Modeling urban pollutant transport at multi-resolutions: Impacts of turbulent mixing

Zining Yang[1], Qiuyan Du[1], Qike Yang[1], Chun Zhao[1,2,3*], Gudongze Li[1], Zihan Xia[1], Mingyue Xu[1], Renmin Yuan[1], Yubin Li[4], Kaihui Xia[1], Jun Gu[1], and Jiawang Feng[1]

[1]Deep Space Exploration Laboratory/School of Earth and Space Sciences/CMA-USTC Laboratory of Fengyun Remote Sensing/State Key Laboratory of Fire Science/Institute of Advanced Interdisciplinary Research on High-Performance Computing Systems and Software, University of Science and Technology of China, Hefei, China

[2]Laoshan Laboratory, Qingdao, China

[3]CAS Center for Excellence in Comparative Planetology, University of Science and Technology of China, Hefei, China.

[4]School of Atmospheric Physics, Nanjing University of Information Science and Technology, Nanjing, China

*Corresponding author: Chun Zhao (chunzhao@ustc.edu.cn)

Key Points:

1. Higher horizontal resolutions improve BC surface concentration predictions by enhancing PBL mixing and vertical wind flux, especially at night.

2. Small-scale eddies resolved at higher horizontal resolutions strengthen vertical fluxes, increasing BC atmospheric lifetime and column concentrations.

3. **Detailed land use and terrain in high ~~-res~~ horizontal resolution models enhance PBL mixing, refining pollutant transport and urban air quality simulations.**

Abstract

Air pollution in cities ~~seriously~~ impacts public health and ~~regional~~ climate. Turbulent mixing ~~plays a~~is crucial ~~role~~ in pollutant formation and dissipation, yet current atmospheric models struggle to accurately represent it. T~~he intensity of t~~urbulent mixing intensity varies with model resolution, which has rarely been analyzed. To investigate turbulent mixing variations at multi-resolutions and their implications for urban pollutant transport, we conducted ~~numerical~~ experiments using WRF-Chem at 25~~ km~~, 5~~ km~~, and 1 km resolutions. The simulated meteorological fields and black carbon (BC) concentrations are compared with observations. Differences in turbulent mixing across multi-resolutions are more ~~more~~ pronounced at night, resulting in noticeable variations in BC concentrations. BC surface concentrations decrease as resolution increases from 25 km to 5 km and further to 1 km, but are similar at 5 km and 1 km resolutions. Enhanced planetary boundary layer (PBL) mixing coefficients and vertical wind flux at higher resolutions reduce BC surface concentration overestimation~~the overestimation of nighttime BC surface concentration~~s. The 1 km resolution parameterized lower ~~PBL~~ mixing coefficients than 5 km but resolved more small-scale eddies, leading to similar near-surface turbulent mixing at both resolutions, while the intensity at higher altitudes is greater at 1 km. This caused BC to be transported higher and farther, increasing its atmospheric lifetime and column concentrations. Variations in mixing coefficients are partly attributed to differences in land use and terrain, with higher resolutions providing more detailed information~~data~~ that enhance~~d~~s PBL mixing coefficients~~.~~, while grid size remains crucial in regions with more gradual terrain and land use changes. This study interprets ~~the impacts of~~how turbulent mixing ~~on~~ affects simulated urban pollutant diffusion at multi-resolutions.

1. Introduction

Since the middle of the 19th century, rapid economic growth and urbanization have caused severe regional haze and photochemical smog pollution (Li et al., 2015; Li et al., 2019; Ma et al., 2019). A variety of air pollution episodes mainly occur in cities (Chan and Yao, 2008). Exposure to atmospheric particulate matter is one of the major threats to public health (Yin et al., 2017; Liu et al., 2019). Accurate pollutant estimation is crucial for the realization of pollution prevention goals. Pollution processes are affected by many different factors, such as pollution source emissions (Li et al., 2017a), physical and chemical characteristics of aerosols (Riccobono et al., 2014; Zhao et al., 2018), topographic effects (Zhang et al., 2018), and meteorological conditions (Ye et al., 2016). Significantly, pollutant concentrations are mainly gathered within the planetary boundary layer (PBL), and PBL mixing processes are associated with intricate turbulent eddies (Stull, 1988), which significantly affect the horizontal transport and vertical diffusion of pollutants (Wang et al., 2018; Du et al., 2020; Ren et al., 2020; Ren et al., 2021), as well as the formation of new aerosol particles (Wu et al., 2021).

The mechanism of turbulent transport has been widely investigated. The vertical diffusion of pollutants in urban areas is affected by the structure of the urban boundary layer (UBL), and different structures may lead to uneven spatial distribution of pollutants (Han et al., 2009; Zhao et al., 2013c). First, meteorological conditions play dominant roles in turbulent mixing of air pollutants within the atmospheric boundary layer (ABL) (Xu et al., 2015; Miao et al., 2019). Unstable meteorological conditions enhance turbulence, promoting pollutant dispersion, while stable conditions suppress it, leading to pollutants accumulation. Previous studies have indicated that constant stagnant winds and increased water vapor density inhibit the vertical diffusion of pollutants, resulting in explosive growth of pollutants (Zhang et al., 2015a; Zhang et al., 2015b; Wei et al., 2018; Zhong et al., 2018). Under these stable conditions, the inherent characteristics of the stable boundary layer (SBL), particularly turbulence intermittency

(Costa et al., 2011), affect the heavy urban haze events by altering surface-atmosphere exchanges (Wei et al., 2018; Ren et al., 2019a; Ren et al., 2019b; Wei et al., 2020; Ren et al., 2021; Zhang et al., 2022). Second, diurnal variations in turbulent mixing between day and night significantly influence changes in pollutant concentrations (Li et al., 2018; Liu et al., 2020). In the daytime convective boundary layer (CBL), pollutants can be mixed uniformly in a thick layer due to the intense turbulent mixing (Sun et al., 2018). While in the nighttime SBL, reduced mixing and dispersion result in the accumulation of pollutants near the surface (Holmes et al., 2015). Severe urban haze pollution formation is typically accompanied with the development of nocturnal SBL (Pierce et al., 2019; Li et al., 2020; Zhang et al., 2020; Li et al., 2022). Moreover, pollutants in the residual layer can be mixed downward to the surface with the development of the ABL the next morning (Chen et al., 2009; Sun et al., 2013; Quan et al., 2020). Overall, the impact of turbulent mixing on urban pollution is important and complex.

Numerical simulation is an important method for studying turbulent mixing. However, there are still challenges associated with accurately representing turbulent mixing in numerical models. Previous researches have indicated that turbulent mixing in current atmospheric chemical models is insufficient to capture stable atmospheric conditions, potentially leading to rapid increases in severe haze in urban areas (Ren et al., 2019b; Wang et al., 2018; Peng et al., 2018; Du et al., 2020). Von Kuhlmann et al. (2003) identified insufficient upward transport of ozone and its precursors due to weak convection. Some studies revealed that WRF-Chem simulations underestimate turbulent exchange within stable nocturnal boundary layers, allowing unrealistic accumulation of pollutants near the surface (McKeen et al., 2007; Tuccella et al., 2012; Berger et al., 2016). Additionally, PBL parameterization schemes in current models may not accurately represent intricate turbulent mixing, particularly in complex terrains, urban areas, or extreme weather conditions. Researches have revealed that different PBL parameterization schemes employed in WRF-Chem tend to underestimate turbulent mixing when compared to observations (Hong et al., 2006; Banks and Baldasano, 2016; Kim, 2006). Turbulent mixing coefficients diagnosed in atmospheric models characterize the intensity of turbulent mixing (Cuchiara et al., 2014). However,

these models frequently underestimate mixing coefficients during the nighttime. Researchers have employed various approaches to address this limitation. Du et al. (2020) demonstrated that increasing the lower limit of PBL mixing coefficients during nighttime significantly reduced the modeling biases in simulated pollutant concentrations. Jia and Zhang (2021) utilized the new modified turbulent diffusion coefficient to represent the mixing process of pollutants separately and improved the simulation results of pollutant concentrations. Jia et al. (2021) employed the revised turbulent mixing coefficient of particles using high-resolution vertical flux data of particles according to the mixing length theory, and improved the overestimation of pollutant concentrations. In conclusion, current atmospheric models commonly face several challenges in accurately simulating turbulent mixing.

The representation of turbulent mixing in models is influenced by various factors, including grid resolution, topography, boundary layer parameterization, atmospheric dynamics, and land-surface processes. Among these factors, model resolution can significantly affect turbulent mixing processes in atmospheric simulations, with simulated turbulent mixing varying substantially across different resolutions. Qian et al. (2010) evaluated model performance at 3 km, 15 km, and 75 km resolutions, finding that only simulations at 3 km resolution accurately captured multiple concentration peaks in observational data, indicating that turbulent mixing may play a critical role in simulating pollutant concentrations. Fountoukis et al. (2013) conducted model simulations at three resolutions and demonstrated that higher resolution reduced the bias for BC concentration by more than 30% in the Northeastern United States during winter, attributing this improvement to better resolved pollutant dispersion. Tao et al. (2020) found that changes in model resolution led to increased pollutant concentrations in urban areas but decreased concentrations in west mountain regions, likely due to differences in vertical and horizontal dispersion. In conclusion, previous researches have primarily focused on comparing pollutant concentrations across different model resolutions, demonstrating that resolution significantly affects pollutant distribution and dispersion. These studies suggest that turbulent mixing may play a crucial role. However, few have systematically explored the specific mechanisms by which

turbulent mixing influences pollutant concentrations simulated at multi-resolutions, despite their importance in determining urban atmospheric pollutions.

Motivated by aforementioned problems, this study aims to investigate differences in pollutant concentrations across multi-resolutions and explore how the turbulent mixing plays as a crucial role affecting pollutant concentrations at various resolutions. Furthermore, we seek to determine whether higher-resolution simulations can address the issue of inaccurate turbulent mixing in current models. The Weather Research and Forecasting model coupled with Chemistry (WRF-Chem) is applied to simulate pollutant and meteorological fields during the spring of 2019 in Hefei, a typical mega-city and sub-center of the Yangtze River Delta (YRD) urban agglomeration in China, with a population of nearly 10 million and an area of 11,445 km^2. Our study interprets the various characteristics of black carbon (BC) distributions simulated at multi-resolutions and focuses on the mechanisms involved. BC is selected as the primary pollutant for this study due to its near-inert nature in the atmosphere and can be treated as a representative tracer for turbulent mixing. The paper is organized as follows: Section 2 introduces the WRF-Chem model configuration, the design of multi-resolutions experiments, emissions from different sources, and observational data. Section 3 evaluates model simulations across multi-resolutions against observations, presents the spatial distributions of surface and column concentrations simulated at three resolutions, and investigates the important turbulent mixing processes that generate spatial variability in pollutant concentrations. Section 4 present the conclusion and discussion of the analysis.

2. Methodology

2.1 Models and Experiments

2.1.1 WRF-Chem

The non-hydrostatic Weather Research and Forecasting (WRF) model includes various options for dynamic cores and physical parameterizations that can be used to simulate atmospheric processes over a wide range of spatial and temporal scales

(Skamarock et al., 2008). WRF-Chem, the chemistry version of the WRF model (Grell et al., 2005), simulates trace gases and particulates interactively with the meteorological fields. WRF-Chem contains some treatments for photochemistry and aerosols developed by the user community. In this study, the version of WRF-Chem updated by the University of Science and Technology of China (USTC version of WRF-Chem) is used. Compared with the publicly released version, this USTC version of WRF-Chem includes some additional functions such as the diagnosis of radiative forcing of aerosol species, land surface coupled biogenic VOC (volatile organic compound) emission, aerosol-snow interaction, improved PBL mixing of aerosols and a detailed diagnosis of the contributions of each crucial process to pollutant concentrations (Zhao et al., 2013a; Zhao et al., 2013b; Zhao et al., 2014; Zhao et al., 2016; Hu et al., 2019; Du et al., 2020; Zhang et al., 2021).

The configuration of WRF-Chem in this study is given in Table 1. The Statewide Air Pollution Research Center (SAPRC99) photochemical mechanism (Carter, 2000) is chosen to simulate the gas-phase chemistry, and the Model for Simulating Aerosol Interactions and Chemistry (MOSAIC) is also selected (Zaveri and Peters, 1999; Zaveri et al., 2008). The MOSAIC aerosol scheme includes important physical and chemical processes such as nucleation, condensation, coagulation, aqueous-phase chemistry, and water uptake by aerosols. Sulfate, nitrate, ammonium, sea salt, mineral dust, organic matter (OM), BC, and other (unspecified) inorganics (OIN) constitute the prognostic species in MOSAIC. The aerosol direct effect is coupled to the Rapid Radiative Transfer Model (RRTMG) (Mlawer et al., 1997; Iacono et al., 2000) for both SW (shortwave) and LW (longwave) radiation as implemented by Zhao et al. (2011). We also turned on the aerosol indirect effect, which represents the interactions between aerosols and clouds, including the first and second indirect effects, activation/resuspension, wet scavenging, and aqueous chemistry (Gustafson et al., 2007; Chapman et al., 2009). The photolysis rate is computed by the Fast-J radiation parameterization (Wild et al., 2000). Our simulation includes the secondary organic aerosol (SOA) mechanism, a crucial aerosol process that can substantially reduce discrepancies between simulated results and observations.

Another type of option is meteorological physics, including the Yonsei University (YSU) nonlocal PBL parameterization scheme (Hong et al., 2006), the Noah land-surface model (Chen and Dudhia, 2001) for the surface layer process, the Morrison two-moment scheme (Morrison et al., 2009) for cloud microphysics, and the Rapid Radiative Transfer Model (RRTMG) for longwave and shortwave radiation. The 25 km resolution simulation turns on the option of cumulus parameterization, which uses the Kain-Fritsch cumulus and shallow convection scheme (Kain, 2004) to simulate sub-grid scale clouds and precipitation. However, this option is turned off in the other two higher resolution simulations because the fine-resolution is sufficient to resolve the cloud forming processes.

2.1.2 Numerical experiments

The study period spans from March 5th to March 20th, 2019. Following previous research (Gustafson et al., 2011), the first five days are considered as the model spin-up time, while the remaining integration period is used for analysis. Consequently, only the results from March 10th to March 20th, 2019, are used in the analysis of this study. Three different resolutions and computational domains are employed in our study. The outer domain, covering East, North, and South China, has 140 x 105 grid cells (107.1°-127.9°E, 17.1°-44.9°N) with a horizontal resolution of 25 km. The middle domain, encompassing the entire YRD region in East China, has 250 x 250 grid cells (111.82°-121.78°E, 27.02°-36.98°N) with a resolution of 5 km. The inner domain, covering most of the Hefei region, consists of 150 x 150 grid cells (116.604°-117.796°E, 31.204°-32.396°N) at a horizontal resolution of 1 km. The center of inner domain is the city of Hefei, a typical mega-city of East China. Hefei, the capital city of Anhui province, is located in the mid-latitude zone with a humid subtropical monsoon climate and serves as a representative case for this study. The regions are shown in Figure S1. To facilitate the comparison of discrepancies among the three simulations at different resolutions, we have selected the innermost region as the main scope of study for this research, as shown in Figure 1a.

In this study, we derive terrain information from a high-resolution (~ 1 km) US

Geological Survey (USGS) topographic data and interpolate it onto the WRF grid. Therefore, the three domains with different resolutions exhibit varying degrees of terrain detail. The 1 km grid resolves the most intricate topographic features, followed by the 5 km grid, while the 25 km grid captures the least spatial detail. These multi-resolutions topographic representations potentially influence pollutant turbulent mixing processes, which will be analyzed in this study. The land cover dataset is derived from a 1 km horizontal resolution dataset for China (Zhang et al., 2021). The land use categories follow the United States Geological Survey's (USGS) 24-category classification, and the dataset is based on China's land cover conditions as of 2015. ~~It~~ This provides a more accurate representation of current land cover, particularly for eastern China, which has experienced intensive urban expansion since the 2000s. Figure 1b shows the land cover data at different resolutions, with detailed descriptions of the legend and land cover classes provided in Table S1. This set of simulations is referred to as the baseline experiment. With the exception of part of Section 3.2.3, all other analyses in this study are based on the results of these baseline experiments. Moreover, to explore the differences in turbulent mixing simulated at multi-resolutions under consistent land use conditions, we conducted an additional set of sensitivity experiments referred to as the sensitivity experiment. The sensitivity experiment was identical to the baseline experiment, except it used the default USGS land use category data in WRF. Notably, this default USGS data in WRF's geographical static database represents Chinese land use patterns before the 2000s, as shown in Figure S2. This default dataset reflects land use distribution prior to China's significant urbanization. Consequently, the land use data types have minor variations and remained generally consistent across all three resolutions in the sensitivity experiment.

On the other hand, the vertical configuration within the PBL is also crucial for accurately modeling pollutant dispersion. To better resolve the PBL structure and mixing processes, we implemented a finer vertical resolution within the PBL. Identical vertical layer distributions are maintained across all three horizontal resolutions (25 km, 5 km, and 1 km), ensuring direct comparability of turbulent mixing across different horizontal resolutions. A total of 50 terrain-following vertical eta-layers extending from

the surface to approximately 15 km were used in all three resolution simulations, with 30 layers distributed below 2 km above the ground to describe the atmospheric boundary structure in detail. The vertical layer was strategically designed with 7 layers below 200 meters (each approximately 20 meters in height), 3 layers between 200 and 300 meters (each about 30 meters in height), and 8 layers between 300 and 1000 meters (each approximately 80 meters in height). This configuration comprehensively captures mixed layer development and key turbulent processes (e.g., entrainment and surface flux exchange) through layer densification, which is sufficient to capture PBL turbulent mixing. Jiang et al. (2024) and Jiang and Hu (2023) have demonstrated that the number of model vertical layers primarily influences vertical distribution, with more vertical grid layers producing a more stable vertical structure under stable boundary conditions that better resolves boundary layer turbulence.

In order to allow for a straightforward comparison of multi-resolutions simulations and facilitate the identification of differences between the high- and low-resolution simulations, the corner locations of the 1 km and 5 km resolution domains are aligned with the corner locations of the 25 km grid cell. Each grid cell in the 25 km simulation consists of a 5 x 5 set of cells from the 5 km simulation, and each grid cell in the 5 km simulation comprises 5 x 5 cells from the 1 km simulation, as shown in Figure ~~S2~~S3. Thus, exactly 25 grids at 5 km resolution and 625 grids at 1 km resolution are embedded within each 25 km grid cell.

To ensure similar boundary forcing across the three simulations, initial and boundary conditions are handled differently for the 25 km, 5 km, and 1 km resolution domains. For the 25 km resolution, meteorological initial and lateral boundary conditions are obtained from the National Center for Environmental Prediction (NCEP) final reanalysis (FNL) data with 1° x 1° resolution and 6 h temporal resolution. Initial and boundary conditions for the trace gases and aerosol species are provided by the quasi-global WRF-Chem simulation with 360 x 145 grid cells (67.5°S-77.5°N, 180°W-180°E) at 1° x 1° resolution. The initial and boundary conditions for the simulation at 5 km resolution are derived from the simulation at 25 km resolution. Similarly, the initial and boundary conditions for the simulation at 1 km resolution are derived from

the simulation at 5 km resolution. In this way, since the forcing for the study area is consistent across multi-resolutions, differences in simulation results among multi-resolutions can be attributed to disparities in model resolutions.

2.1.3 Emissions

Anthropogenic emissions for the outer quasi-global simulation are derived from the Hemispheric Transport of Air Pollution version-2 (HTAPv2) at 0.1° x 0.1° horizontal resolution and a monthly temporal resolution for 2010 (Janssens-Maenhout et al., 2015). The Multi-resolution Emission Inventory for China (MEIC) at 0.25° x 0.25° horizontal resolution for 2019 (Li et al., 2017a; Li et al., 2017b) is used to replace emissions over China within the simulation domain. Emission differences significantly contribute to pollutant concentration variability across multi-resolutions. Qian et al. (2010) showed that sub-grid variability of emissions can contribute up to 50% of the variability near Mexico City. To eliminate the impact of inconsistent emissions on pollutant concentrations simulated at multi-resolutions, we ensured emission consistency across ~~the~~ all three domains by interpolating emissions for all species from the 25 km resolution domain to both the 5 km and 1 km resolution domains~~the 25 km resolution emissions of primary species (NH3, CO, NO2, SO2, BC, OC, PM2.5, PM10, SO4, NO3) to the 5 km and 1 km resolution domains~~. This study primarily focuses on BC, the spatial distribution of BC emissions is shown in Figure ~~2~~2. Figure ~~S3~~ S4 illustrates BC emissions at three different resolutions, demonstrating similar spatial patterns across multi-resolutions. Biomass burning emissions are obtained from the Fire Inventory from NCAR (FINN) at 1 km horizontal resolution and an hour temporal resolution (Wiedinmyer et al., 2011). The diurnal variation of biomass burning emissions follows the suggestions by WRAP (2005), with injection heights based on Dentener et al. (2006) from the Aerosol Comparison between Observations and Models (AeroCom) project. Biogenic emissions were calculated using the Model of Emissions of Gases and Aerosols from Nature (MEGAN) v3.0 model (Zhang et al., 2021).

2.2 Observational data

2.2.1 Meteorological data

The meteorological data were obtained from the observation tower at the University of Science and Technology of China (USTC) in Hefei, Anhui, China (117.27°E, 31.84°N), indicated by a solid black triangle in Figure 1a. The tower measures temperature, relative humidity, wind speed, and wind direction at 2 m, 4.5 m, 8 m, 12.5 m and 18 m heights. This site represents a typical urban surface within the study area. The tower was installed on the roof of a teaching building, with its top 17 m above the canopy plane. It is equipped with three RM Young 03002 anemometers and three HPM155A temperature and humidity sensors to measure the aforementioned meteorological parameters (Yuan et al., 2016; Liu et al., 2017). This study focuses on analyzing temperature, relative humidity, and wind speed.

Additionally, we employed meteorological data from automatic weather stations (AWSs), which were established based on the operational standards issued by the China Meteorological Administration (CMA, 2018). The hourly data underwent quality control (QC) by local meteorological bureaus of Anhui, following World Meteorological Organization guidelines (Estevez et al., 2011). The QC included checks of consistency, such as internal, temporal-spatial, and climatic range validations. These QC data were used to determine daily mean, minimum, and maximum meteorological variables. The AWSs recorded various parameters, including air temperature (T, °C), wind speed (U, m/s), air pressure (P, Pa), and wind direction. In this study, we focus on the 3-hourly 2 m temperature and 10 m wind speed obtained from four AWS stations located in the study region. The four AWS sites are marked by purple solid dots in Figure S5.

2.2.2 Pollutants data~~BC surface concentration~~

~~In this study, w~~We derived the hourly BC observations from the air quality monitoring site on the campus of USTC during spring (March 10 to March 20, 2019). ~~Hefei, a major industrial and transportation hub, serves as the study area.~~ In this study, we focus on analyzing BC observational data to compare with model output. BC was observed using a Multi-angle Absorption Photometer (MAAP, Model-5012)

manufactured by Thermo Scientific. This instrument is located approximately 260 m north of the USTC meteorological tower. It takes advantage of the strong visible light absorption properties of BC aerosols. There is a linear relationship between the attenuation of the beam after passing through the aerosol sample and the load of BC aerosols on the fiber membrane. The BC concentration is derived by inverting this relationship. A light scattering measurement is incorporated into the chamber to correct for multiple scattering effects caused by particle accumulation on the filter tape. The MAAP-5012 Black Carbon Meter collects atmospheric aerosols using glass fiber filter membranes and observes them at a wavelength of 670 nm.

Although this study primarily focuses on the simulation of BC, we conducted a comprehensive validation of other air pollutants to ensure the reliability of the simulation results. However, after being initially obtained via a parameterized PBL scheme, the mixing coefficients for gases are then clipped to empirically chosen thresholds of 1 m^2/s over rural regions and 2 m^2/s over urban regions, with the distinction between rural and urban regions made based on the local CO emission strength. Thus, the boundary layer mixing coefficient for gases in the WRF-Chem model is implicitly influenced by emission resolution rather than directly controlled by model resolution. Consequently, the existing adjustment process for gas mixing coefficients, which relies on CO emission strength, is unsuitable for studying the impact of model resolution on the turbulent mixing of gaseous pollutants. In contrast, the mixing coefficient of particulate matter is directly calculated through boundary layer parameterization without subsequent modifications. Thus, in this study, we limited our additional validation to $PM_{2.5}$ (fine particulate matter with aerodynamic diameters less than 2.5 μm), whose mixing processes are governed by the same resolution-dependent mechanisms as BC. Ground observations of hourly $PM_{2.5}$ surface concentrations during March 2019 were obtained from the website of the Ministry of Environmental Protection of China (MEP of China). As our study concentrates on the Hefei region, we selected 10 monitoring stations within this area for detailed analysis. These stations are marked as black triangles in Figure S5.

While hourly observations for both meteorology and pollutants are available, model

outputs are provided at 3-hour intervals to balance computational efficiency and storage requirements. Hourly output data would provide higher time resolution but significantly increase storage demands. Given that we ran simulations at multi-resolutions (25 km, 5 km, and 1 km), hourly outputs would have generated prohibitively large data volumes. On the other hand, this 3-hour output interval remains sufficient for our primary research objective of analyzing daily pollutant variations (particularly BC) rather than precise hourly comparisons. We believe this approach effectively captures daily variability patterns without losing essential detail. For direct comparisons, hourly observations were sampled to match our 3-hour model output intervals.

3. Results

3.1 Simulated meteorological fields at various horizontal resolutions

Meteorological fields may play a crucial role in the turbulent mixing and pollutant transport. In this study, we evaluate time series of simulated temperature, wind speed, and relative humidity across three resolutions against observational data to assess resolution impacts on these key meteorological variables~~Therefore, the time series of simulated temperature, wind speed, and relative humidity are evaluated in this study. We evaluate simulated results at three resolutions against observations to assess the impact of resolution on these key meteorological variables~~. Figure 3a compares the time series of observed and simulated 8-m wind speeds at the USTC site (117.27°E, 31.84°N). Simulation results among multi-resolutions are similar, attributing to relatively flat and uncomplicated topography. The temporal trends of the simulations closely align with observational data, exhibiting distinct diurnal variations characterized by higher values during the daytime and lower values at night. Additionally, the model struggles to capture some moments accurately, overestimating wind speed when it suddenly increases. For instance, on March 20 at noon, while the observed peak wind speed is approximately 6 m/s, simulations at 25 km and 5 km resolutions produced maximum wind speeds of approximately 9 m/s, significantly exceeding the observed value, with only the 1 km resolution simulation yielding results

close to the observation. Figure 3b compares the 2-m temperature simulated at three different resolutions with the observation. The multi-resolutions simulation results exhibit remarkable consistency and closely align with observations. Temperature displays a pronounced diurnal variation, fluctuating between 5 and 30 ℃ with relative stability. However, the model occasionally underestimates or overestimates values at certain time points. As shown in Figure 3c, the multi-resolutions simulated results demonstrate consistency and accurately capture the diurnal variation trend of observed relative humidity (RH). Model results are highly consistent with observations, both reaching a maximum of 100%.

Additionally, Figure S6 displays the time series of observed and simulated meteorological variables averaged across four AWS stations in the study region. Figure S6a presents a comparison of 10-m wind speed simulated at three different resolutions, revealing generally consistent results with observations. The overall pattern is similar to that observed at the single USTC station, characterized by a clear diurnal variation with higher wind speeds during daytime and lower speeds at night. However, simulations at all three resolutions occasionally deviate from observations. For example, on March 11, the 5 km and 1 km resolution models overestimate wind speed at approximately 7 m/s compared to the observed 4 m/s. Conversely, on March 14 during the daytime, all three resolutions underestimate wind speed, simulating around 2 m/s against an observed value of 4 m/s. Figure S6b compares the simulated 2-m temperatures across three resolutions with observational data. The simulated temperatures are remarkably similar across all resolutions and show strong correlation with observations throughout most of the study period. Only a few outliers were noted, which minimally impact the overall pattern. For example, all resolution models overestimate temperature at noon on March 20, simulating approximately 28°C while the observed temperature is only about 20°C.

In summary, the simulated meteorological variables across multi-resolutions demonstrate strong similarity and closely match the observations, with only occasional minor discrepancies. However, our subsequent analysis reveals that the variations in pollutant concentrations across multi-resolutions cannot be attributed to the minor

discrepancies observed in the time series of meteorological variables.

3.2 Simulated BC~~BC~~ surface concentrations and impacts of turbulent mixing at various horizontal resolutions

3.2.1 Surface concentrations simulated at three different horizontal resolutions

The spatial distribution of BC surface concentrations across multi-resolutions in the study area is illustrated in Figure ~~4~~4. As the resolution improves from 25 km to 5 km and further to 1 km, BC surface concentrations reveal more detailed spatial features. Figure ~~4a~~ 4a presents the simulation results across multi-resolutions, averaged over the whole day. Significant variations exist from coarse resolutions to fine resolutions, with surface concentrations decreasing as resolution increases from 25 km to 5 km and further to 1 km. BC surface concentrations range from 0 to 9 ug/m^3. At 25 km resolution, there is a notable discrepancy between the spatial distributions of BC concentrations and emissions (Fig. ~~2~~2). The highest simulated concentration at 25 km resolution is located west of the USTC site, while maximum emissions are centered at the USTC site. Our analysis indicates that the difference in turbulent mixing between these two regions leads to spatial inconsistency between BC surface concentrations and emissions. The details of this phenomenon will be discussed in section 3.2.2. Figure ~~4b~~ 4b illustrates the spatial distribution of BC surface concentrations during the daytime. The differences in surface concentrations among multi-resolutions are minimal, with values falling within the range of 0 to 5 ug/m^3. In the central urban areas, the BC surface concentration simulated at 25 km resolution is marginally lower than those simulated at finer resolutions. Moreover, during the daytime, simulated BC concentrations over Chaohu lake areas are notably higher than in other regions, potentially due to the impact of dry deposition velocity. Figure ~~S4~~ S7 shows the spatial distribution of dry deposition velocity, revealing lower values over lakes compared to other areas. This lower dry deposition velocity leads to higher pollutant concentrations over lakes compared to land areas after pollutants transport to the lake surface during the daytime. At night, dry deposition velocity is similar to that of surrounding non-urban land areas. Consequently, nighttime BC concentrations over lakes are approximately equal to those in surrounding

areas. Figure ~~4c~~ 4c demonstrates the spatial distribution of BC surface concentrations during nighttime. Compared to daytime, BC surface concentrations are notably higher in all major urban regions at night, with high-resolution simulations capturing more spatial variations. In conclusion, BC surface concentrations decrease as resolution increases from 25 km to 5 km and further 1 km. However, the spatial distribution of BC surface concentrations at 5 km and 1 km resolutions are similar throughout the whole day.

To facilitate a more accurate and direct comparison of results across multi-resolutions, we refine coarse grids to match fine grids. The detailed refinement process is described in Text S1. Figure ~~S5a~~ S8a exhibits the spatial differences in BC surface concentrations between 25 km and 5 km resolutions, as well as between 25 km and 1 km resolutions, averaged over the whole day. It reveals that coarse-resolution (25 km resolution) simulations generally yield higher BC surface concentrations than fine-resolutions (5 km and 1 km resolution) simulations across most areas. The largest disparities mainly occur in central urban areas with complex underlying surfaces and complicated flow patterns. Figure ~~S5b~~ S8b demonstrate the spatial differences in BC surface concentrations between 25 km and 5 km resolutions, as well as between 25 km and 1 km resolutions during the daytime, revealing smaller disparities mostly ranging between -1 and 1 ug/m^3. In contrast, Figure ~~S5c~~ S8c depicts pronounced differences in BC concentrations between 25 km and 5 km resolutions, as well as between 25 km and 1 km resolutions during the nighttime, with most areas exhibiting disparities exceeding 2 ug/m^3. The largest differences are mainly concentrated in urban areas. These findings indicate that diversities in BC surface concentrations among multi-resolutions are primarily attributable to nocturnal concentrations in urban areas. However, differences between 5 km and 1 km resolutions are small compared to those between 25 km and finer resolutions (5 km and 1 km). BC surface concentrations are approximately equal in the 5 km and 1 km simulations, as shown in Figure ~~S6~~S9.

Furthermore, BC observations from the USTC monitoring station were utilized to validate the simulated BC surface concentrations. Figure ~~5~~ 5 illustrates the diurnal variation of BC surface concentrations ~~averaged over the Hefei region~~averaged over

the USTC site. Both observations and simulations exhibit a pronounced diurnal variation, with lower concentrations during the daytime and higher concentrations at night. During the daytime, BC surface concentrations simulated at three resolutions are comparable to the observational data. However, nighttime simulations significantly overestimate BC surface concentrations. As resolution increases from 25 km to 5 km and 1 km, the simulated surface concentrations decrease, aligning more closely with observations. The 25 km resolution simulations yield the highest concentrations, with a maximum value of approximately 12 ug/m^3, nearly double the observed values. In contrast, BC surface concentrations simulated at 5 km and 1 km resolutions are similar and more closely align with nocturnal observations, peaking at around 9 ug/m^3. In conclusion, the diurnal variation of the observation is better captured by high-resolution (5 km and 1 km) simulations. The performance of BC surface concentrations across multi-resolutions demonstrates that coarse grid spacing inadequately captures local pollutant distributions.

To verify the accuracy and comprehensiveness of the simulation results, we further analyzed the diurnal variation of $PM_{2.5}$ surface concentrations. Figure S10 illustrates the diurnal variation of simulated $PM_{2.5}$ surface concentrations across multi-resolutions compared with observations. The diurnal pattern of $PM_{2.5}$ closely resembles that of BC, characterized by higher concentrations at night and lower concentrations during daytime. Across all resolutions, the model slightly underestimates daytime $PM_{2.5}$ surface observations while overestimating nighttime values. Notably, increased horizontal resolution substantially improves nocturnal simulations. The 25 km resolution simulation generates an anomalous midnight peak (105 μg/m³), resulting in a +61% bias, whereas the 5 km and 1 km resolutions substantially mitigate these deviations to approximately 30%. To further examine the contribution of each $PM_{2.5}$ component to the diurnal variation across multi-resolutions, Figure S11 shows the diurnal variations of four $PM_{2.5}$ constituents (sulfate (SO_4^{2-}), nitrate (NO_3^-), OIN, and organic carbon (OC)) averaged over 10 MEP sites in Hefei. Significant differences emerge in the diurnal variations of these components across multi-resolution simulations. Specifically, the surface concentrations of NO_3^-, OIN, and OC exhibit a

consistent diurnal pattern, with lower concentrations during daytime and higher concentrations at night. As resolution increases from 25 km to 5 km and 1 km, the simulated components surface concentrations decrease, aligning more closely with observations.

The total concentration of $PM_{2.5}$ and its components demonstrates significant sensitivity to horizontal resolutions. Coarse resolution simulations underestimate turbulent mixing capacity, resulting in overestimated concentrations. Higher resolution simulations more accurately capture vertical mixing within the PBL. For secondary particles such as sulfates and nitrates, formation rates depend heavily on local precursor substance concentrations (SO_2, NO_x). Higher resolution simulations may enable more realistic representation of precursor substance diffusion, leading to reduced local concentration gradients and consequently slower secondary aerosol formation rates. Additionally, variations in $PM_{2.5}$ surface concentrations across multi-resolutions may also stem from complex secondary particle generation mechanisms. For instance, liquid-phase oxidation of sulfates in clouds is sensitive to local cloud water distribution, with higher resolutions better capturing small-scale cloud structures that potentially alter sulfate formation efficiency. The formation of ammonium nitrate (NH_4NO_3) is particularly sensitive to temperature and humidity variations. At higher resolutions, temperature and humidity gradients induced by urban heat island effects or topographical variations can be more realistically simulated, influencing the distribution of gaseous nitric acid (HNO_3) and particulate nitrate (NO_3^-). Dry deposition processes may also contribute to resolution-dependent variations, as local differences in surface roughness (including buildings and vegetation) become more apparent at higher resolutions, directly affecting particulate deposition velocity rates. Overall, the simulation results for major air pollutants fall within a reasonable error range compared to observational data, confirming the reliability of the model for this study.

We now aim to further investigate the underlying factors contributing to the discrepancies in atmospheric pollutant simulations, with a particular focus on BC, across different spatial resolutions. Previous studies have indicated that~~referred that~~ the diurnal variation of ~~BC surface~~atmospheric particulate matter concentrations ~~is~~ is

primarily ~~mainly~~ controlled by daily variations of PBL mixing and ~~BC~~ pollutants emissions (Du et al., 2020). The diurnal variation of BC emissions peak during the daytime and are lower at night. ~~–~~During nighttime,~~At night,~~ pollutants are trapped within the shallow boundary layer due to the reduced turbulent mixing, resulting in elevated~~high~~ ~~BC~~ surface concentrations~~.~~ of atmospheric particulate matter. As the boundary layer develops in the morning, pollutants rapidly diffuse and are transported to upper atmospheric layers, leading to relatively low surface concentrations. Therefore, the turbulent mixing process plays a crucial role in determining pollutant concentrations. ~~To elucidate the mechanisms underlying the disparities in simulated BC surface concentrations across multi-resolutions in urban areas, we conducted several in-depth analyses to investigate the impact of turbulent mixing on pollutant concentrations.~~

3.2.2 Impacts of turbulent mixing on BC surface concentrations at three different horizontal resolutions

To investigate the vertical mixing depth influencing pollutant diffusion, we first analyze the PBL height, as illustrated in Figure 6. Figure 6a shows the spatial distribution of the PBL height simulated at three different resolutions, averaged over the whole day. Higher-resolution simulations yield lower PBL heights and capture more intricate details compared to lower-resolution simulations. This trend is consistent during both daytime and nighttime. Figure 6b demonstrates that the PBL height exceeds 0.9 km across most regions during the daytime. Notably, due to strong topographic influences, the PBL height in the vicinity of Chaohu Lake is remarkably low, typically less than 0.1 km. Conversely, in the southwestern region, characterized by higher elevations and more complex terrain, the PBL height surpasses 1.1 km. Figure 6c depicts the nighttime PBL heights at three different resolutions. These heights predominantly fall below 0.3 km, significantly lower than those during the daytime. The PBL height gradually decreases as the resolution increases, which should typically lead to higher BC surface concentrations. However, BC surface concentrations actually decrease as resolution increases from 25 km to 5 km and 1km (Figure 4). Consequently, the PBL height alone cannot explain the differences in pollutant simulations among

multi-resolutions in this study.

Previous studies have established that PBL mixing coefficients are critical determinants in air quality modeling (Du et al., 2020)~~(Du et al., 2020)~~. In WRF-Chem, turbulent mixing within the boundary layer is partially governed by PBL mixing coefficients generated by the PBL parameterization scheme. It is worth noting that the mixing coefficients for atmospheric particulate matter and gases are two distinct variables in the current version of WRF-Chem. The boundary layer mixing coefficient for gases is initially obtained via a parameterized PBL scheme but undergoes additional modification through an empirical parameterization that enhances gas mixing based on CO emission strength~~In WRF-Chem, turbulent mixing within the boundary layer is partially governed by PBL mixing coefficients simulated by the PBL parameterization scheme.~~ (Kuhn et al., 2024). This enhancement applies to gas pollutants when using the MOSAIC aerosol scheme, as implemented in this study. Specifically, gas mixing coefficients are clipped to empirically chosen thresholds of 1 m^2/s over rural regions and 2 m^2/s over urban regions, with the distinction between rural and urban regions made based on the local CO emission strength. In contrast, the mixing coefficient of particulate matter is directly calculated through boundary layer parameterization without subsequent modifications. Our study focuses exclusively on the turbulent mixing of atmospheric particulate matter, analyzing the aerosol mixing coefficient with the default lower limit of 0.1 m^2/s as specified in the publicly released version of WRF-Chem. Additionally, we have not implemented the mixing coefficient adjustments proposed by Du et al. (2020), which suggest raising the lower limit of PBL mixing coefficient from 0.1 m^2/s to 5 m^2/s within the PBL. Unlike gas mixing coefficients, the particulate matter mixing coefficient is directly calculated through boundary layer parameterization without adjustments based on pollutant emission data, thus not being limited by emission resolution. This approach allows the model to more accurately represent the natural turbulent mixing processes. Consequently, we can investigate the turbulent mixing intensity of particulate matter across different horizontal resolutions and examine the true impact of grid resolution on pollutant mixing.

The spatial distribution of aerosol turbulent mixing coefficients at the lowest model

layer is analyzed, as shown in Figure 7. Figure 7a illustrates the simulation results across multi-resolutions averaged over the whole day. The variations in PBL mixing coefficients across different resolutions are evident, with high-resolution simulations capturing more spatial characteristics. The spatial distribution of the PBL mixing coefficient demonstrates strong correlation with land use type and terrain height, which will be explored subsequently. Turbulent mixing coefficients range from 0 to 8 m^2/s, with peak values predominantly located in urban areas. Notably, the mixing coefficient simulated at 25 km resolution near surface around USTC substantially exceeds that of the western area, resulting in lower BC surface concentrations simulated at 25 km resolution at USTC compared to its western regions (Figure 4). This discrepancy leads to a mismatch between the spatial distribution of pollutant concentrations and emissions, as discussed in section 3.2.1. During the daytime, the PBL mixing coefficients simulated at three resolutions are relatively high, ranging from 0 to 17 m^2/s, as shown in Figure 7b. BC masses simulated across multi-resolutions are fully mixed within the boundary layer, resulting in similar BC surface concentrations across these resolutions. Conversely, turbulent mixing coefficients diminish considerably during the nighttime, with maximum values approximately 3 m^2/s, as shown in Figure 7c. The turbulent mixing coefficient emerges as one of the important factors controlling surface pollutant concentrations under stable nocturnal PBL conditions. Nighttime PBL coefficients are higher at 5 km and 1 km resolutions compared to 25 km resolution across most of the study area, resulting in lower BC surface concentrations at these two higher resolutions during the nighttime. Figure ~~S7~~ S12 further illustrates the disparities in parametrized PBL mixing coefficients between 25 km resolution and the two higher-resolution simulations. However, ~~in the lowest model layer,~~ Figure ~~S8~~ S13 shows that the intension of turbulent mixing parameterized at 5 km resolution is larger than that at 1 km resolution, which fails to explain the similar surface concentrations in these two higher-resolution (5 km and 1 km) simulations. To further investigate this phenomenon, we selected a meridional section passing through the USTC site to analyze the distribution of vertical wind speed flux, which represents the turbulent mixing directly resolved by large-scale dynamic processes.

Figure 8 displays the cross section of meridional wind speed flux along the USTC site simulated at three different resolutions. The upward vertical wind speed flux simulated at 25 km resolution are near the surface. However, the 5 km resolution simulation generates stronger upward motion at a slightly higher altitude, specifically between 850 and 1000 hPa. Notably, the 1 km resolution simulation captures the highest vertical wind speed flux, with relatively intensive upward motion extending beyond 500 hPa. The 1 km resolution can resolve small-scale eddies and capture the most pronounced vertical wind speed fluxes. In comparison, simulations at 5 km resolution are able to capture smaller-scale eddies, while those at 25 km resolution occasionally capture larger-scale eddies. Despite the larger PBL mixing coefficients at 5 km resolution compared to 1 km resolution near the surface, the upward vertical wind speed flux at 1 km resolution reaches higher altitudes, indicating the presence of more small-scale eddies and resulting in enhanced vertical turbulent mixing. Consequently, near the surface, the combined effects of turbulent mixing, which is represented by both the parameterized PBL mixing coefficient and the directly resolved vertical wind speed flux, lead to similar BC surface concentrations at higher resolutions (5 km and 1 km) simulations. Furthermore, Figure ~~S9~~ S14 shows the meridional cross section during daytime and nighttime. During the day, the mixing height vertically upward is relatively high at all three resolutions, allowing pollutants to be fully mixed and transported within the PBL. This results in similar BC surface concentrations across multi-resolutions. Conversely, at night, high-resolution simulations resolve more small-scale eddies, resulting in vertical transport reaching higher altitudes and intensifying turbulent mixing. In conclusion, pollutants in lower-resolutions (25 km) simulations tend to accumulate near the surface, whereas at higher resolutions (5 km and 1 km) simulations, pollutants are transported to higher heights. This phenomenon contributes to imparities in BC surface concentration across multi-resolutions.

3.2.3 Impacts of land use type and terrain height on turbulent mixing coefficients at three different horizontal resolutions

Previous analysis indicate that the PBL mixing coefficient is one of the main factors

contributing to the disparities in BC surface concentrations across multi-resolutions. Therefore, we further explored the factors influencing the spatial distribution of the PBL mixing coefficient. Our analysis reveals that the spatial distribution of the PBL mixing coefficient is closely related to land use types and terrain height. Specifically, the overall distribution of the turbulent mixing coefficient is closely resembled by the land use types (Figure 1b and Figure 7). However, in areas with obvious magnitude changes, such as east of the USTC site, the turbulent mixing coefficient displays distinct gradient changes that are not reflected in land use patterns. Notably, the spatial distribution of the topographic height (Figure 1a) in this region exhibits distinct gradient changes similar to those of the turbulent mixing coefficients. Consequently, the spatial distribution of the turbulent mixing coefficient is influenced by both terrain and land use types. This correlation can be attributed to the inter-relationship among turbulent mixing, friction velocity, terrain, and land use types. Terrain and land use types influence friction velocity by modifying surface roughness, which in turn directly affects turbulent mixing coefficients within the PBL. Higher surface roughness typically lead to greater fiction velocity, subsequently enhancing turbulent intensity and increasing the vertical mixing efficiency of pollutants within the PBL. To further investigate this relationship, the spatial distribution of friction velocity is analyzed, as shown in Figure 9. The analysis reveals that friction velocity increases as resolution increases from 25 km to 5 km and 1 km resolutions, with finer resolutions (5 km and 1 km) capturing more spatial details. Differences in friction velocity are illustrated in Figure ~~S10~~S15. The spatial distribution of friction velocity indeed correlates with terrain and land use patterns, consequently influencing the distribution of the PBL mixing coefficient. As a result, the spatial distribution of the PBL mixing coefficient correlates with land use types and terrain height.

Our study indicates that variations in land use type distribution simulated at different horizontal resolutions are a significant factor causing changes in PBL mixing coefficients across multi-resolutions. These variations in mixing coefficients relate closely to BC surface concentrations, explaining specific patterns of BC surface concentration distributions. For example, the BC surface concentration south of the

USTC site increases as resolution improves from 25 km to 5 km and 1 km resolutions (Figure 4 and Figure ~~S5~~S8), contrasting with concentration variations simulated in other regions. Our analysis reveals that the turbulent mixing coefficient simulated at 25 km resolution is higher compared to the two higher-resolution simulations in this area (Figure 7 and Figure ~~S7~~S12). Moreover, the spatial distribution of land use types indicates that the 25 km resolution simulation resolves only a single urban land use type in this area (Figure 1b). In contrast, higher resolution simulations capture additional land use types beyond the urban, including lakes, farmland, and shrubs (Figure 1b). The inclusion of these diverse land use types in the higher resolution leads to smaller PBL mixing coefficients in this area, as the surface roughness associated with lakes, farmland, and shrubs is generally lower than that of urban areas. As a result, the reduced vertical mixing in the finer resolution (5 km and 1 km) simulations results in higher BC surface concentrations south of the USTC site.

Additionally, to explore the differences in PBL mixing coefficients across multi-resolutions under uniform land use conditions, we designed another set of sensitivity experiments across three resolutions. As mentioned earlier, the only difference from the baseline experiment was the use of the default USGS land use classification data in the WRF model. As shown in Figure S2, land use type data at different horizontal resolutions are approximately consistent in this setup. All other settings remained identical to those in the baseline experiment.

Figure 10 presents the spatial distribution of PBL mixing coefficients in the sensitivity experiment. Figure 10a illustrates the results across multi-resolutions averaged over the whole day. Similar to the baseline experiment, increasing resolution resolves more spatial details. For example, in the area where the USTC site is located, the PBL mixing coefficient in the 25 km resolution simulation of the sensitivity experiment is approximately 4.3 m^2/s, significantly lower than the 8 m^2/s observed in the baseline experiment. This pattern is consistent across higher resolutions (5 km and 1 km). This finding aligns with the spatial distribution of land use types used in both sets of experiments (Figure 1b and Figure S2). The decrease in mixing coefficients in the sensitivity experiment stems from its land use data failing to resolve urban land

types in urban areas. Figures 10b and 10c show the PBL mixing coefficients of the sensitivity experiment during daytime and nighttime, respectively. Consistent with the baseline experiment, the turbulent mixing coefficients during the day are substantially higher than at night. The PBL coefficients in the nighttime simulations are higher at 5 km and 1 km resolutions compared to the 25 km resolution.

Additionally, Figure S16 further illustrates the differences in the parameterized PBL mixing coefficient between the 25 km resolution and the two higher-resolution simulations under roughly uniform land use conditions. Figure S16c shows that in the city center, the boundary layer mixing coefficient parameterized at 5 km and 1 km resolutions is higher than at the 25 km resolution during nighttime. Since urban areas are primarily flat, topographical differences between different resolutions in urban areas are minimal, almost negligible. Furthermore, because the land use types in the sensitivity experiment are approximately consistent across different resolutions, the main factor responsible for resolution-related differences in the PBL mixing coefficients in urban areas is the grid size. Notably, in areas with significant topographic variations, such as suburban and rural regions, the difference in boundary layer mixing coefficients between 25 km and 5 km/1 km resolutions in the sensitivity experiment strongly correlates with the spatial distribution of topographic differences. This directly demonstrates that topographic height is also a key determinant of boundary layer mixing coefficient distribution. Qian et al. (2010) indicated that the terrain affects the transport and mixing of aerosols and trace gases, as well as their concentrations across multi-resolutions, through its impact on meteorological fields such as wind and the PBL structure. These terrain-related effects are particularly significant in regions with more variable topography. Additionally, Figure S17 shows that the turbulent mixing intensity parameterized at 5 km resolution in the sensitivity experiment is greater than at 1 km resolution. Further analysis of the latitude-pressure cross section of BC concentrations and vertical wind speed flux, as shown in Figure S18, indicates that, similar to the baseline experiment, the 1 km resolution of the sensitivity experiment resolves more small-scale turbulent eddies, capturing more prominent vertical wind speed flux, thus resulting in stronger turbulent mixing.

Through comprehensive analysis of both baseline and sensitivity experiments, we found that within the resolution range of 25 km to 5 km and 1 km, the spatial distribution accuracy of land use types plays a decisive role in parameterizing the PBL mixing coefficient. Finer land use type information at higher resolutions directly alters the spatial distribution of the boundary layer mixing coefficient, with urban surfaces significantly increasing the parameterized PBL mixing coefficient. Therefore, accurately representing land use types, particularly urban surfaces, is critical for parameterizing the PBL mixing coefficient. On the other hand, in the sensitivity experiment, complex terrain areas with significant elevation (such as suburban, rural, and hilly regions) increase mixing coefficients by enhancing surface roughness, whereas this effect is weaker in flat urban areas. Consequently, differences in PBL mixing coefficients across multi-resolutions strongly correlate with terrain precision. Higher resolutions can resolve finer terrain variations, affecting local turbulent mixing (such as terrain-induced mechanical turbulence). This confirms the dominant role of high-resolution terrain and land use information in PBL mixing coefficient parameterization. Notably, in regions where land use types and terrain height remain relatively flat and consistent across different horizontal resolutions in the sensitivity experiments, increasing resolution still leads to enhanced boundary layer mixing coefficients, highlighting the importance of grid size for parameterizing the boundary layer mixing coefficient. In the resolution range from 5 km to 1 km, higher resolution slightly reduces the parameterized boundary layer mixing coefficient. However, the 1 km resolution model resolves more small-scale turbulent eddies, resulting in stronger turbulent mixing at night. In summary, for parameterization of boundary layer mixing coefficients across multi-resolutions, high-resolution surface information is more important in regions with significant changes in land use types and terrain height. Grid size is also crucial in regions with more gradual changes, where higher-resolution grids consistently enhance boundary layer mixing representation. Therefore, to improve PBL mixing coefficient simulation, priority should be given to ensuring accuracy of land use data (especially spatial representation of urban types), precise terrain representation in complex regions, and appropriated grid resolution to enhance turbulent mixing

simulation.

3.3 Simulated BC column concentrations and impacts of turbulent mixing at various horizontal resolutions

3.3.1 Simulated BC column concentrations at three different horizontal resolutions

It is generally accepted that the turbulent mixing process primarily affects pollutant surface concentrations by mixing surface pollutants into higher layers, without altering the column concentration. However, in this study, BC column concentrations exhibit differences across multi-resolutions simulations. Therefore, we further investigate the spatial distribution of BC column concentrations and the main mechanisms behind these variations. Figure ~~10a~~ 11a illustrates the spatial distribution of BC column concentrations simulated at three resolutions, averaged over the whole day. The regional average values for the three resolutions are 2041, 2150, and 2223 ug/m^2, respectively. The 5 km and 1 km resolution simulations yield larger BC column concentrations compared to 25 km resolution simulations. The spatial distribution of BC column concentrations simulated at 25 km resolution is highly consistent with the BC emission distributions (Figure 2), showing high concentrations in central urban areas exceeding 2500 ug/m^2, while regions distant from urban centers demonstrate lower concentrations, generally below 2100 ug/m^2. The 5 km resolution simulation results indicate peak column concentrations concentrated in urban areas and spread around, with the southwestern area approaching 2250 ug/m^2. The 1 km resolution simulation results yield the largest BC column concentrations and demonstrate the most pronounced diffusion tendency, with most areas exceeding 2250 ug/m^2. Figure ~~10b~~ 11b and Figure ~~10c~~ 11c reveal lower BC column concentrations during the daytime compared to those at night, with a more pronounced dispersion trend of column concentrations simulated at night. Figure ~~S11~~ S19 depicts the differences in BC column concentrations between 25 km and 5 km resolutions, as well as between 25 km and 1 km resolutions, revealing that BC column concentrations in coarser resolutions are marginally lower than those in finer resolutions (5 km and 1 km) in most of the study areas. On the other hand, the BC column concentration simulated at 1 km resolution are

larger than those at 5 km resolution, as shown in Figure ~~S12~~S20. In conclusion, BC column concentrations increases with increased resolutions, accompanied by a more pronounced dispersion tendency towards higher and farther areas.

3.3.2 Impacts of turbulent mixing on BC column concentrations at three different horizontal resolutions

We further analyze the mechanisms underlying the differences in BC column concentrations across multi-resolutions in urban areas. Figure ~~11a~~ 12a displays the vertical profiles of BC concentrations averaged over the study area. The BC profiles at 25 km resolution exhibit significant variability, generally decreasing from the surface to higher altitudes. The near-surface BC concentration is approximately three times higher than those at high altitudes, with surface concentrations reaching about 3 ug/m^3. At an altitude of 100 m, the concentration drops to 1 ug/m^3, while above this elevation, the BC concentration is less than 1 ug/m^3. Substantial disparities exist among multi-resolutions simulations in the vertical profiles of BC concentrations. Our analyses above have shown that near the surface, the parameterized mixing coefficients and directly resolved vertical wind speed flux are lower at 25 km resolution compared to 5 km and 1 km resolutions, reducing the vertical mixing of pollutants in 25 km resolution simulations. Thus, BC concentrations at 25 km resolution are higher near the surface and lower at higher altitudes compared to high-resolution (5 km and 1 km) simulations. Moreover, the parametrized PBL mixing coefficient at 1 km resolution is lower than at 5 km resolution in the atmosphere, but the directly resolved upward vertical wind speed flux by the model dynamic process reaches higher altitudes at 1 km resolution compared to 5 km resolution. Thus, due to the combined effects of these two processes, the intensity of turbulent mixing is similar between the 5 km and 1 km resolutions at near-surface levels, whereas it is greater at 1 km resolution than at 5 km resolution at higher altitudes. In numerical models, sub-grid scale (SGS) turbulent diffusion is typically simulated by parameterization schemes. However, as model resolution increases, such as achieving 1 km resolution, the turbulent mixing is increasingly resolved by the dynamical framework of model. This advancement allows the model to capture

dynamic structures and small-scale turbulence more accurately, significantly enhancing the strength of turbulent mixing. The direct resolve of dynamic processes reduces reliance on traditional parameterization schemes, thereby decreasing the PBL mixing coefficient parameterized at finer resolutions. In conclusion, at higher altitudes, the enhanced turbulent mixing efficiently facilitates more ground-emitted pollutants to higher height as resolution increases. Thus, BC concentrations at 5 km and 1 km resolution are similar near surface, with 1 km resolution yielding the largest concentrations at higher altitudes.

To further investigate the BC column concentrations and their dispersion tendency towards farther areas, we analyzed the vertical profile of wind speed at three resolutions averaged over the study area, as shown in Figure ~~11b~~12b. The vertical profile of wind speed is relatively consistent across the three resolutions. From the ground to higher altitudes, the overall wind speed gradually increases, transitioning from low speeds near the surface to higher speeds aloft. Near the ground, the simulated average wind speed is approximately 1 m/s, increasing to 4 m/s at an altitude of 1 km, and reaching an average of about 7 m/s at an altitude of 2 km. In the upper atmosphere, characterized by larger wind speeds, pollutants mixed up from near-surface can be transported and dispersed farther. As previously mentioned, BC simulated in higher-resolution simulations can be transported to higher altitudes, thus dispersing over greater distances by stronger winds. Therefore, as the resolution increases, the trend of diffusion towards farther regions in the simulated BC column concentrations becomes more pronounced.

As previously discussed, higher-resolution simulations facilitate BC transport to greater altitudes and further distances. This phenomenon extends its atmospheric lifetime, consequently resulting in increased column concentrations. Bauer et al. (2013) noted that turbulent mixing and convective transport processes play a critical role in determining BC lifetimes. Figure ~~12~~ 13 illustrates the spatial distribution of BC lifetime, calculated by dividing the BC column concentration by the dry deposition flux. It demonstrates that BC lifetime gradually lengthens as resolution increases. The average lifetime of BC column concentrations in the study area is 344 h, 350 h, and 382 h for 25 km, 5 km, and 1 km resolutions, respectively. These results clearly demonstrate that

BC simulated at higher resolutions exhibits prolonged atmospheric residence times. Consequently, the BC column concentration is higher in high-resolution simulations.

4. Conclusion and Discussion

Turbulent mixing plays a crucial role in urban pollutant transport by enhancing the diffusion of atmospheric pollutants. Current atmospheric models often underestimate turbulent exchange within stable nocturnal boundary layers, and the turbulent mixing varies markedly across different model horizontal resolutions. However, few studies have analyzed how turbulent mixing processes across multi-resolutions affect pollutant concentrations in urban areas. Therefore, our goal is to elucidate the variations in pollutant concentrations across multi-resolutions and investigate the influence of turbulent mixing on pollutant concentrations at various resolutions.

We conducted a three-nested WRF-Chem simulation at 25 km, 5 km, and 1 km resolutions in the Hefei area. BC surface concentrations decrease as resolution increases from 25 km to 5 km and further to 1 km but are similar at 5 km and 1 km resolutions, showing significant diurnal variations with higher concentrations at night and lower during the daytime. The BC surface concentrations across multi-resolutions align well with USTC site observations during daytime but are overestimated at night, with this overestimation decreasing at higher-resolution (5 km and 1 km). Disparities in BC surface concentrations between the two finer-resolution and the 25 km resolution simulations are primarily attributable to nocturnal concentrations. In addition, the diurnal variation of $PM_{2.5}$ surface concentrations simulated at different resolutions follows the same trend as the observed concentrations at the national monitoring sites, with slight underestimation during daytime and overestimation at night. The PBL mixing coefficient plays a crucial role in controlling surface ~~pollutant~~ particulate matter concentrations at night. Larger nighttime PBL mixing coefficients and higher vertical wind speed flux at 5 km and 1 km resolutions compared to 25 km resolution near the surface result in lower BC surface concentrations. However, the PBL mixing coefficient at 5 km is larger than at 1 km resolution. Moreover, the upward vertical wind speed flux

resolved at 1 km resolution reaches higher altitudes compared to 25 km and 5 km resolutions, indicating more small-scale eddies and resulting in enhanced turbulent mixing. Consequently, near the surface, the combined effects of parametrized PBL mixing coefficient and the directly resolved vertical wind speed flux lead to similar BC surface concentrations at 5 km and 1 km resolutions.

Further analysis reveals that the spatial distribution of PBL mixing coefficients is influenced by both land use types and terrain heights. The turbulent mixing coefficient correlates with the spatial distribution of land use types at smaller scales, with urban underlying surfaces notably increasing the parameterized PBL mixing coefficient.~~,~~ The mixing coefficient also strongly correlates with~~while correlating with~~ terrain heights at larger scales, particularly in ~~in~~ regions with complex topography and significant elevation differences,~~ and complicated flow patterns~~ where higher terrain substantially enhances mixing coefficients. ~~.~~This correlation can be attributed to the interrelationship among turbulent mixing coefficients, friction velocity, terrain, and land use types. The static database of terrain and land use types employed as model input determines the surface roughness. Higher surface roughness typically leads to greater fiction velocity, subsequently increasing the PBL mixing coefficients. Moreover, in regions where land use types and terrain height remain relatively flat and consistent across multi-resolutions, increasing resolution still enhances boundary layer mixing coefficients, highlighting the importance of grid size. ~~–~~Thus, both surface information and grid resolution are crucial for accurately parameterizing PBL mixing coefficients, with priority given to accurate land use data, precise terrain representation, and higher grid resolution to improve turbulent mixing simulations.

In WRF-Chem, the mixing coefficients of chemical species are clipped to empirically chosen thresholds of 1 m^2/s over rural areas and 2 m^2/s over urban areas to prevent unrealistically low values. These thresholds are modified based on differences in anthropogenic CO and primary $PM_{2.5}$ emissions between rural and urban regions. Importantly, this adjustment applies exclusively to gases and not to aerosols when the MOSAIC or MADE/SORGAM aerosol schemes are used. This is because the adjustment does not couple with the aerosol PBL mixing scheme in WRF-Chem,

although potential modifications could be made for compatibility with the MOSAIC or MADE/SORGAM scheme. Thus, the boundary layer mixing coefficient for gases is implicitly influenced by emission resolution rather than directly controlled by model resolution. In this study, this treatment caused gas mixing coefficients to converge across different horizontal resolutions, preventing us from accurately assessing the impact of horizontal resolution on gas turbulent mixing. For aerosols, however, the original PBL mixing coefficients are retained, which are directly parametrized from boundary layer parameterization schemes. Therefore, our focus is mainly on particulate matter in this analysis and we omitted this modification for gases.

The variations in turbulent mixing across multi-resolution simulations not only affect the BC surface concentration but also lead to different BC column concentrations. BC column concentrations increase with improved resolutions, accompanied by a more pronounced diffusion tendency towards higher altitudes and distant regions. Throughout the atmosphere, turbulent mixing intensifies with improved resolutions, resulting in pollutants being transported to higher altitudes. Concurrently, wind speed increases with altitude, facilitating the pollutants which are mixed to higher altitudes to be spread farther. Consequently, BC simulated at higher resolution is transported to greater altitudes and dispersed to farther regions, thus persisting in the atmosphere for longer periods and leading to larger lifetimes. As a result, BC column concentrations increase with finer resolutions.

This study highlights the importance of model horizontal resolution in simulating the dispersion of atmospheric pollutants. We observed that the enhanced turbulent mixing strength in high-resolution can more accurately reproduce the vertical and horizontal distribution of pollutants, thus aligning the simulated pollutant surface concentrations more closely with actual observations. In contrast, turbulent mixing in low-resolution simulations, primarily depending on boundary layer parameterizations, may not adequately capture the dynamics of turbulence, leading to discrepancies between the simulated and actual distribution of pollutants, particularly during the night with stable boundary condition. Future research should focus on improving PBL parameterization schemes to enhance model performance at lower resolutions, thereby

better serving the needs of air pollution control and environmental management.

Moreover, we have noted that the parameterized PBL mixing coefficient decreases when transitioning from 5 km to 1 km resolution, alongside an increase in vertical wind speed flux which represents turbulent mixing directly resolved by the dynamical processes. This trend suggests that if the resolution was further increased to LES scales, the parameterized PBL mixing coefficient might diminish significantly, potentially approaching zero, while the turbulence mixing resolved directly by the dynamics would intensify considerably. At LES scales, the majority of turbulent mixing is directly resolved, capturing the atmospheric dynamical processes and turbulent exchanges more realistically, thereby reducing the simulation biases caused by parameterization errors. This shift diminishes reliance on traditional boundary layer parameterizations to simulate turbulent mixing, leading to a substantial reduction in the parameterized boundary layer mixing coefficient. By capturing the finer details of atmospheric dynamics, the model provides a more realistic representation of turbulent mixing and related physical processes, which is crucial for understanding weather patterns, climate variability, and pollutant dispersion. However, due to the huge computational resources required for LES simulation, we have not yet performed an analysis at the LES scale, but it is worth further exploring in the future.

Our analysis also found that higher-resolution facilitate transport over greater distances, suggesting that inter-city pollutant diffusion can be affected by model resolution, with coarse-resolution potentially reducing long-range transport and inter-urban impacts. While previous studies have examined pollutant formation mechanisms at specific resolutions and explored the physical and chemical interactions among megacities, few have considered the impacts of different resolutions on long-range transport between cities. Due to computational cost constraints, inter-urban impacts are not discussed in this study but deserve further investigation in the future. ~~Furthermore, this study focuses exclusively on BC, a primary aerosol species, while the impact of grid resolution on secondary aerosols may differ. Future investigations could expand this analysis to encompass a wider spectrum of pollutant species.~~ Finally, while vertical resolution is held constant in our study, we recognize that it could influence the

interpretation of the turbulence processes in certain scenarios, especially in regions with complex vertical structures. Therefore, future work could systematically explore the interplay between vertical resolution and pollutant concentration or aerosol-boundary layer feedbacks.

Data availability. The release version of WRF-Chem can be downloaded from http://www2.mmm.ucar.edu/wrf/users/download/get_source.html. The updated USTC version of WRF-Chem can be downloaded from http://aemol.ustc.edu.cn/product/list/ or contact chunzhao@ustc.edu.cn. Additionally, code modifications will be incorporated into the release version of WRF-Chem in the future.

Author contributions. Zining Yang and Chun Zhao designed the experiments and conducted and analyzed the simulations. All authors contributed to the discussion and final version of the paper.

Competing interests. The contact author has declared that none of the authors has any competing interests.

Acknowledgments. This research was supported by the National Key Research and Development Program of China (No. 2022YFC3700701), the Strategic Priority Research Program of Chinese Academy of Sciences (XDB0500303), National Natural Science Foundation of China (41775146), the USTC Research Funds of the Double First-Class Initiative (YD2080002007, KY2080000114), the Science and Technology Innovation Project of Laoshan Laboratory (LSKJ202300305), and the National Key Scientific and Technological Infrastructure project "Earth System Numerical Simulation Facility" (EarthLab). The study used the computing resources from the Supercomputing Center of the University of Science and Technology of China (USTC) and the Qingdao Supercomputing and Big Data Center.

Reference

Banks, R. F. and Baldasano, J. M.: Impact of WRF model PBL schemes on air quality simulations over Catalonia, Spain, Science of the Total Environment, 572, 98-113, https://doi.org/10.1016/j.scitotenv.2016.07.167, 2016.

Bauer, S. E., Bausch, A., Nazarenko, L., Tsigaridis, K., Xu, B., Edwards, R., Bisiaux, M., and McConnell, J.: Historical and future black carbon deposition on the three ice caps: Ice core measurements and model simulations from 1850 to 2100, Journal of Geophysical Research-Atmospheres, 118, 7948-7961, https://doi.org/10.1002/jgrd.50612, 2013.

Berger, A., Barbet, C., Leriche, M., Deguillaume, L., Mari, C., Chaumerliac, N., Begue, N., Tulet, P., Gazen, D., and Escobar, J.: Evaluation of Meso-NH and WRF-CHEM simulated gas and aerosol chemistry over Europe based on hourly observations, Atmospheric Research, 176, 43-63, https://doi.org/10.1016/j.atmosres.2016.02.006, 2016.

Carter: Implementation of the SAPRC-99 chemical mechanism into the models-3 framework, 2000.

Chan, C. K. and Yao, X.: Air pollution in mega cities in China, Atmospheric Environment, 42, 1-42, https://doi.org/10.1016/j.atmosenv.2007.09.003, 2008.

Chapman, E. G., Gustafson, W. I., Jr., Easter, R. C., Barnard, J. C., Ghan, S. J., Pekour, M. S., and Fast, J. D.: Coupling aerosol-cloud-radiative processes in the WRF-Chem model: Investigating the radiative impact of elevated point sources, Atmospheric Chemistry and Physics, 9, 945-964, https://doi.org/10.5194/acp-9-945-2009, 2009.

Chen, F. and Dudhia, J.: Coupling an Advanced Land Surface–Hydrology Model with the Penn State–NCAR MM5 Modeling System. Part I: Model Implementation and Sensitivity, Monthly Weather Review, 129, 569-585, 2001.

Chen, Y., Zhao, C., Zhang, Q., Deng, Z., Huang, M., and Ma, X.: Aircraft study of Mountain Chimney Effect of Beijing, China, Journal of Geophysical Research-Atmospheres, 114, https://doi.org/10.1029/2008jd010610, 2009.

CMA, 2018: Technical Specifications for Maintenance of Regional Automatic Weather Stations. QX/T 465–2018. (in Chinese). Available at: http://cmastd.cmatc.cn/standardView.jspx?id=3076. Accessed on 5 May 2022., 2018.

Costa, F. D., Acevedo, O. C., Mombach, J. C. M., and Degrazia, G. A.: A Simplified Model for Intermittent Turbulence in the Nocturnal Boundary Layer, Journal of the Atmospheric Sciences, 68, 1714-1729, https://doi.org/10.1175/2011jas3655.1, 2011.

Cuchiara, G. C., Li, X., Carvalho, J., and Rappenglueck, B.: Intercomparison of planetary boundary layer parameterization and its impacts on surface ozone concentration in the WRF-Chem model for a case study in Houston/Texas, Atmospheric Environment, 96, 175-185, https://doi.org/10.1016/j.atmosenv.2014.07.013, 2014.

Dentener, F., Kinne, S., Bond, T., Boucher, O., Cofala, J., Generoso, S., Ginoux, P., Gong, S., Hoelzemann, J. J., Ito, A., Marelli, L., Penner, J. E., Putaud, J. P., Textor, C., Schulz, M., van der Werf, G. R., and Wilson, J.: Emissions of primary aerosol and precursor gases in the years 2000 and 1750 prescribed data-sets for AeroCom, Atmospheric Chemistry and Physics, 6, 4321-4344, https://doi.org/10.5194/acp-6-4321-2006, 2006.

Du, Q., Zhao, C., Zhang, M., Dong, X., Chen, Y., Liu, Z., Hu, Z., Zhang, Q., Li, Y., Yuan, R., and Miao, S.: Modeling diurnal variation of surface $PM_{2.5}$ concentrations over East China with WRF-Chem: impacts from boundary-layer mixing and anthropogenic emission, Atmospheric Chemistry and Physics, 20, 2839-2863, https://doi.org/10.5194/acp-20-2839-2020, 2020.

Estevez, J., Gavilan, P., and Giraldez, J. V.: Guidelines on validation procedures for meteorological data from automatic weather stations, Journal of Hydrology, 402, 144-154, https://doi.org/10.1016/j.jhydrol.2011.02.031, 2011.

Fountoukis, C., Koraj, D., van der Gon, H. A. C. D., Charalampidis, P. E., Pilinis, C., and Pandis, S. N.: Impact of grid resolution on the predicted fine PM by a regional 3-D chemical transport model, Atmospheric Environment, 68, 24-32,

https://doi.org/10.1016/j.atmosenv.2012.11.008, 2013.

Grell, G. A., Peckham, S. E., Schmitz, R., McKeen, S. A., Frost, G., Skamarock, W. C., and Eder, B.: Fully coupled "online" chemistry within the WRF model, Atmospheric Environment, 39, 6957-6975, https://doi.org/10.1016/j.atmosenv.2005.04.027, 2005.

Gustafson, W. I., Jr., Qian, Y., and Fast, J. D.: Downscaling aerosols and the impact of neglected subgrid processes on direct aerosol radiative forcing for a representative global climate model grid spacing, Journal of Geophysical Research-Atmospheres, 116, https://doi.org/10.1029/2010jd015480, 2011.

Gustafson, W. I., Jr., Chapman, E. G., Ghan, S. J., Easter, R. C., and Fast, J. D.: Impact on modeled cloud characteristics due to simplified treatment of uniform cloud condensation nuclei during NEAQS 2004, Geophysical Research Letters, 34, https://doi.org/10.1029/2007gl030021, 2007.

Han, S., Bian, H., Tie, X., Xie, Y., Sun, M., and Liu, A.: Impact of nocturnal planetary boundary layer on urban air pollutants: Measurements from a 250-m tower over Tianjin, China, Journal of Hazardous Materials, 162, 264-269, https://doi.org/10.1016/j.jhazmat.2008.05.056, 2009.

Holmes, H. A., Sriramasamudram, J. K., Pardyjak, E. R., and Whiteman, C. D.: Turbulent Fluxes and Pollutant Mixing during Wintertime Air Pollution Episodes in Complex Terrain, Environmental Science & Technology, 49, 13206-13214, https://doi.org/10.1021/acs.est.5b02616, 2015.

Hong, S.-Y., Noh, Y., and Dudhia, J.: A new vertical diffusion package with an explicit treatment of entrainment processes, Monthly Weather Review, 134, 2318-2341, https://doi.org/10.1175/mwr3199.1, 2006.

Hu, Z., Huang, J., Zhao, C., Bi, J., Jin, Q., Qian, Y., Leung, L. R., Feng, T., Chen, S., and Ma, J.: Modeling the contributions of Northern Hemisphere dust sources to dust outflow from East Asia, Atmospheric Environment, 202, 234-243, https://doi.org/10.1016/j.atmosenv.2019.01.022, 2019.

Iacono, M. J., Mlawer, E. J., Clough, S. A., and Morcrette, J. J.: Impact of an improved longwave radiation model, RRTM, on the energy budget and thermodynamic

properties of the NCAR community climate model, CCM3, Journal of Geophysical Research-Atmospheres, 105, 14873-14890, https://doi.org/10.1029/2000jd900091, 2000.

Janssens-Maenhout, G., Crippa, M., Guizzardi, D., Dentener, F., Muntean, M., Pouliot, G., Keating, T., Zhang, Q., Kurokawa, J., Wankmueller, R., van der Gon, H. D., Kuenen, J. J. P., Klimont, Z., Frost, G., Darras, S., Koffi, B., and Li, M.: HTAP_v2.2: a mosaic of regional and global emission grid maps for 2008 and 2010 to study hemispheric transport of air pollution, Atmospheric Chemistry and Physics, 15, 11411-11432, https://doi.org/10.5194/acp-15-11411-2015, 2015.

Jia, W. and Zhang, X.: Impact of modified turbulent diffusion of $PM_{2.5}$ aerosol in WRF-Chem simulations in eastern China, Atmospheric Chemistry and Physics, 21, 16827-16841, https://doi.org/10.5194/acp-21-16827-2021, 2021.

Jia, W., Zhang, X., Zhang, H., and Ren, Y.: Application of Turbulent Diffusion Term of Aerosols in Mesoscale Model, Geophysical Research Letters, 48, https://doi.org/10.1029/2021gl093199, 2021.

Jiang, L. and Hu, J.: Influence of the lowest model level height and vertical grid resolution on mesoscale meteorological modeling, Atmospheric Research, 296, https://doi.org/10.1016/j.atmosres.2023.107066, 2023.

Jiang, L., Bessagnet, B., Meleux, F., Couvidat, F., Tognet, F., and Hu, J.: The role of vertical grid resolution and turbulent diffusion uncertainty on chemical transport modeling, Atmospheric Research, 312, https://doi.org/10.1016/j.atmosres.2024.107759, 2024.

Kain, J. S.: The Kain-Fritsch convective parameterization: An update, Journal of Applied Meteorology, 43, 170-181, https://doi.org/10.1175/1520-0450(2004)043<0170:Tkcpau>2.0.Co;2, 2004.

Kim, S. W.: The Influence of PBL Parameterizations on the Distributions of Chemical Species in a Mesoscale Chemical Transport Model, WRF-Chem,

Kuhn, L., Beirle, S., Kumar, V., Osipov, S., Pozzer, A., Boesch, T., Kumar, R., and Wagner, T.: On the influence of vertical mixing, boundary layer schemes, and temporal emission profiles on tropospheric NO2 in WRF-Chem - comparisons to

in situ, satellite, and MAX-DOAS observations, Atmospheric Chemistry and Physics, 24, 185-217, https://doi.org/10.5194/acp-24-185-2024, 2024.

Li, H., Li, L., Huang, C., An, J., Yan, R., Huang, H., Wang, Y., Lu, Q., Wang, Q., Lou, S., Wang, H., Zhou, M., Tao, S., Qiao, L., and Chen, M.: Ozone Source Apportionment at Urban Area during a Typical Photochemical Pollution Episode in the Summer of 2013 in the Yangtze River Delta, Environmental Science, 36, 1-10, 2015.

Li, L., An, J., Huang, L., Yan, R., Huang, C., and Yarwood, G.: Ozone source apportionment over the Yangtze River Delta region, China: Investigation of regional transport, sectoral contributions and seasonal differences, Atmospheric Environment, 202, 269-280, https://doi.org/10.1016/j.atmosenv.2019.01.028, 2019.

Li, M., Liu, H., Geng, G., Hong, C., Liu, F., Song, Y., Tong, D., Zheng, B., Cui, H., Man, H., Zhang, Q., and He, K.: Anthropogenic emission inventories in China: a review, National Science Review, 4, 834-866, https://doi.org/10.1093/nsr/nwx150, 2017a.

Li, M., Zhang, Q., Kurokawa, J.-i., Woo, J.-H., He, K., Lu, Z., Ohara, T., Song, Y., Streets, D. G., Carmichael, G. R., Cheng, Y., Hong, C., Huo, H., Jiang, X., Kang, S., Liu, F., Su, H., and Zheng, B.: MIX: a mosaic Asian anthropogenic emission inventory under the international collaboration framework of the MICS-Asia and HTAP, Atmospheric Chemistry and Physics, 17, 935-963, https://doi.org/10.5194/acp-17-935-2017, 2017b.

Li, Q., Zhang, H., Jin, X., Cai, X., and Song, Y.: Mechanism of haze pollution in summer and its difference with winter in the North China Plain, Science of the Total Environment, 806, https://doi.org/10.1016/j.scitotenv.2021.150625, 2022.

Li, Q., Wu, B., Liu, J., Zhang, H., Cai, X., and Song, Y.: Characteristics of the atmospheric boundary layer and its relation with $PM_{2.5}$ during haze episodes in winter in the North China Plain, Atmospheric Environment, 223, https://doi.org/10.1016/j.atmosenv.2020.117265, 2020.

Li, X.-B., Wang, D.-S., Lu, Q.-C., Peng, Z.-R., and Wang, Z.-Y.: Investigating vertical

distribution patterns of lower tropospheric PM_{2.5} using unmanned aerial vehicle measurements, Atmospheric Environment, 173, 62-71, https://doi.org/10.1016/j.atmosenv.2017.11.009, 2018.

Liu, C., Huang, J., Wang, Y., Tao, X., Hu, C., Deng, L., Xu, J., Xiao, H.-W., Luo, L., Xiao, H.-Y., and Xiao, W.: Vertical distribution of PM_{2.5} and interactions with the atmospheric boundary layer during the development stage of a heavy haze pollution event, Science of the Total Environment, 704, https://doi.org/10.1016/j.scitotenv.2019.135329, 2020.

Liu, C., Chen, R., Sera, F., Vicedo-Cabrera, A. M., Guo, Y., Tong, S., Coelho, M. S. Z. S., Saldiva, P. H. N., Lavigne, E., Matus, P., Ortega, N. V., Garcia, S. O., Pascal, M., Stafoggia, M., Scortichini, M., Hashizume, M., Honda, Y., Hurtado-Diaz, M., Cruz, J., Nunes, B., Teixeira, J. P., Kim, H., Tobias, A., Iniguez, C., Forsberg, B., Astrom, C., Ragettli, M. S., Guo, Y.-L., Chen, B.-Y., Bell, M. L., Wright, C. Y., Scovronick, N., Garland, R. M., Milojevic, A., Kysely, J., Urban, A., Orru, H., Indermitte, E., Jaakkola, J. J. K., Ryti, N. R. I., Katsouyanni, K., Analitis, A., Zanobetti, A., Schwartz, J., Chen, J., Wu, T., Cohen, A., Gasparrini, A., and Kan, H.: Ambient Particulate Air Pollution and Daily Mortality in 652 Cities, New England Journal of Medicine, 381, 705-715, https://doi.org/10.1056/NEJMoa1817364, 2019.

Liu, H., Yuan, R., Mei, J., Sun, J., Liu, Q., and Wang, Y.: Scale Properties of Anisotropic and Isotropic Turbulence in the Urban Surface Layer, Boundary-Layer Meteorology, 165, 277-294, https://doi.org/10.1007/s10546-017-0272-z, 2017.

Ma, T., Duan, F., He, K., Qin, Y., Tong, D., Geng, G., Liu, X., Li, H., Yang, S., Ye, S., Xu, B., Zhang, Q., and Ma, Y.: Air pollution characteristics and their relationship with emissions and meteorology in the Yangtze River Delta region during 2014-2016, Journal of Environmental Sciences, 83, 8-20, https://doi.org/10.1016/j.jes.2019.02.031, 2019.

McKeen, S., Chung, S. H., Wilczak, J., Grell, G., Djalalova, I., Peckham, S., Gong, W., Bouchet, V., Moffet, R., Tang, Y., Carmichael, G. R., Mathur, R., and Yu, S.: Evaluation of several $PM_{2.5}$ forecast models using data collected during the

ICARTT/NEAQS 2004 field study, Journal of Geophysical Research-Atmospheres, 112, https://doi.org/10.1029/2006jd007608, 2007.

Miao, Y., Li, J., Miao, S., Che, H., Wang, Y., Zhang, X., Zhu, R., and Liu, S.: Interaction Between Planetary Boundary Layer and PM_{2.5} Pollution in Megacities in China: a Review, Current Pollution Reports, 5, 261-271, https://doi.org/10.1007/s40726-019-00124-5, 2019.

Mlawer, E. J., Taubman, S. J., Brown, P. D., Iacono, M. J., and Clough, S. A.: Radiative transfer for inhomogeneous atmospheres: RRTM, a validated correlated-k model for the longwave, Journal of Geophysical Research-Atmospheres, 102, 16663-16682, https://doi.org/10.1029/97jd00237, 1997.

Morrison, H., Thompson, G., and Tatarskii, V.: Impact of Cloud Microphysics on the Development of Trailing Stratiform Precipitation in a Simulated Squall Line: Comparison of One- and Two-Moment Schemes, Monthly Weather Review, 137, 991-1007, https://doi.org/10.1175/2008mwr2556.1, 2009.

Peng, Y., Wang, H., Li, Y., Liu, C., Zhao, T., Zhang, X., Gao, Z., Jiang, T., Che, H., and Zhang, M.: Evaluating the performance of two surface layer schemes for the momentum and heat exchange processes during severe haze pollution in Jing-Jin-Ji in eastern China, Atmospheric Chemistry and Physics, 18, 17421-17435, https://doi.org/10.5194/acp-18-17421-2018, 2018.

Pierce, A. M., Loria-Salazar, S. M., Holmes, H. A., and Gustin, M. S.: Investigating horizontal and vertical pollution gradients in the atmosphere associated with an urban location in complex terrain, Reno, Nevada, USA, Atmospheric Environment, 196, 103-117, https://doi.org/10.1016/j.atmosenv.2018.09.063, 2019.

Qian, Y., Gustafson, W. I., Jr., and Fast, J. D.: An investigation of the sub-grid variability of trace gases and aerosols for global climate modeling, Atmospheric Chemistry and Physics, 10, 6917-6946, https://doi.org/10.5194/acp-10-6917-2010, 2010.

Quan, J., Dou, Y., Zhao, X., Liu, Q., Sun, Z., Pan, Y., Jia, X., Cheng, Z., Ma, P., Su, J., Xin, J., and Liu, Y.: Regional atmospheric pollutant transport mechanisms over the North China Plain driven by topography and planetary boundary layer processes,

Atmospheric Environment, 221, https://doi.org/10.1016/j.atmosenv.2019.117098, 2020.

Ren, Y., Zhang, H., Wei, W., Cai, X., and Song, Y.: Determining the fluctuation of $PM_{2.5}$ mass concentration and its applicability to Monin-Obukhov similarity, Science of the Total Environment, 710, https://doi.org/10.1016/j.scitotenv.2019.136398, 2020.

Ren, Y., Zhang, H., Wei, W., Cai, X., Song, Y., and Kang, L.: A study on atmospheric turbulence structure and intermittency during heavy haze pollution in the Beijing area, Science China-Earth Sciences, 62, 2058-2068, https://doi.org/10.1007/s11430-019-9451-0, 2019a.

Ren, Y., Zhang, H., Wei, W., Wu, B., Cai, X., and Song, Y.: Effects of turbulence structure and urbanization on the heavy haze pollution process, Atmospheric Chemistry and Physics, 19, 1041-1057, https://doi.org/10.5194/acp-19-1041-2019, 2019b.

Ren, Y., Zhang, H., Zhang, X., Li, Q., Cai, X., Song, Y., Kang, L., and Zhu, T.: Temporal and spatial characteristics of turbulent transfer and diffusion coefficient of $PM_{2.5}$, Science of the Total Environment, 782, https://doi.org/10.1016/j.scitotenv.2021.146804, 2021.

Riccobono, F., Schobesberger, S., Scott, C. E., Dommen, J., Ortega, I. K., Rondo, L., Almeida, J., Amorim, A., Bianchi, F., Breitenlechner, M., David, A., Downard, A., Dunne, E. M., Duplissy, J., Ehrhart, S., Flagan, R. C., Franchin, A., Hansel, A., Junninen, H., Kajos, M., Keskinen, H., Kupc, A., Kuerten, A., Kvashin, A. N., Laaksonen, A., Lehtipalo, K., Makhmutov, V., Mathot, S., Nieminen, T., Onnela, A., Petaja, T., Praplan, A. P., Santos, F. D., Schallhart, S., Seinfeld, J. H., Sipila, M., Spracklen, D. V., Stozhkov, Y., Stratmann, F., Tome, A., Tsagkogeorgas, G., Vaattovaara, P., Viisanen, Y., Vrtala, A., Wagner, P. E., Weingartner, E., Wex, H., Wimmer, D., Carslaw, K. S., Curtius, J., Donahue, N. M., Kirkby, J., Kulmala, M., Worsnop, D. R., and Baltensperger, U.: Oxidation Products of Biogenic Emissions Contribute to Nucleation of Atmospheric Particles, Science, 344, 717-721, https://doi.org/10.1126/science.1243527, 2014.

Skamarock, W. C., Klemp, J. B., Dudhia, J., Gill, D. O., and Powers, J. G.: A

Description of the Advanced Research WRF Version 3, NCAR Technical Note NCAR/TN-475+STR. June 2008. Mesoscale and Microscale Meteorology Division. National Center for Atmospheric Research. Boulder, 475, 2008.

Stull, R. B.: An Introduction to Boundary Layer Meteorology, An Introduction to Boundary Layer Meteorology1988.

Sun, T., Che, H., Qi, B., Wang, Y., Dong, Y., Xia, X., Wang, H., Gui, K., Zheng, Y., Zhao, H., Ma, Q., Du, R., and Zhang, X.: Aerosol optical characteristics and their vertical distributions under enhanced haze pollution events: effect of the regional transport of different aerosol types over eastern China, Atmospheric Chemistry and Physics, 18, 2949-2971, https://doi.org/10.5194/acp-18-2949-2018, 2018.

Sun, Y., Song, T., Tang, G., and Wang, Y.: The vertical distribution of PM_{2.5} and boundary-layer structure during summer haze in Beijing, Atmospheric Environment, 74, 413-421, https://doi.org/10.1016/j.atmosenv.2013.03.011, 2013.

Tao, H., Xing, J., Zhou, H., Pleim, J., Ran, L., Chang, X., Wang, S., Chen, F., Zheng, H., and Li, J.: Impacts of improved modeling resolution on the simulation of meteorology, air quality, and human exposure to $PM_{2.5}$, O_3 in Beijing, China, Journal of Cleaner Production, 243, https://doi.org/10.1016/j.jclepro.2019.118574, 2020.

Tuccella, P., Curci, G., Visconti, G., Bessagnet, B., Menut, L., and Park, R. J.: Modeling of gas and aerosol with WRF-Chem over Europe: Evaluation and sensitivity study, Journal of Geophysical Research-Atmospheres, 117, https://doi.org/10.1029/2011jd016302, 2012.

Von Kuhlmann, R., Lawrence, M. G., Crutzen, P. J., and Rasch, P. J.: A model for studies of tropospheric ozone and nonmethane hydrocarbons: Model description and ozone results, Journal of Geophysical Research-Atmospheres, 108, https://doi.org/10.1029/2002jd002893, 2003.

Wang, H., Peng, Y., Zhang, X., Liu, H., Zhang, M., Che, H., Cheng, Y., and Zheng, Y.: Contributions to the explosive growth of $PM_{2.5}$ mass due to aerosol-radiation feedback and decrease in turbulent diffusion during a red alert heavy haze in

Beijing-Tianjin-Hebei, China, Atmospheric Chemistry and Physics, 18, 17717-17733, https://doi.org/10.5194/acp-18-17717-2018, 2018.

Wei, W., Zhang, H., Cai, X., Song, Y., Bian, Y., Xiao, K., and Zhang, H.: Influence of Intermittent Turbulence on Air Pollution and Its Dispersion in Winter 2016/2017 over Beijing, China, Journal of Meteorological Research, 34, 176-188, https://doi.org/10.1007/s13351-020-9128-4, 2020.

Wei, W., Zhang, H., Wu, B., Huang, Y., Cai, X., Song, Y., and Li, J.: Intermittent turbulence contributes to vertical dispersion of $PM_{2.5}$ in the North China Plain: cases from Tianjin, Atmospheric Chemistry and Physics, 18, 12953-12967, https://doi.org/10.5194/acp-18-12953-2018, 2018.

Wiedinmyer, C., Akagi, S. K., Yokelson, R. J., Emmons, L. K., Al-Saadi, J. A., Orlando, J. J., and Soja, A. J.: The Fire INventory from NCAR (FINN): a high resolution global model to estimate the emissions from open burning, Geoscientific Model Development, 4, 625-641, https://doi.org/10.5194/gmd-4-625-2011, 2011.

Wild, O., Zhu, X., and Prather, M. J.: Fast-j: Accurate simulation of in- and below-cloud photolysis in tropospheric chemical models, Journal of Atmospheric Chemistry, 37, 245-282, https://doi.org/10.1023/a:1006415919030, 2000.

WRAP – Western Regional Air Partnership: 2002 Fire Emission Inventory for the WRAP Region – Phase II, Project No.178-6, available at: http://www.wrapair.org/forums/fejf/tasks/FEJFtask7PhaseII.html (last access: 30 September 2021), 2005.

Wu, H., Li, Z., Li, H., Luo, K., Wang, Y., Yan, P., Hu, F., Zhang, F., Sun, Y., Shang, D., Liang, C., Zhang, D., Wei, J., Wu, T., Jin, X., Fan, X., Cribb, M., Fischer, M. L., Kulmala, M., and Petaja, T.: The impact of the atmospheric turbulence-development tendency on new particle formation: a common finding on three continents, National Science Review, 8, https://doi.org/10.1093/nsr/nwaa157, 2021.

Xu, J., Yan, F., Xie, Y., Wang, F., Wu, J., and Fu, Q.: Impact of meteorological conditions on a nine-day particulate matter pollution event observed in December 2013, Shanghai, China, Particuology, 20, 69-79,

https://doi.org/10.1016/j.partic.2014.09.001, 2015.

Ye, X., Song, Y., Cai, X., and Zhang, H.: Study on the synoptic flow patterns and boundary layer process of the severe haze events over the North China Plain in January 2013, Atmospheric Environment, 124, 129-145, https://doi.org/10.1016/j.atmosenv.2015.06.011, 2016.

Yin, P., Brauer, M., Cohen, A., Burnett, R. T., Liu, J., Liu, Y., Liang, R., Wang, W., Qi, J., Wang, L., and Zhou, M.: Long-term Fine Particulate Matter Exposure and Nonaccidental and Cause-specific Mortality in a Large National Cohort of Chinese Men, Environmental Health Perspectives, 125, https://doi.org/10.1289/ehp1673, 2017.

Yuan, R., Luo, T., Sun, J., Liu, H., Fu, Y., and Wang, Z.: A new method for estimating aerosol mass flux in the urban surface layer using LAS technology, Atmospheric Measurement Techniques, 9, 1925-1937, https://doi.org/10.5194/amt-9-1925-2016, 2016.

Zaveri, R. A. and Peters, L. K.: A new lumped structure photochemical mechanism for large-scale applications, Journal of Geophysical Research-Atmospheres, 104, 30387-30415, https://doi.org/10.1029/1999jd900876, 1999.

Zaveri, R. A., Easter, R. C., Fast, J. D., and Peters, L. K.: Model for Simulating Aerosol Interactions and Chemistry (MOSAIC), Journal of Geophysical Research-Atmospheres, 113, https://doi.org/10.1029/2007jd008782, 2008.

Zhang, H., Zhang, X., Li, Q., Cai, X., Fan, S., Song, Y., Hu, F., Che, H., Quan, J., Kang, L., and Zhu, T.: Research progress on estimation of atmospheric boundary layer height, Acta Meteorologica Sinica, 78, 522-536, 2020.

Zhang, L., Zhang, H., Li, Q., Cai, X., and Song, Y.: Vertical dispersion mechanism of long-range transported dust in Beijing: Effects of atmospheric turbulence, Atmospheric Research, 269, https://doi.org/10.1016/j.atmosres.2022.106033, 2022.

Zhang, L., Sun, J. Y., Shen, X. J., Zhang, Y. M., Che, H., Ma, Q. L., Zhang, Y. W., Zhang, X. Y., and Ogren, J. A.: Observations of relative humidity effects on aerosol light scattering in the Yangtze River Delta of China, Atmospheric Chemistry and

Physics, 15, 8439-8454, https://doi.org/10.5194/acp-15-8439-2015, 2015a.

Zhang, M., Zhao, C., Yang, Y., Du, Q., Shen, Y., Lin, S., Gu, D., Su, W., and Liu, C.: Modeling sensitivities of BVOCs to different versions of MEGAN emission schemes in WRF-Chem (v3.6) and its impacts over eastern China, Geoscientific Model Development, 14, 6155-6175, https://doi.org/10.5194/gmd-14-6155-2021, 2021.

Zhang, R., Wang, G., Guo, S., Zarnora, M. L., Ying, Q., Lin, Y., Wang, W., Hu, M., and Wang, Y.: Formation of Urban Fine Particulate Matter, Chemical Reviews, 115, 3803-3855, https://doi.org/10.1021/acs.chemrev.5b00067, 2015b.

Zhang, Z., Xu, X., Qiao, L., Gong, D., Kim, S.-J., Wang, Y., and Mao, R.: Numerical simulations of the effects of regional topography on haze pollution in Beijing, Scientific Reports, 8, https://doi.org/10.1038/s41598-018-23880-8, 2018.

Zhao, C., Liu, X., Leung, L. R., and Hagos, S.: Radiative impact of mineral dust on monsoon precipitation variability over West Africa, Atmospheric Chemistry and Physics, 11, 1879-1893, https://doi.org/10.5194/acp-11-1879-2011, 2011.

Zhao, C., Leung, L. R., Easter, R., Hand, J., and Avise, J.: Characterization of speciated aerosol direct radiative forcing over California, Journal of Geophysical Research-Atmospheres, 118, 2372-2388, https://doi.org/10.1029/2012jd018364, 2013a.

Zhao, C., Li, Y., Zhang, F., Sun, Y., and Wang, P.: Growth rates of fine aerosol particles at a site near Beijing in June 2013, Advances in Atmospheric Sciences, 35, 209-217, https://doi.org/10.1007/s00376-017-7069-3, 2018.

Zhao, C., Chen, S., Leung, L. R., Qian, Y., Kok, J. F., Zaveri, R. A., and Huang, J.: Uncertainty in modeling dust mass balance and radiative forcing from size parameterization, Atmospheric Chemistry and Physics, 13, 10733-10753, https://doi.org/10.5194/acp-13-10733-2013, 2013b.

Zhao, C., Hu, Z., Qian, Y., Leung, L. R., Huang, J., Huang, M., Jin, J., Flanner, M. G., Zhang, R., Wang, H., Yan, H., Lu, Z., and Streets, D. G.: Simulating black carbon and dust and their radiative forcing in seasonal snow: a case study over North China with field campaign measurements, Atmospheric Chemistry and Physics, 14, 11475-11491, https://doi.org/10.5194/acp-14-11475-2014, 2014.

Zhao, C., Huang, M., Fast, J. D., Berg, L. K., Qian, Y., Guenther, A., Gu, D., Shrivastava, M., Liu, Y., Walters, S., Pfister, G., Jin, J., Shilling, J. E., and Warneke, C.: Sensitivity of biogenic volatile organic compounds to land surface parameterizations and vegetation distributions in California, Geoscientific Model Development, 9, 1959-1976, https://doi.org/10.5194/gmd-9-1959-2016, 2016.

Zhao, X. J., Zhao, P. S., Xu, J., Meng, W., Pu, W. W., Dong, F., He, D., and Shi, Q. F.: Analysis of a winter regional haze event and its formation mechanism in the North China Plain, Atmospheric Chemistry and Physics, 13, 5685-5696, https://doi.org/10.5194/acp-13-5685-2013, 2013c.

Zhong, J., Zhang, X., Dong, Y., Wang, Y., Liu, C., Wang, J., Zhang, Y., and Che, H.: Feedback effects of boundary-layer meteorological factors on cumulative explosive growth of $PM_{2.5}$ during winter heavy pollution episodes in Beijing from 2013 to 2016, Atmospheric Chemistry and Physics, 18, 247-258, https://doi.org/10.5194/acp-18-247-2018, 2018.

~~**Table 1** WRF-Chem model configuration~~

~~Horizontal resolution~~	~~25 km & 5 km & 1 km~~
~~Domain size~~	~~140 x 105 & 250 x 250 & 150 x 150~~
~~Simulation period~~	~~5 March to 21 March 2019~~
~~Gas-phase chemistry scheme~~	~~SAPRC99 mechanism~~
~~Radiation scheme~~	~~Fast-J~~
~~PBL scheme~~	~~YSU scheme~~
~~Microphysics scheme~~	~~Morrison two-moment scheme~~
~~Land surface scheme~~	~~Noah land-surface scheme~~
~~Cumulus scheme~~	~~Kain-Fritsch (25 km grid only)~~
~~Surface layer scheme~~	~~Revised MM5 Monin-Obukhov scheme~~
~~Longwave radiation scheme~~	~~RRTMG scheme~~
~~Shortwave radiation scheme~~	~~RRTMG scheme~~

Table 1 WRF-Chem model configuration

Horizontal resolution	25 km & 5 km & 1 km
Domain size	140 x 105 & 250 x 250 & 150 x 150
Simulation period	5 March to 21 March 2019
Gas-phase chemistry scheme	SAPRC99 mechanism
Radiation scheme	Fast-J
PBL scheme	YSU scheme
Microphysics scheme	Morrison two-moment scheme
Land surface scheme	Noah land-surface scheme
Cumulus scheme	Kain-Fritsch (25 km grid only)
Surface layer scheme	Revised MM5 Monin-Obukhov scheme
Longwave radiation scheme	RRTMG scheme
Shortwave radiation scheme	RRTMG scheme

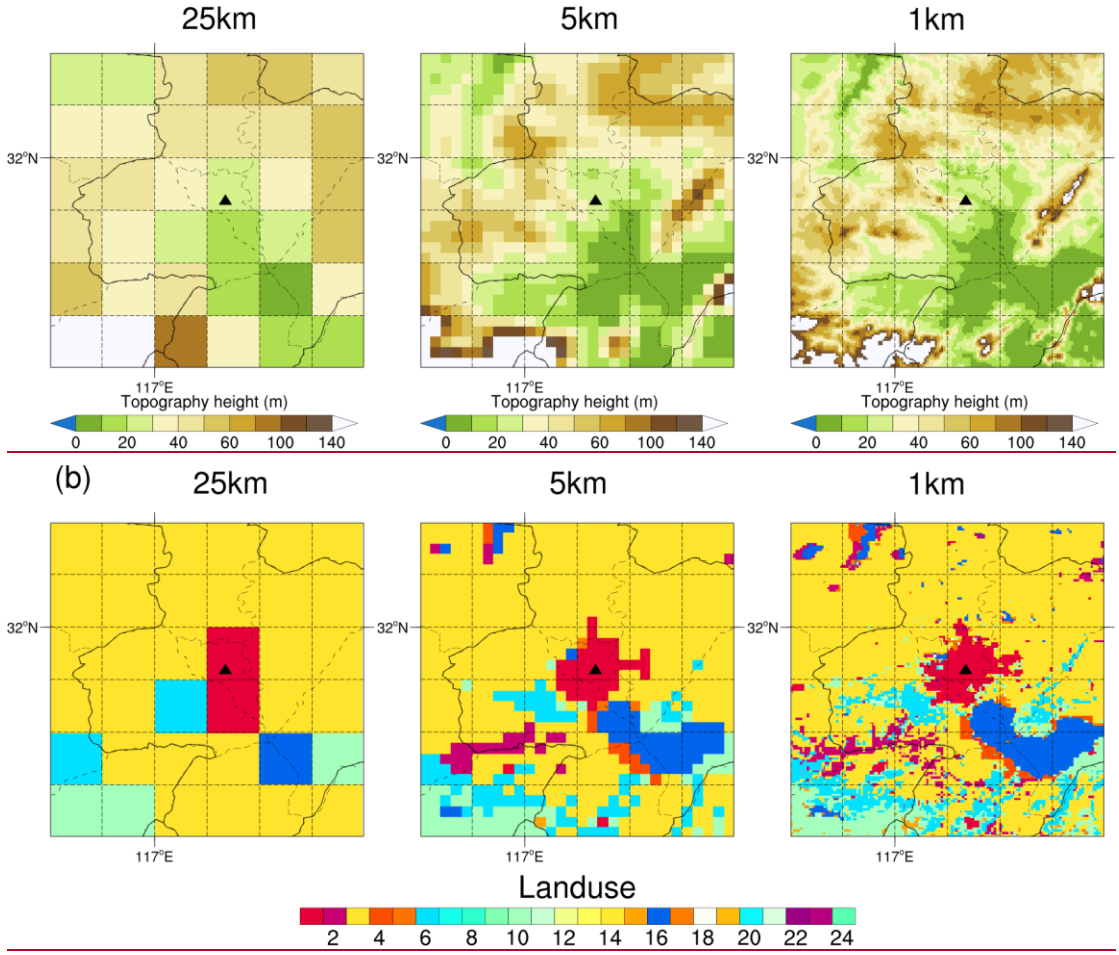

Figure 1. (a) The terrain height (m) in the study area for 25-km (left), 5-km (middle), and 1-km (right) resolution simulations, respectively; (b) Spatial distribution of land use types in the study area for 25-km (left), 5-km (middle), and 1-km (right) resolution simulations, respectively. The solid black triangle indicates the location of the USTC site.

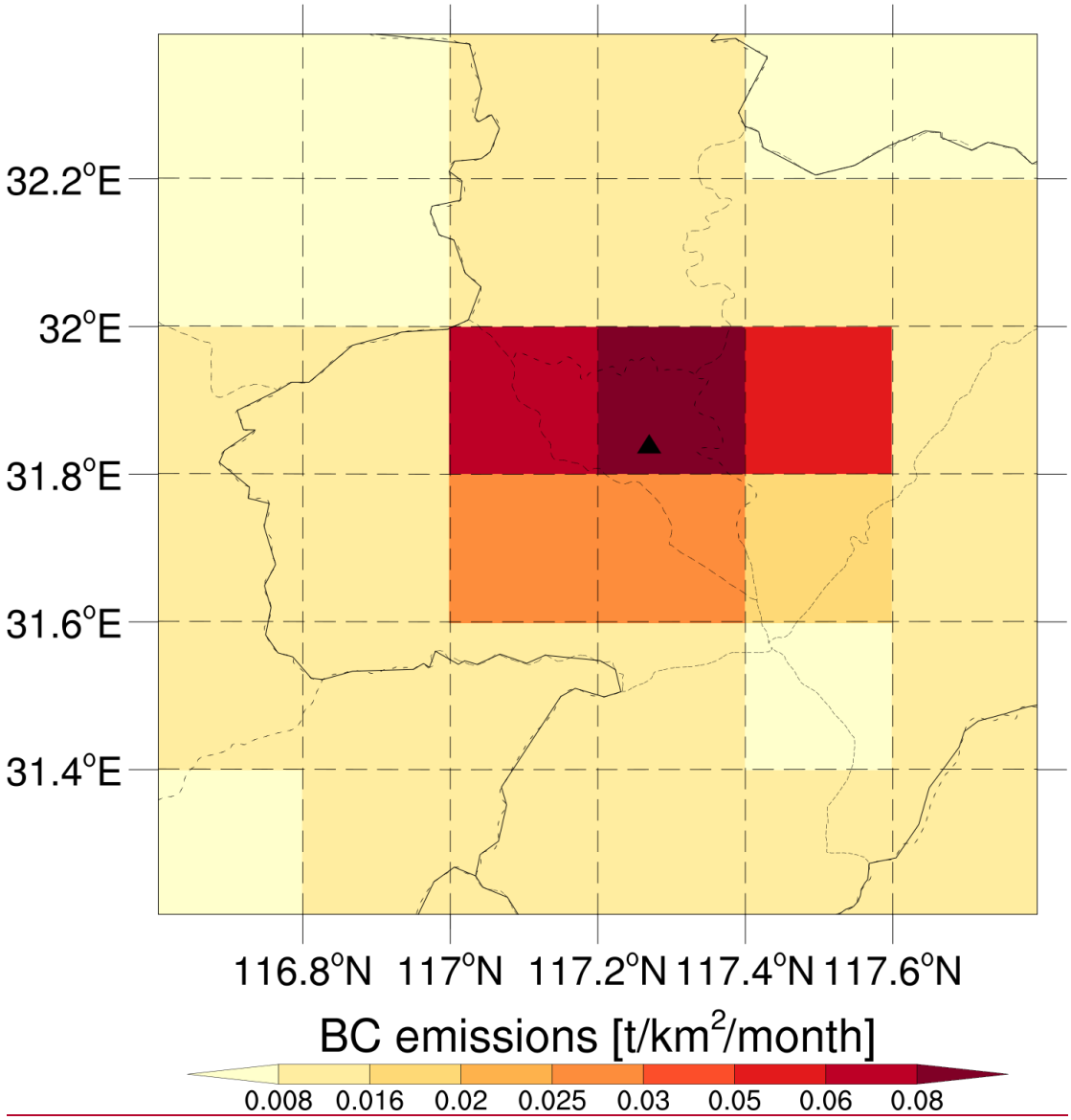

Figure 2. Spatial distribution of BC emissions in the study area. The solid black triangle indicates the location of the USTC site.

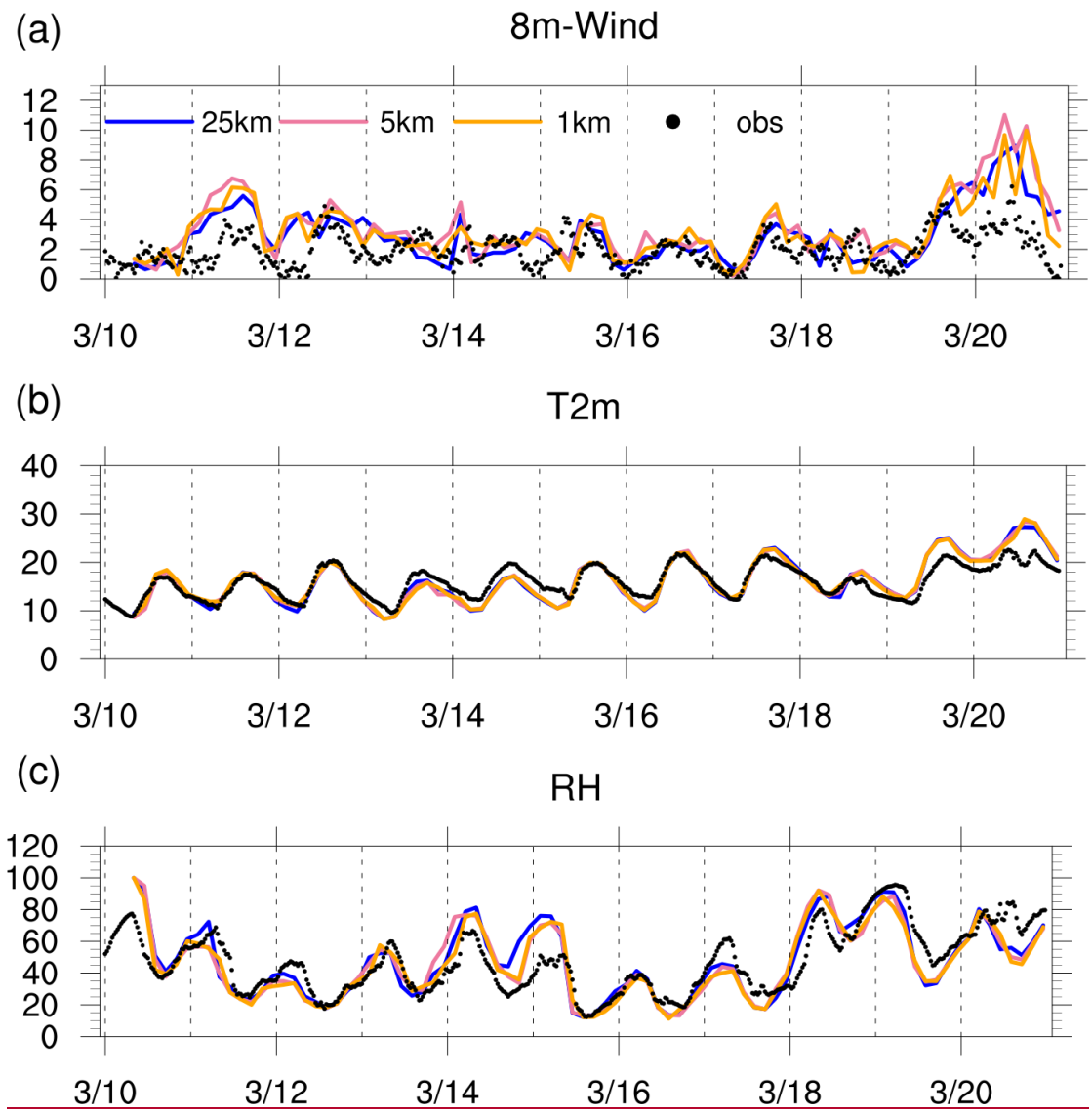

Figure 3. Time series at USTC meteorological tower observation site of observed (black dot) and simulated wind speed at 8 m (top, unit: m s^{-1}), temperature at 2 m (middle, unit: ℃), and relative humidity (bottom, unit: %) for 25-km (solid blue line) resolution, 5-km (solid pink line) resolution, and 1-km (solid orange line) resolution, respectively.

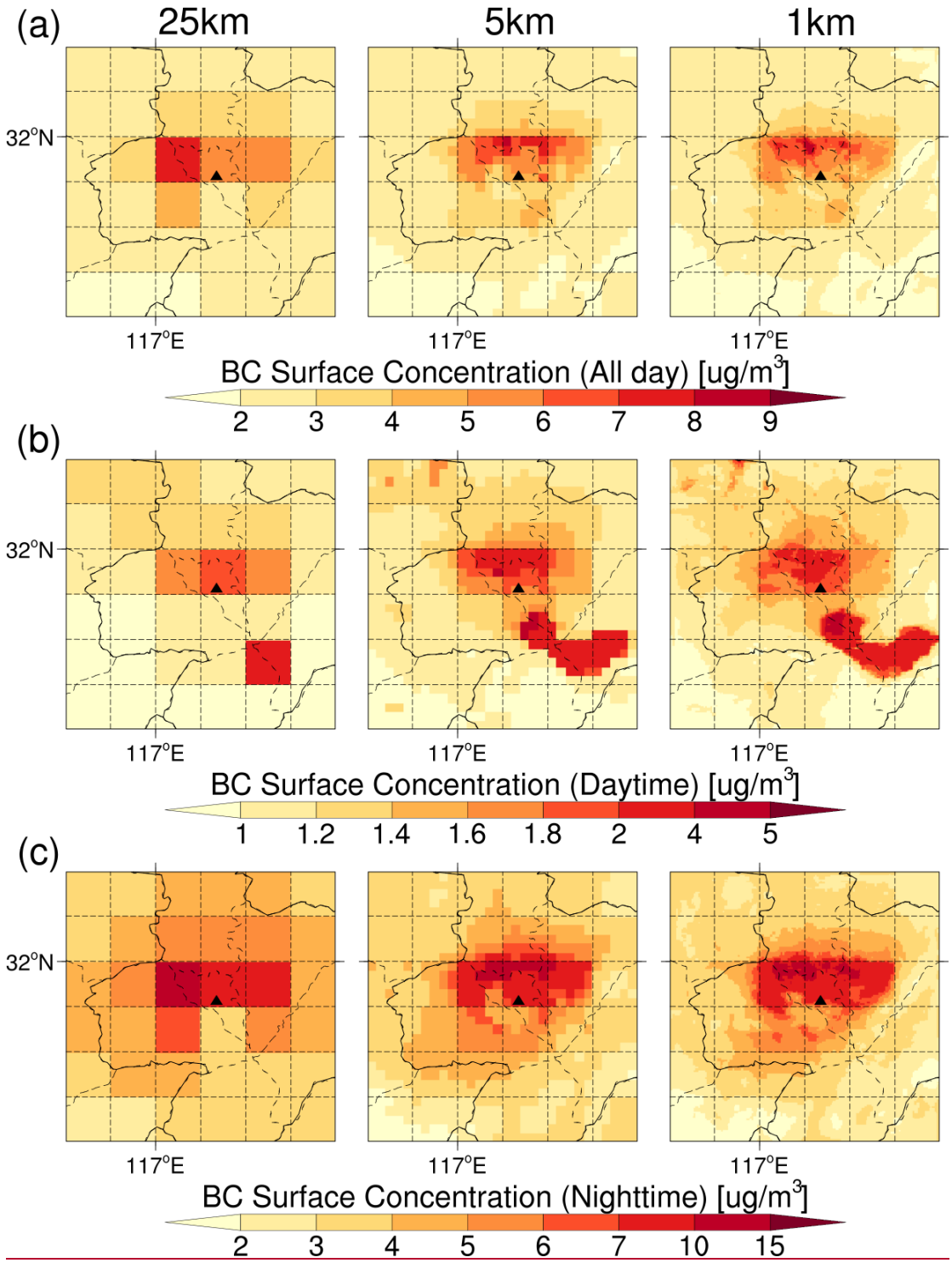

Figure 4. Spatial distribution of the BC surface concentration in the study area for 25-km (left), 5-km (middle), and 1-km (right) resolution simulations of the whole day (top), the daytime (middle), and the nighttime (bottom), respectively. The solid black triangle indicates the location of the USTC site.

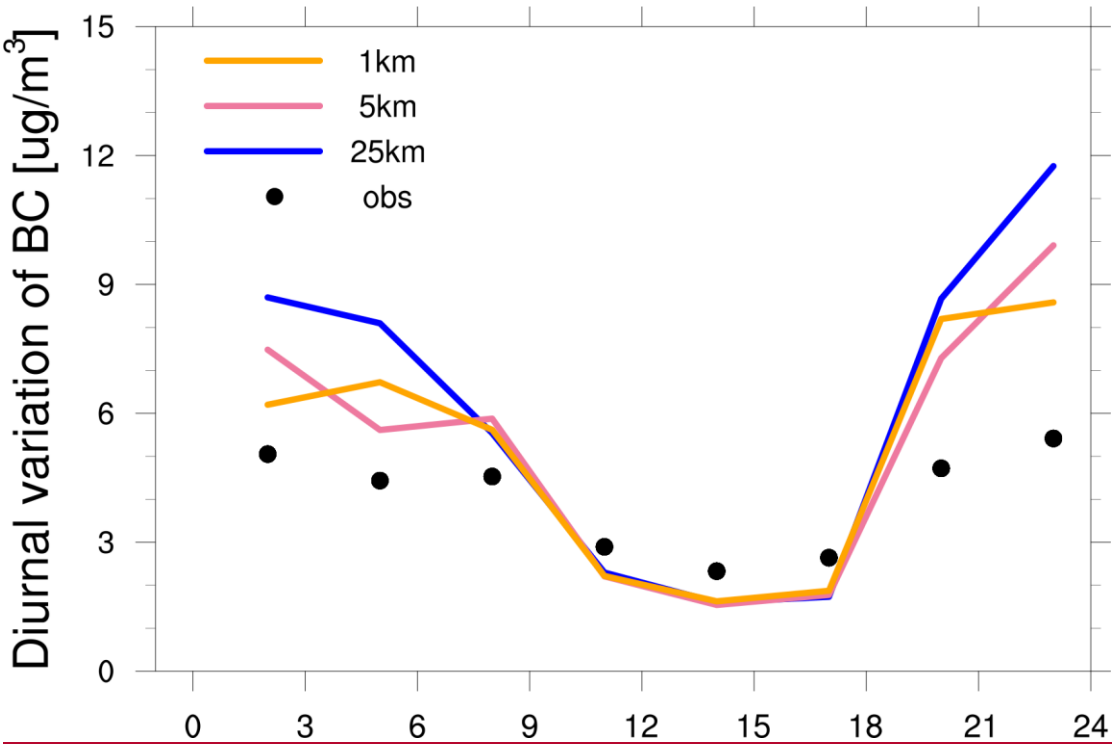

Figure 5. Diurnal variation of BC surface concentrations within 24 h averaged over the USTC site during the study period for 25-km (solid blue line), 5-km (solid pink line), and 1-km (solid orange line) resolution simulations and observations (black dot). Both the simulated results and observations are sampled at the model output frequency, i.e., 3-hourly.

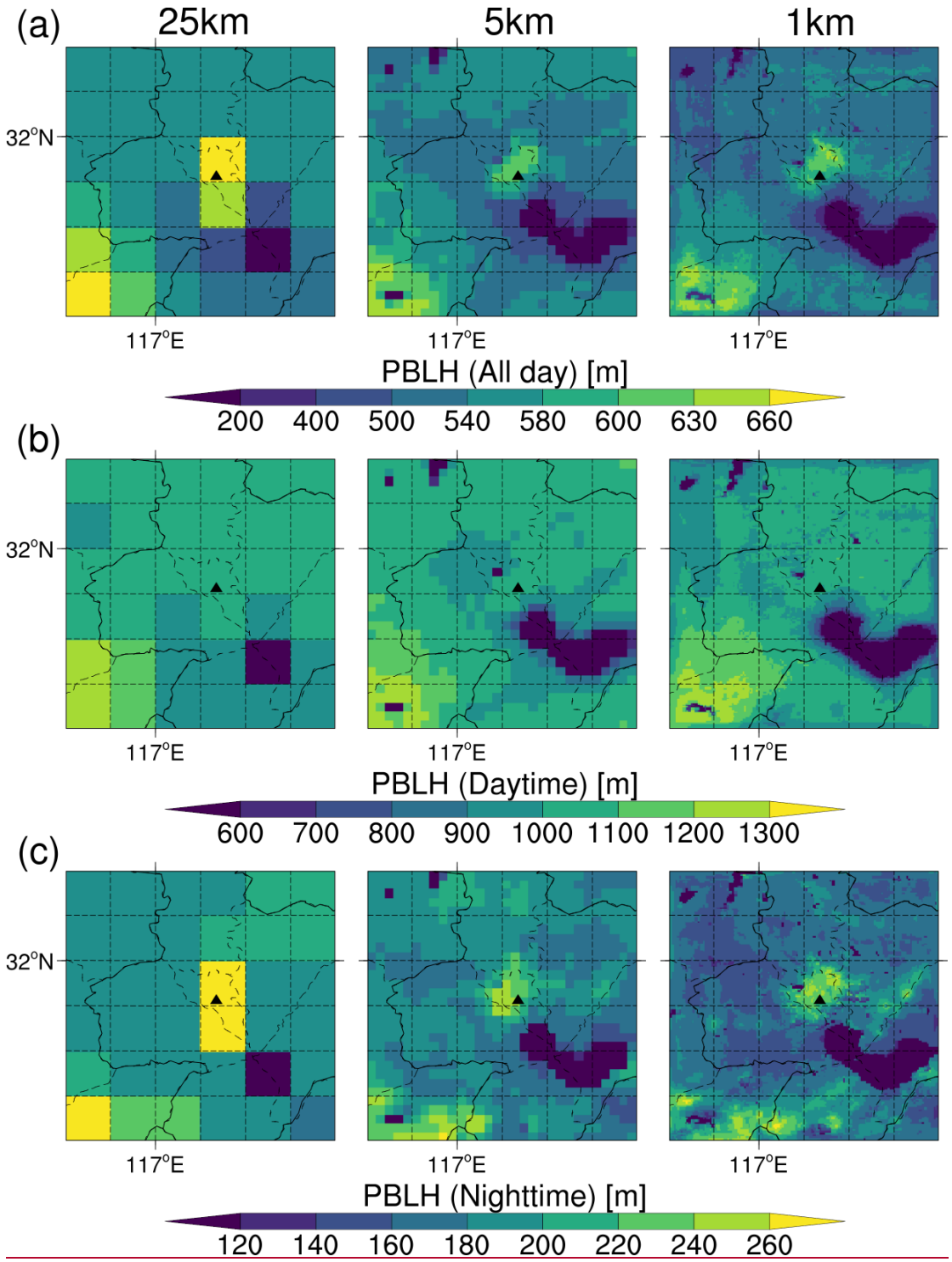

Figure 6. Spatial distribution of the PBL height in the study area for 25-km (left), 5-km (middle), and 1-km (right) resolution simulations of the whole day (top), the daytime (middle), and the nighttime (bottom), respectively. The solid black triangle indicates the location of the USTC site.

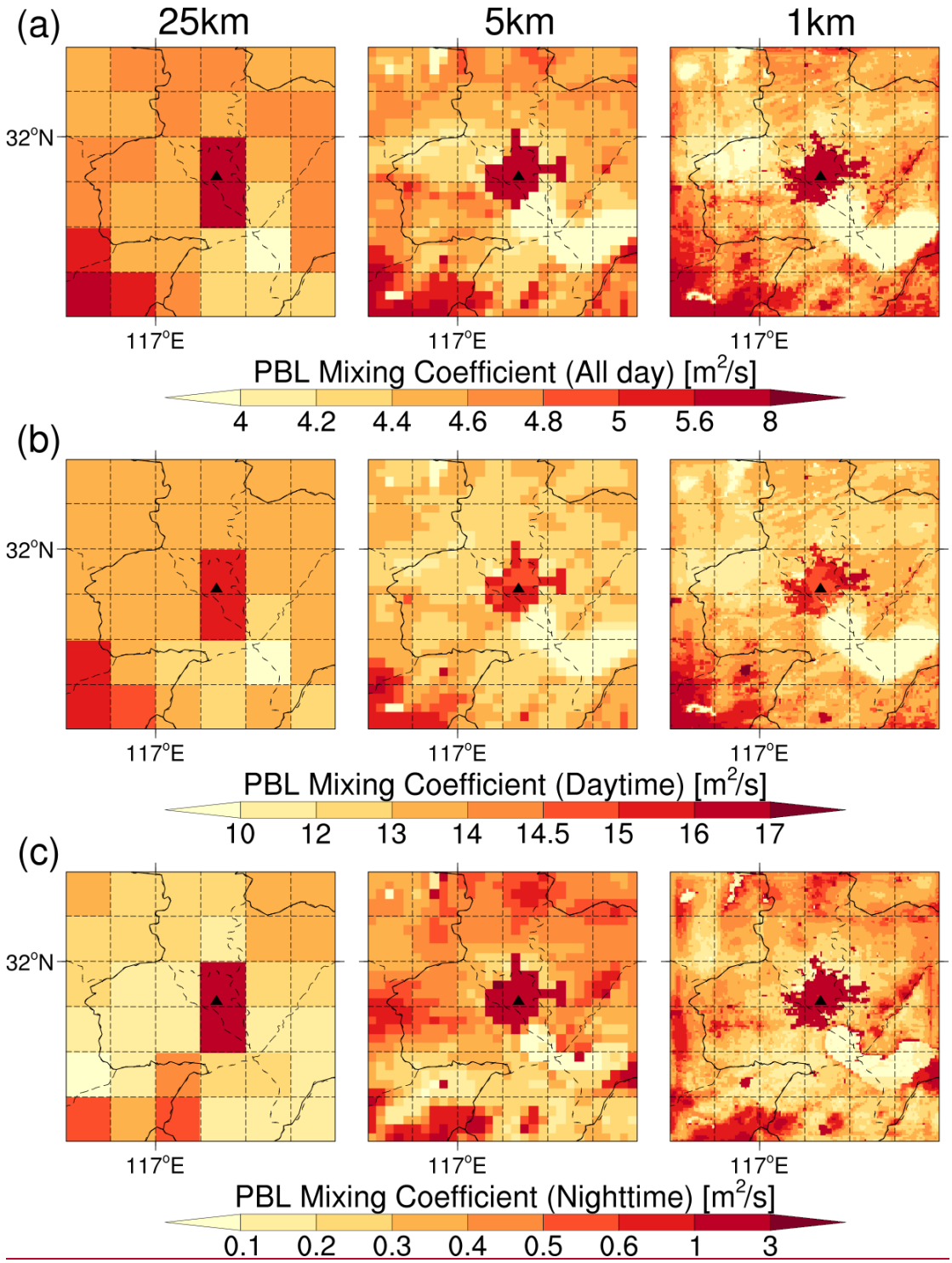

Figure 7. Spatial distribution of PBL mixing coefficients in the study area for 25-km (left), 5-km (middle), and 1-km (right) resolution simulations of the whole day (top), the daytime (middle), and the nighttime (bottom), respectively. The solid black triangle indicates the location of the USTC site.

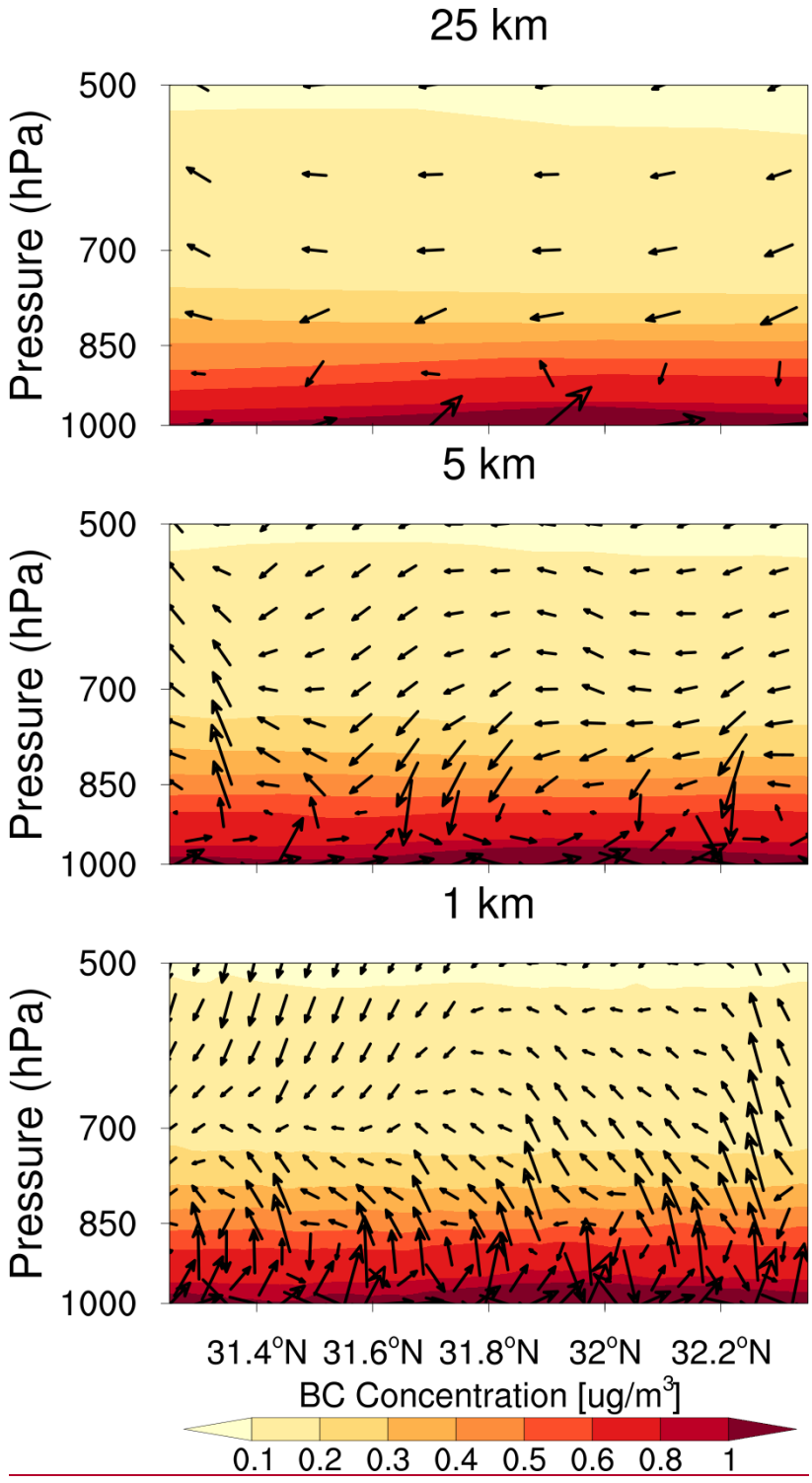

Figure 8. The latitude-pressure cross section of BC concentrations and wind speed flux along the USTC site for 25-km (top), 5-km (middle), and 1-km (bottom) resolution simulations of the whole day, respectively. Vector arrows are the combination of wind speed fluxes v and w, with the vertical wind speed flux being multiplied by 100 for visibility. The shaded contours represent BC concentrations at each pressure level.

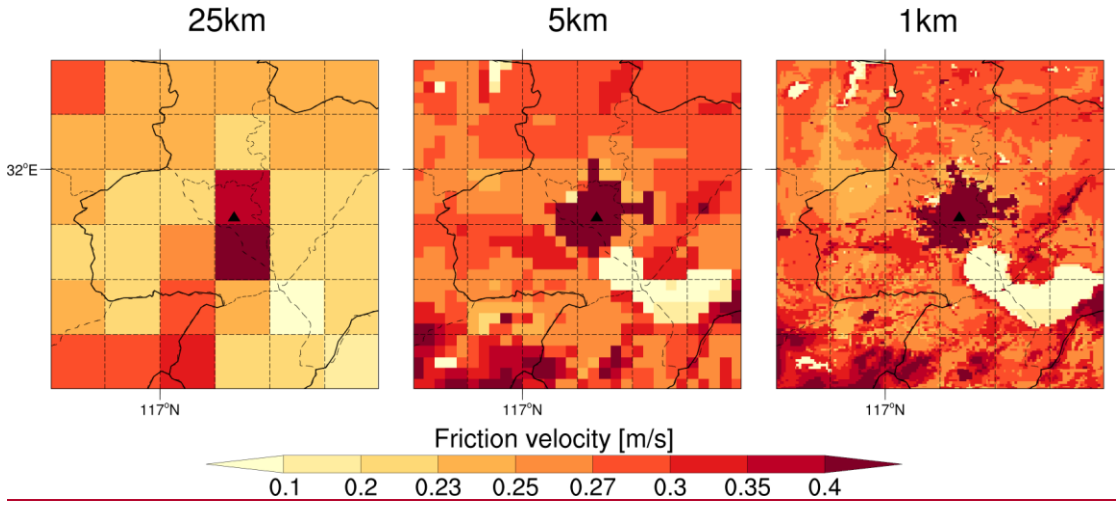

Figure 9. Spatial distribution of friction velocity in the study area for 25-km (left), 5-km (middle), and 1-km (right) resolution simulations of the whole day, respectively. The solid black triangle indicates the location of the USTC site.

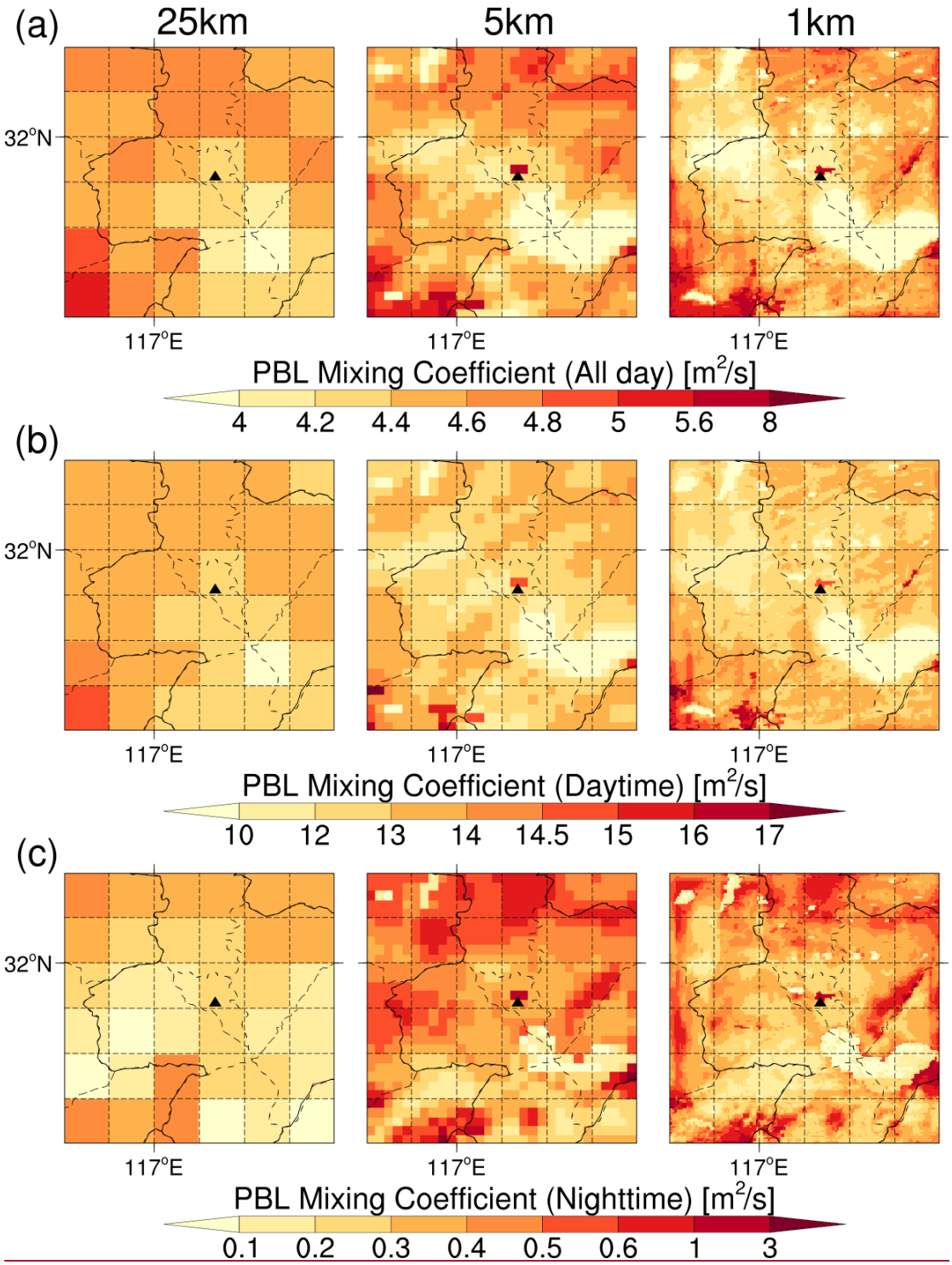

Figure 10. Spatial distribution of PBL mixing coefficients in the study area for 25-km (left), 5-km (middle), and 1-km (right) resolution simulations of the whole day (top), the daytime (middle), and the nighttime (bottom), respectively. The solid black triangle indicates the location of the USTC site. The simulation results are from the three sensitivity experiments.

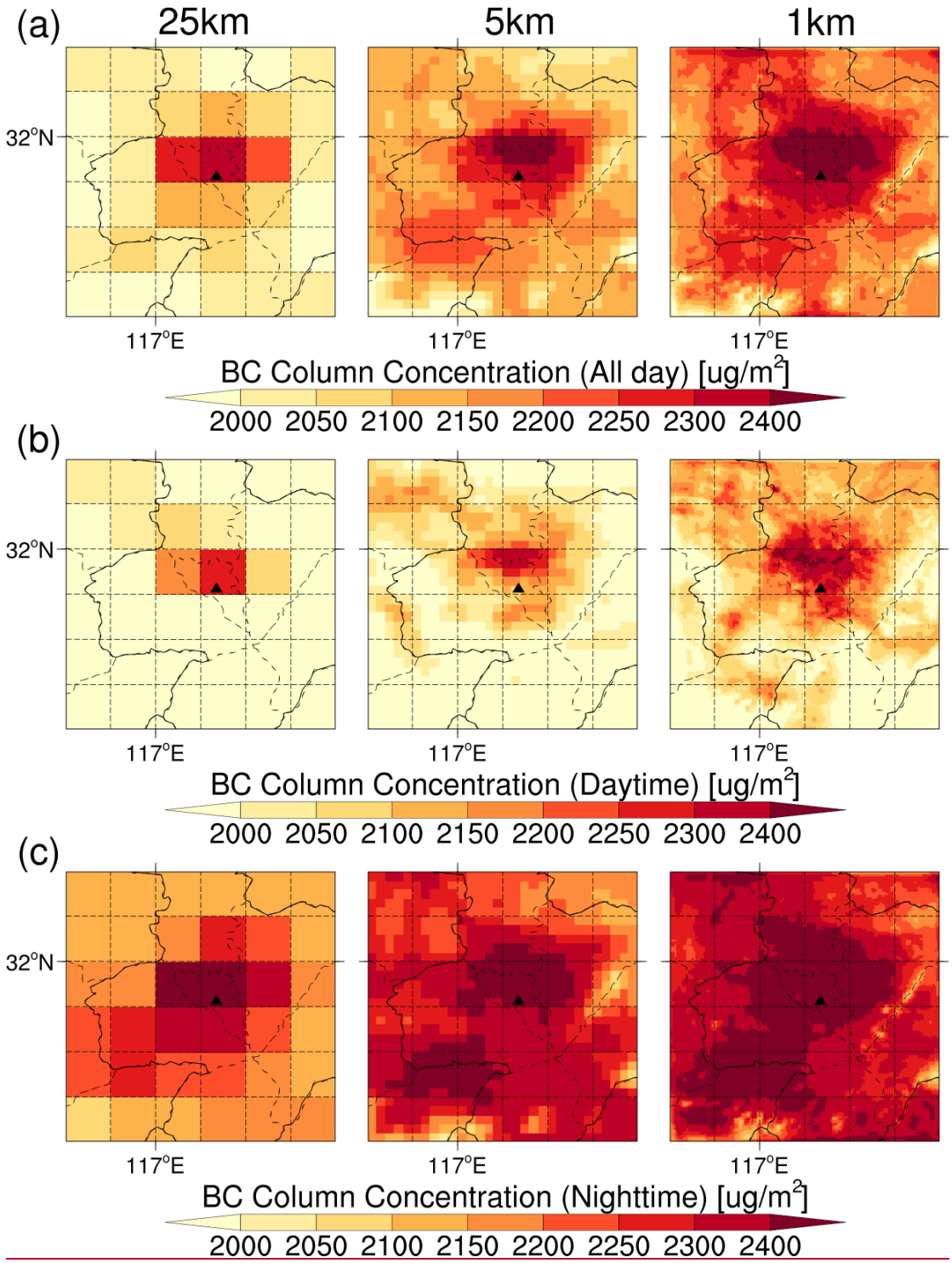

Figure 11. Spatial distribution of the BC column concentration in the study area for 25-km (left), 5-km (middle), and 1-km (right) resolution simulations of the whole day (top), the daytime (middle), and the nighttime (bottom), respectively. The solid black triangle indicates the location of the USTC site.

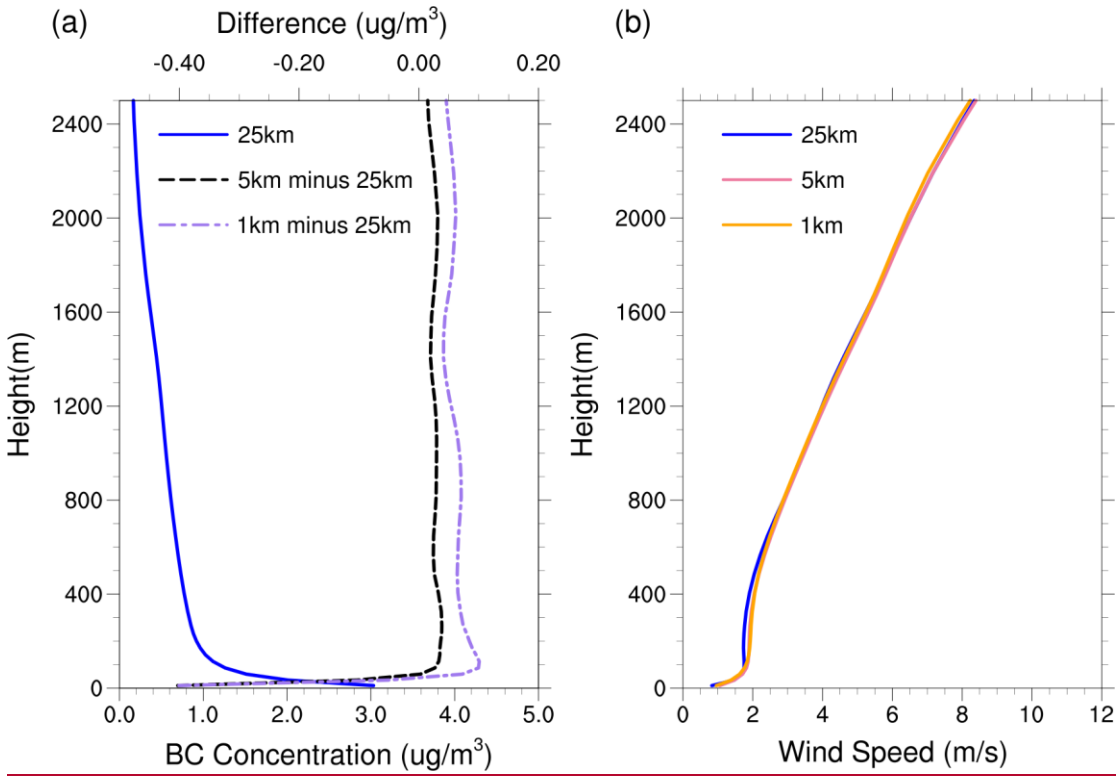

Figure 12. (a) Vertical profiles of BC concentrations simulated at 25-km resolution (solid blue line), the difference between 5-km and 25-km resolutions (dashed black line), and the difference between 1-km and 25-km resolutions (dashed purple line) averaged over the study area for the whole day, respectively. (b) Vertical profiles of wind speed simulated at 25-km resolution (solid blue line), 5-km resolution (solid pink line), and 1-km resolution (solid orange line) averaged over the study area for the whole day, respectively.

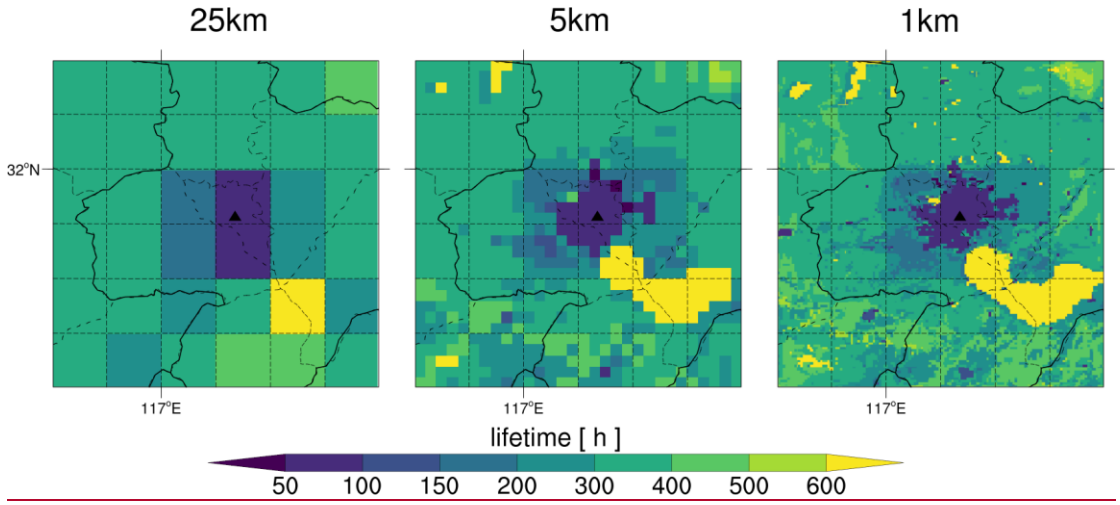

Figure 13. Spatial distribution of the lifetime in the study area for 25-km (left), 5-km (middle), and 1-km (right) resolution simulations of the whole day, respectively. The solid black triangle indicates the location of the USTC site.

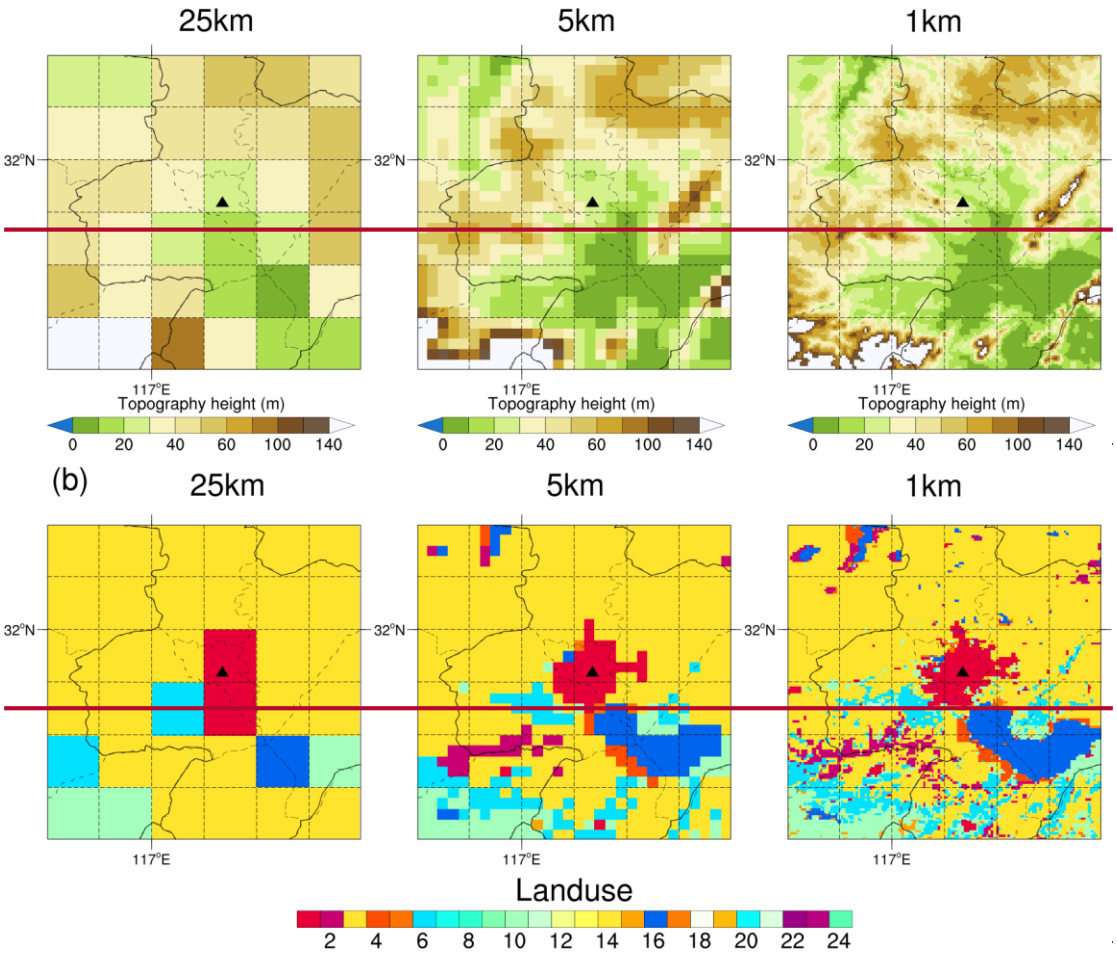

Figure 1. (a) The terrain height (m) in the study area for 25-km (left), 5-km (middle), and 1-km (right) resolution simulations, respectively; (b) Spatial distribution of land use types in the study area for 25-km (left), 5-km (middle), and 1-km (right) resolution simulations, respectively. The solid black triangle indicates the location of the USTC site.

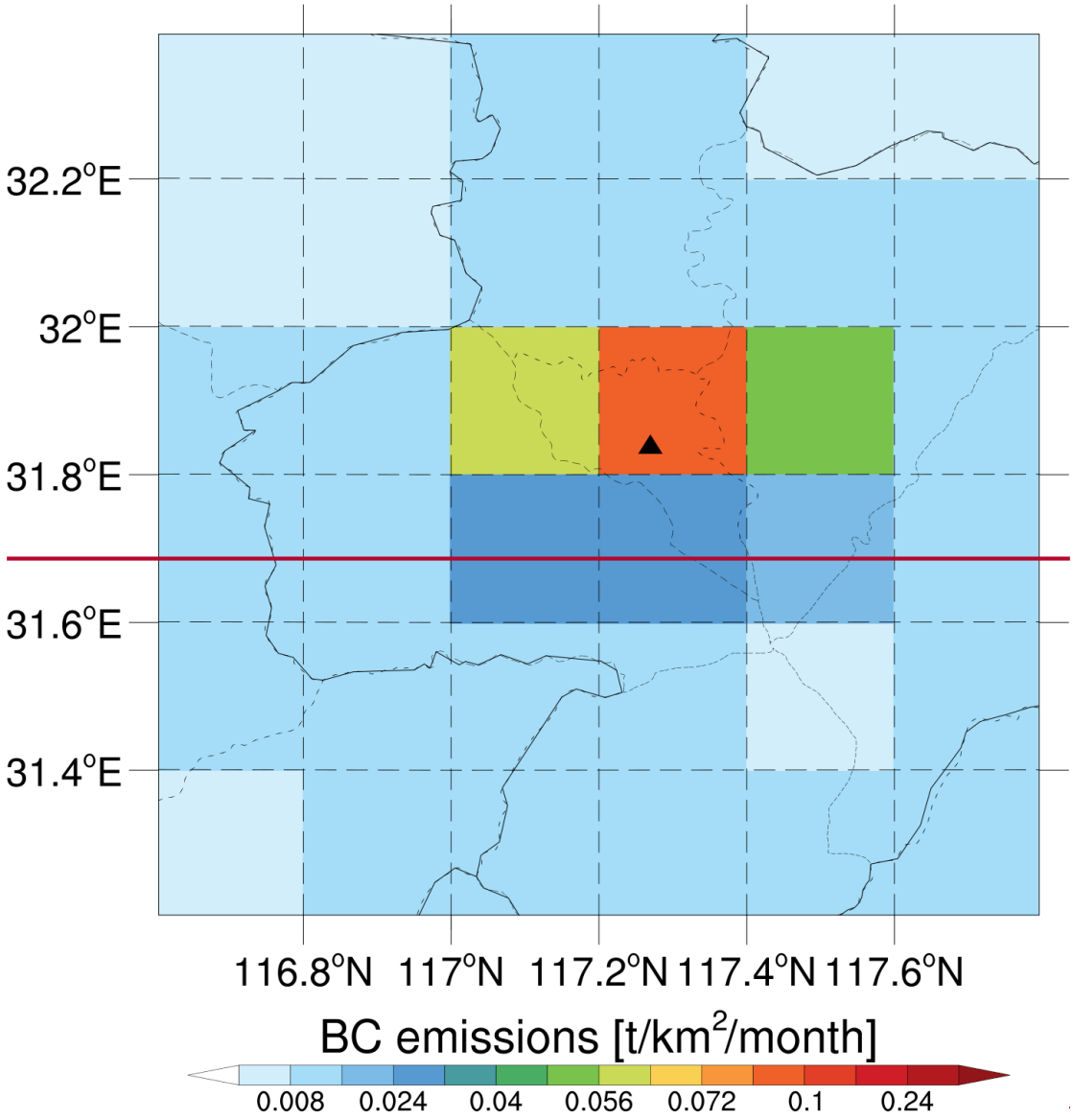

Figure 2. Spatial distribution of BC emissions in the study area. The solid black triangle indicates the location of the USTC site.

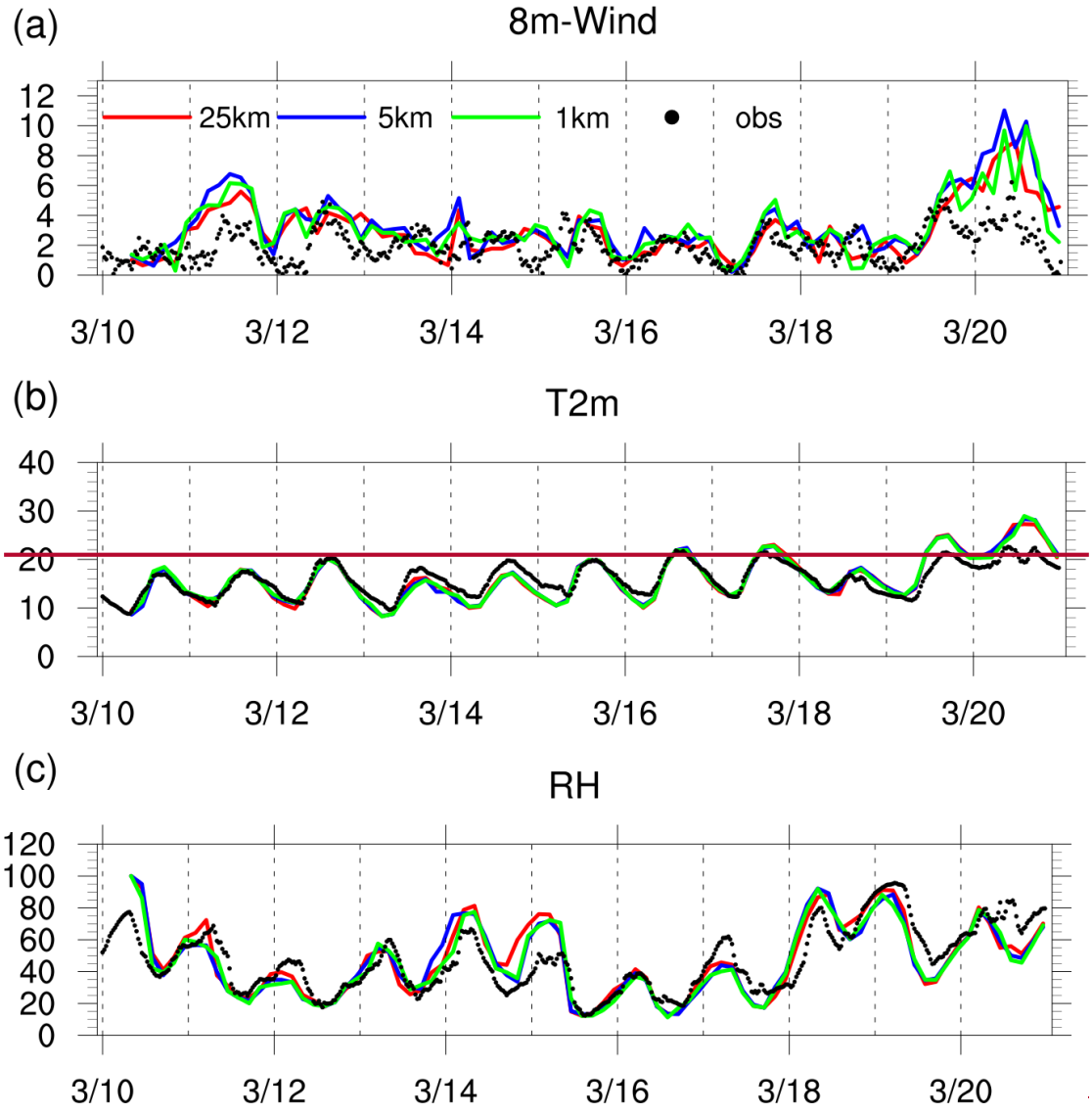

Figure 3. Time series at USTC meteorological tower observation site of observed (black dot) and simulated wind speed at 8 m (top, unit: m s^{-1}), temperature at 2 m (middle, unit: °C), and relative humidity (bottom, unit: %) for 25-km (solid red line) resolution, 5-km (solid blue line) resolution, and 1-km (solid green line) resolution, respectively.

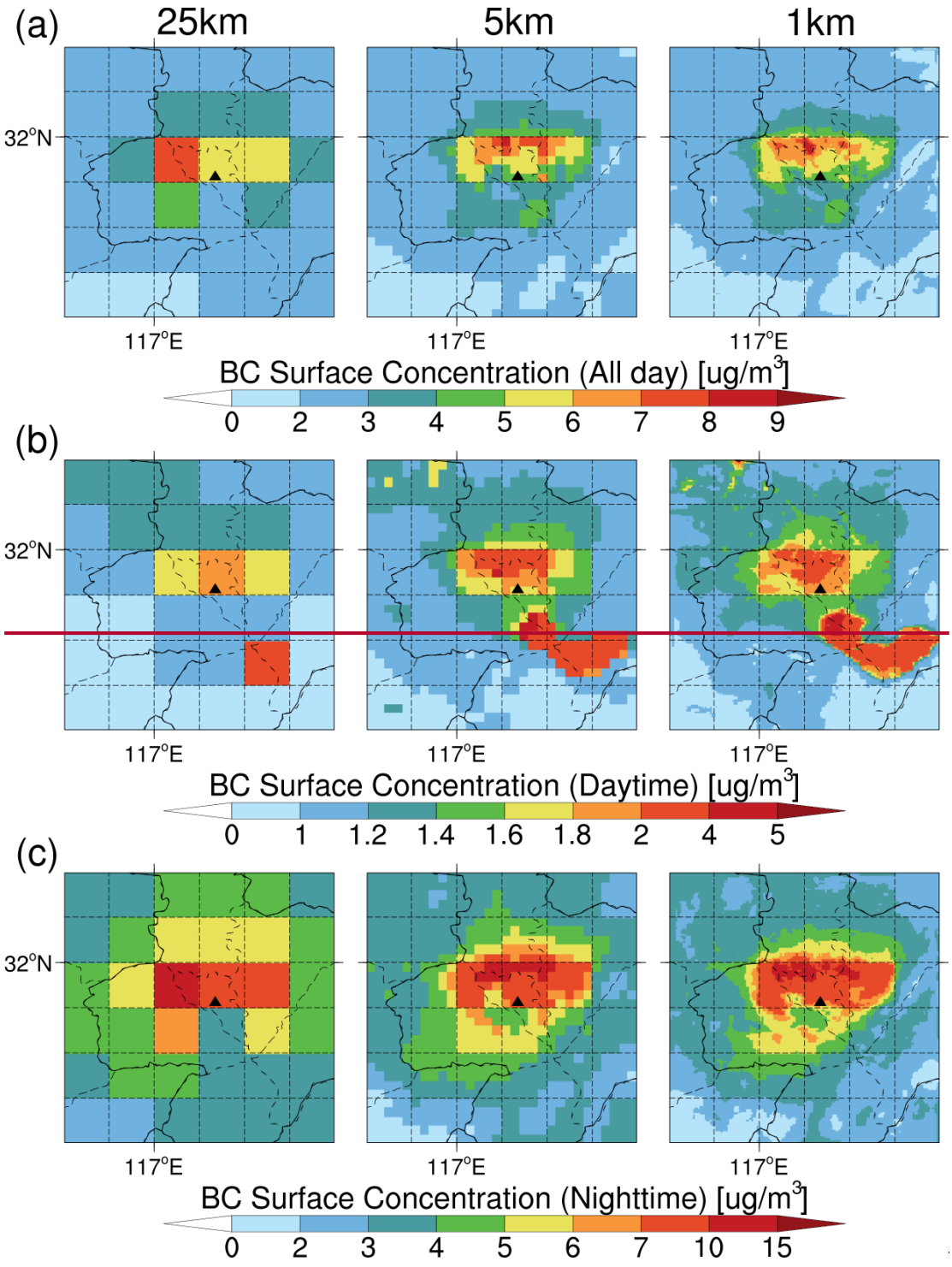

Figure 4. Spatial distribution of the BC surface concentration in the study area for 25-km (left), 5-km (middle), and 1-km (right) resolution simulations of the whole day

(top), the daytime (middle), and the nighttime (bottom), respectively. The solid black triangle indicates the location of the USTC site.

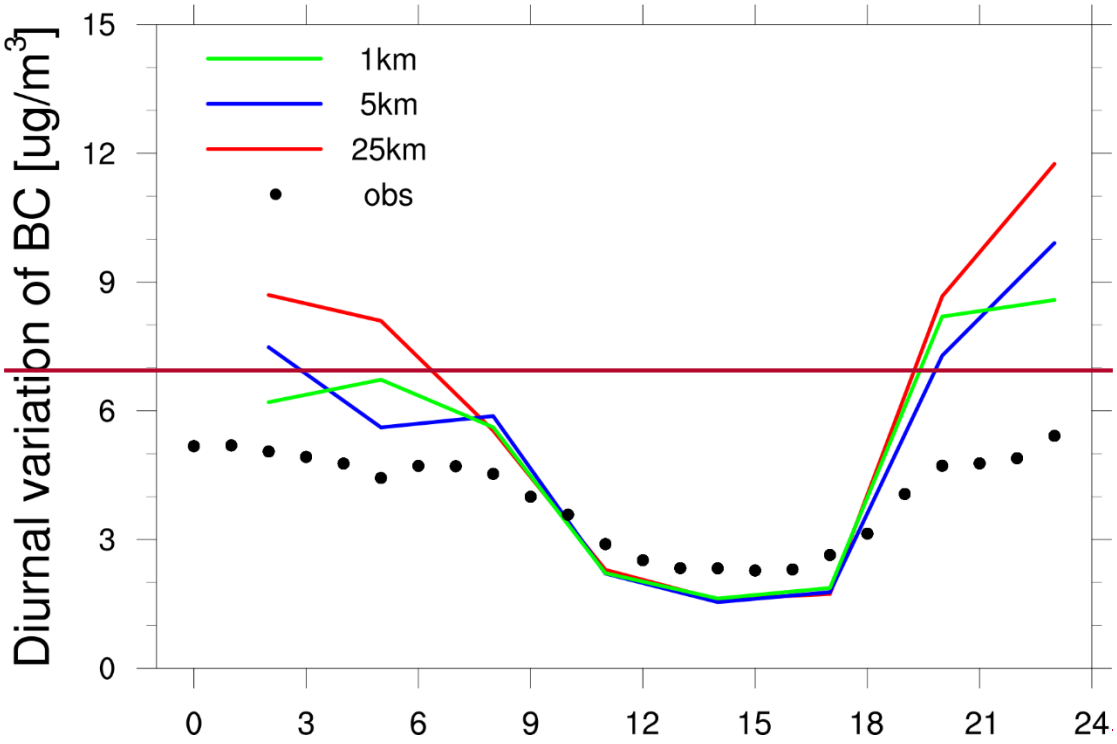

Figure 5. Diurnal variation of BC surface concentrations within 24 h averaged over the Hefei region (within the range of Figure 1a) during the study period for 25-km (solid red line), 5-km (solid blue line), and 1-km (solid green line) resolution simulations and observations (black dot). Both the simulated results and observations are sampled at the model output frequency, i.e., 3-hourly.

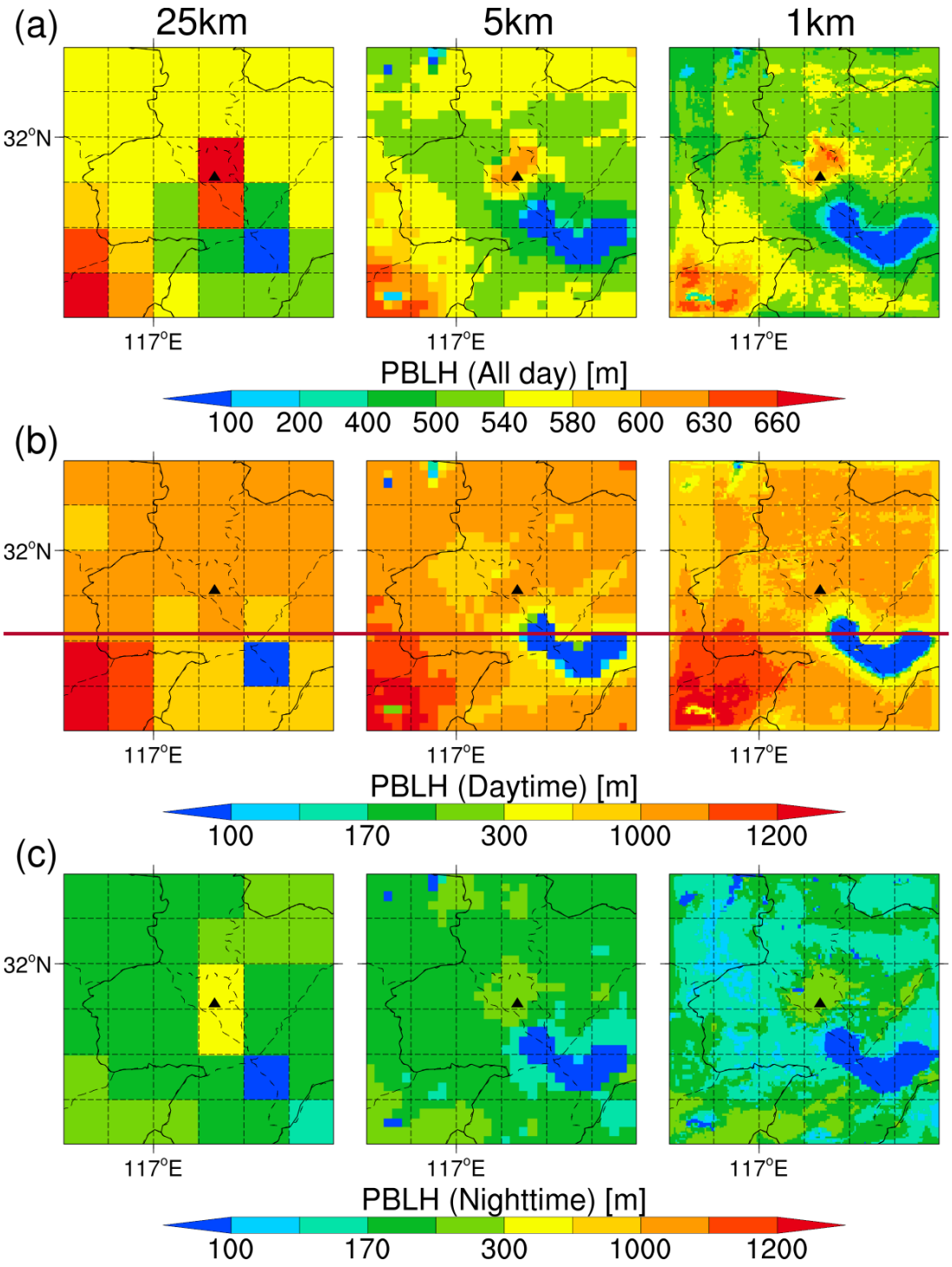

Figure 6. Spatial distribution of the PBL height in the study area for 25-km (left), 5-km (middle), and 1-km (right) resolution simulations of the whole day (top), the

daytime (middle), and the nighttime (bottom), respectively. The solid black triangle indicates the location of the USTC site.

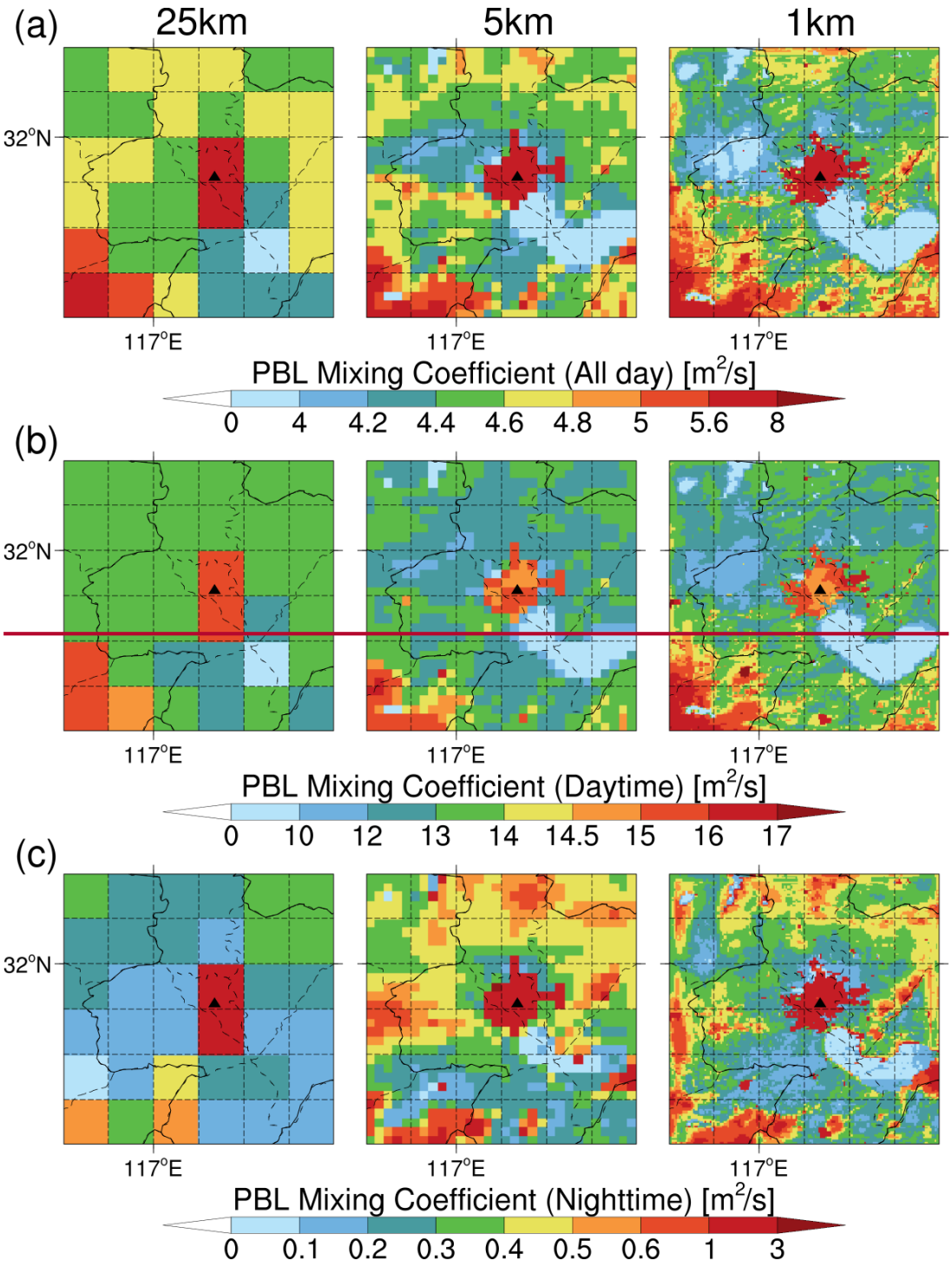

Figure 7. Spatial distribution of PBL mixing coefficients in the study area for 25-km (left), 5-km (middle), and 1-km (right) resolution simulations of the whole day (top),

the daytime (middle), and the nighttime (bottom), respectively. The solid black triangle indicates the location of the USTC site.

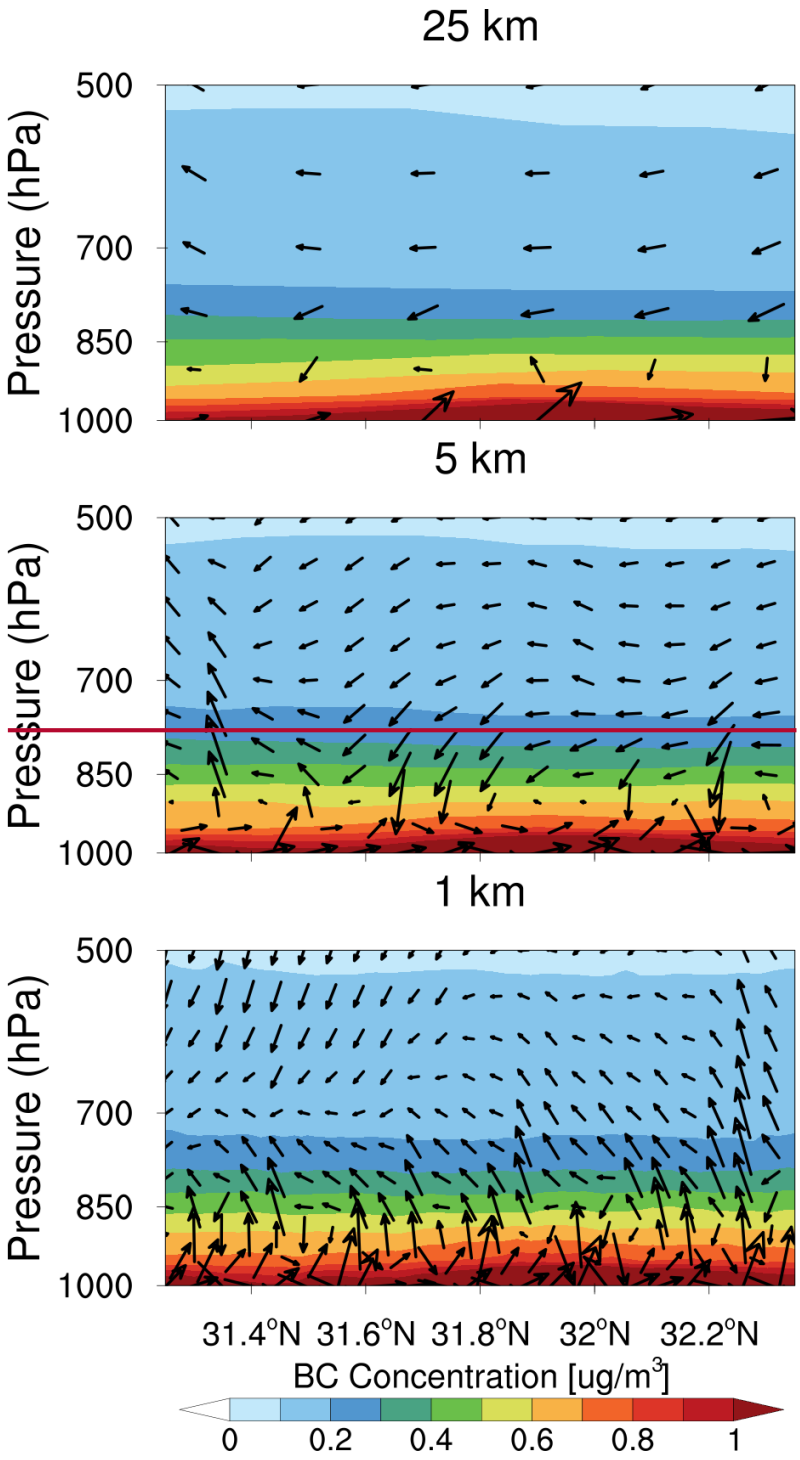

Figure 8. The latitude-pressure cross section of BC concentrations and wind speed flux along the USTC site for 25-km (top), 5-km (middle), and 1-km (bottom)

resolution simulations of the whole day, respectively. Vector arrows are the combination of wind speed fluxes v and w, with the vertical wind speed flux being multiplied by 100 for visibility. The shaded contours represent BC concentrations at each pressure level.

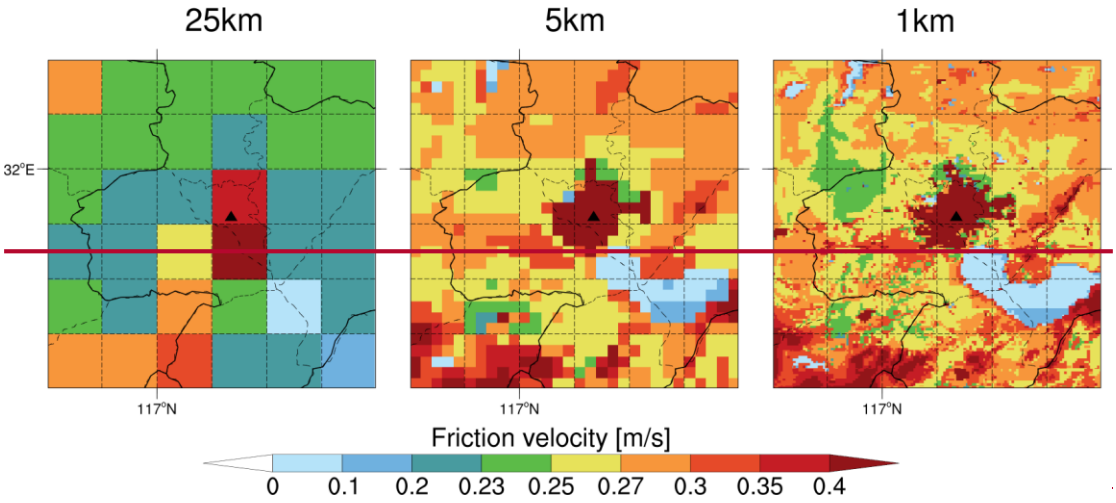

Figure 9. Spatial distribution of friction velocity in the study area for 25-km (left), 5-km (middle), and 1-km (right) resolution simulations of the whole day, respectively. The solid black triangle indicates the location of the USTC site.

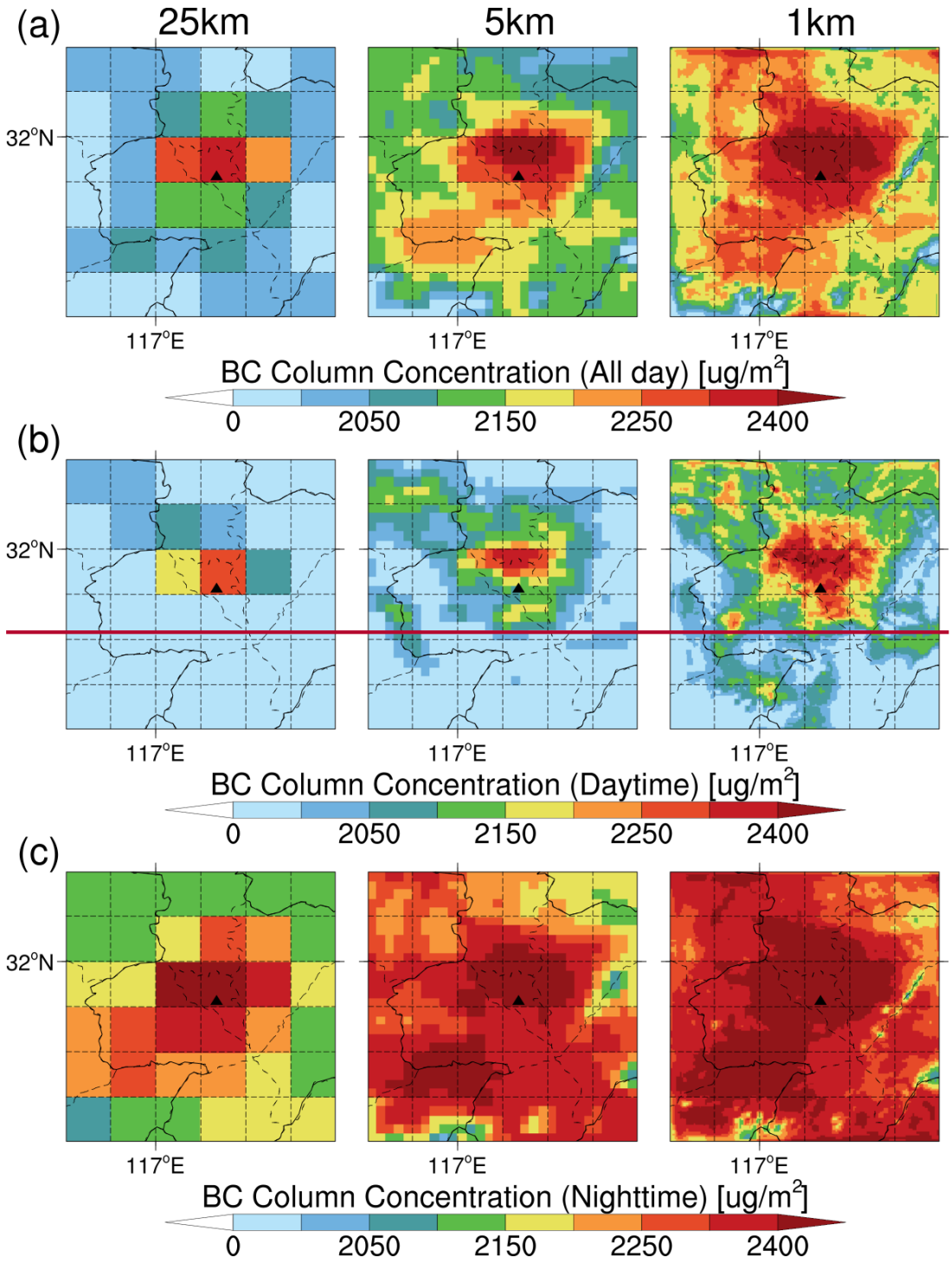

Figure 10. Spatial distribution of the BC column concentration in the study area for 25-km (left), 5-km (middle), and 1-km (right) resolution simulations of the whole day

~~(top), the daytime (middle), and the nighttime (bottom), respectively. The solid black triangle indicates the location of the USTC site.~~

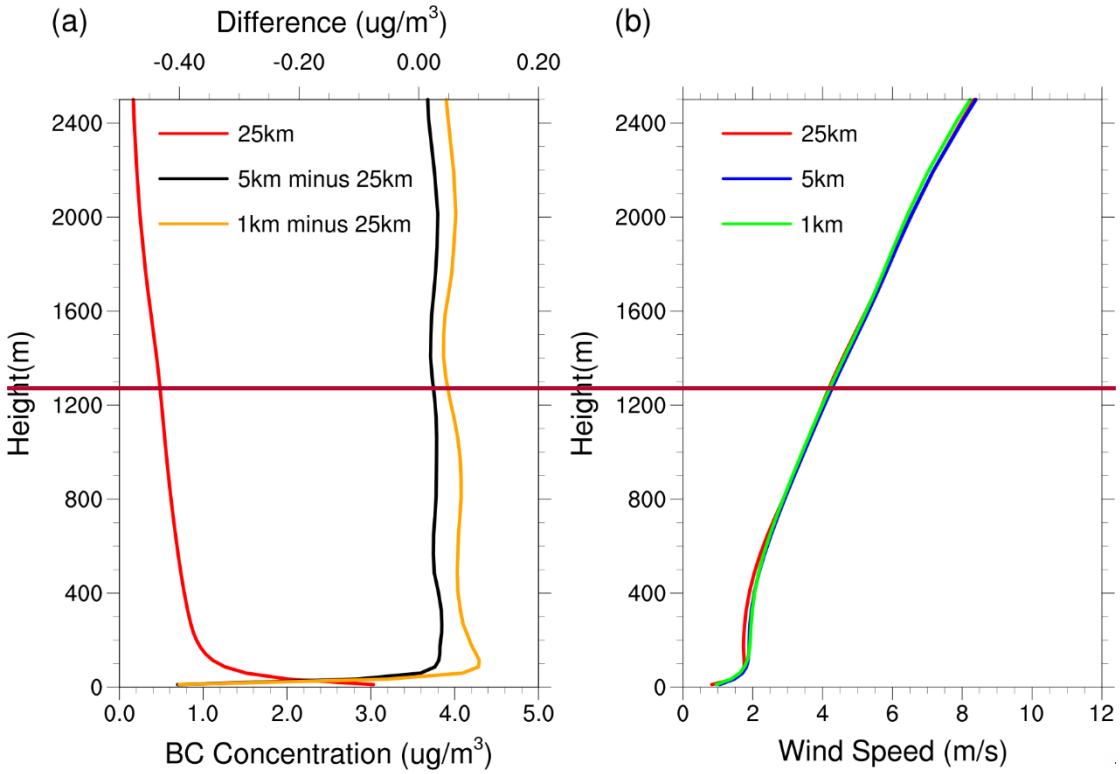

~~Figure 11.~~ ~~(a) Vertical profiles of BC concentrations simulated at 25-km resolution (solid red line), the difference between 5-km and 25-km resolutions (solid black line), and the difference between 1-km and 25-km resolutions (solid orange line) averaged over the study area for the whole day, respectively. (b) Vertical profiles of wind speed simulated at 25-km resolution (solid red line), 5-km resolution (solid blue line), and 1-km resolution (solid green line) averaged over the study area for the whole day, respectively.~~

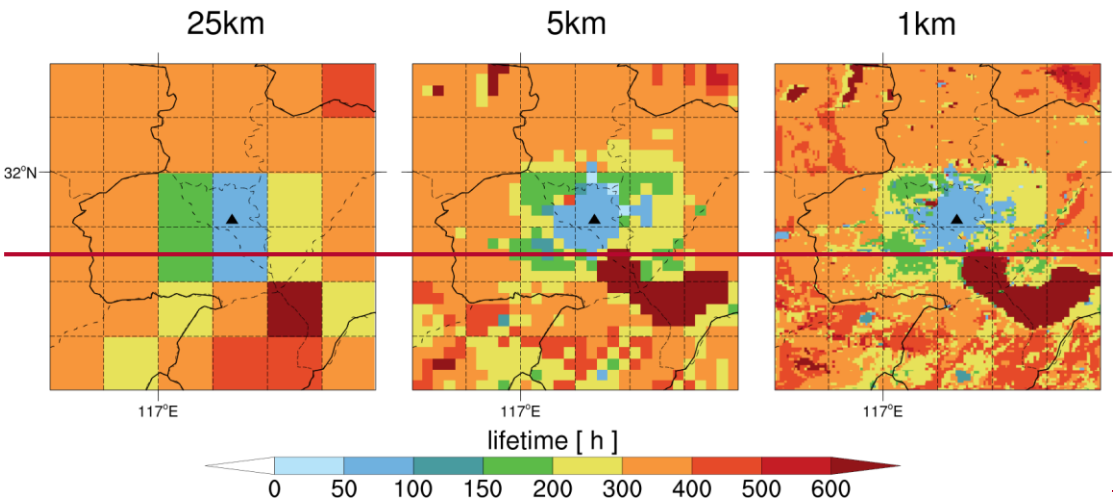

Figure 12. Spatial distribution of the lifetime in the study area for 25-km (left), 5-km (middle), and 1-km (right) resolution simulations of the whole day, respectively. The solid black triangle indicates the location of the USTC site.

Supporting information for:

Modeling urban pollutant transport at multi-resolutions: Impacts of turbulent mixing

Zining Yang[1], Qiuyan Du[1], Qike Yang[1], Chun Zhao[1,2,3*], Gudongze Li[1], Zihan Xia[1], Mingyue Xu[1], Renmin Yuan[1], Yubin Li[4], Kaihui Xia[1], Jun Gu[1], and Jiawang Feng[1]

[1]Deep Space Exploration Laboratory/School of Earth and Space Sciences/CMA-USTC Laboratory of Fengyun Remote Sensing/State Key Laboratory of Fire Science/Institute of Advanced Interdisciplinary Research on High-Performance Computing Systems and Software, University of Science and Technology of China, Hefei, China

[2]Laoshan Laboratory, Qingdao, China

[3]CAS Center for Excellence in Comparative Planetology, University of Science and Technology of China, Hefei, China.

[4]School of Atmospheric Physics, Nanjing University of Information Science and Technology, Nanjing, China

*Corresponding author: Chun Zhao (chunzhao@ustc.edu.cn)

Contents of this file

Figure S13: The spatial distributions of PBL mixing coefficient differences between the two higher-resolutions.

Figure S14: The latitude-pressure cross section of BC concentrations and wind flux across multi-resolutions along the USTC site.

Figure S15: The spatial distributions of friction velocity differences between high- and low-resolutions.

Figure S16: The spatial distributions of PBL mixing coefficient differences between high- and low-resolutions simulation results from the sensitivity experiments.

Figure S17: The spatial distributions of PBL mixing coefficient differences between the two higher-resolutions simulation results from the sensitivity experiments.

Figure S18: The latitude-pressure cross section of BC concentrations and wind flux across multi-resolutions from the sensitivity experiments along the USTC site.

Figure S19: The spatial distributions of BC column concentration differences between high- and low-resolutions.

Figure S20: The spatial distributions of BC column concentration differences between the two higher-resolutions.

Text S1. The process of grid refinement in this study.

Due to the disparate grid sizes of the three resolution simulations impeding direct calculation of spatial distribution differences, we employ a grid refinement method to upscale the low-resolution grids to match the high-resolution grid cells. The grid refinement process involves dividing the cells in the original coarse grid into finer cells. Specifically, the 25 km grids are divided into 25 x 25 small grids and the 5 km grids are divided into 5 x 5 small grids. This approach ensures that the grid resolution of all three simulations is identical while preserving spatial details, thus allowing us to quantify the differences between the 25 km resolution simulations and the two higher-resolution simulations.

Table S1. Description of land cover data classifications

Number	Description
1	Urban
2	Dryland cropland/pasture
3	Irrigated cropland/pasture
4	Mixed Dryland/Irrigated Cropland
5	Cropland/Grassland Mosaic
6	Cropland/Woodland Mosaic
7	Grassland
8	Shrubland
9	Mixed Shrubland/Grassland
10	Savanna
11	Deciduous Broadleaf Forest
12	Deciduous Needleleaf Forest
13	Evergreen Broadleaf Forest
14	Evergreen Needleleaf Forest
15	Mixed Forest
16	Water
17	Herbaceous Wetland
18	Wooded Wetland
19	Barren or Sparsely Vegetated
20	Herbaceous Tundra
21	Wooded Tundra
22	Mixed Tundra
23	Bare Ground Tundra
24	Snow or Ice

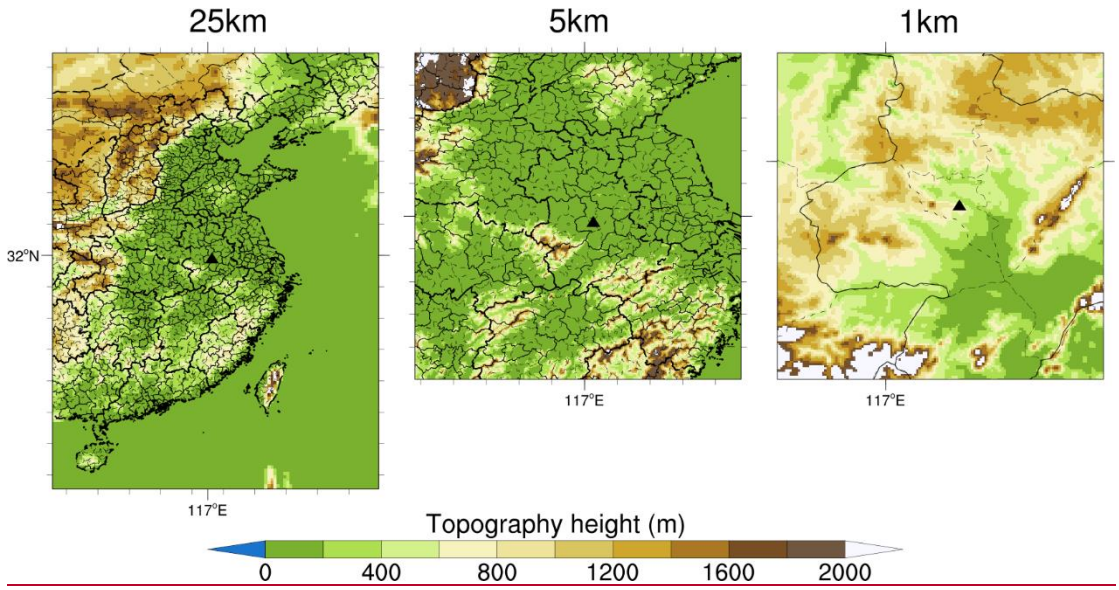

Figure S1. The three domains in the WRF-Chem simulations and the terrain height (m) of each domain. Domain one (D1) has a horizontal grid spacing of 25 km, domain 2 (D2) 5 km, and domain 3 (D3) 1 km. The solid black triangle indicates the location of the USTC site.

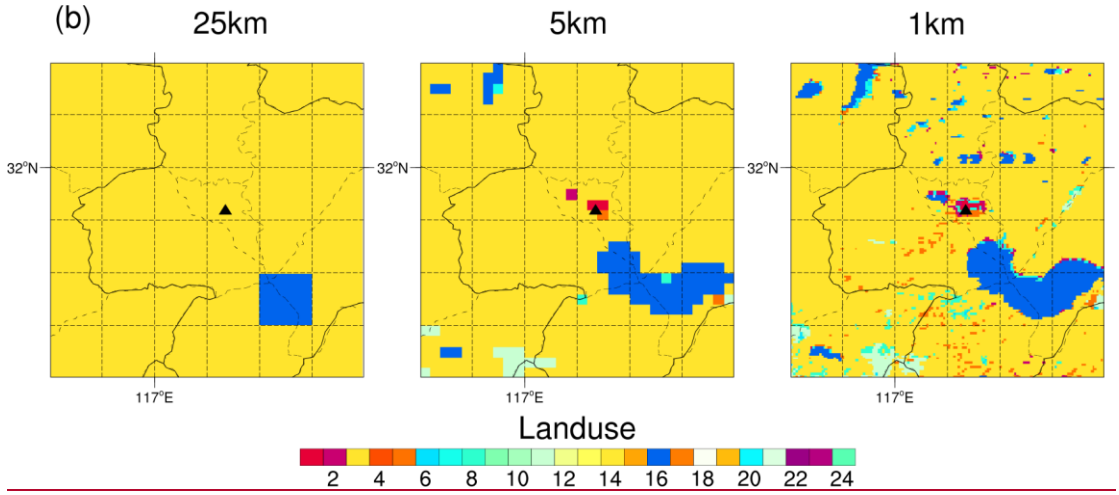

Figure S2. The spatial distribution of the default USGS land use category data in WRF in the study area for 25-km (left), 5-km (middle), and 1-km (right) resolution simulations, respectively. The solid black triangle indicates the location of the USTC site.

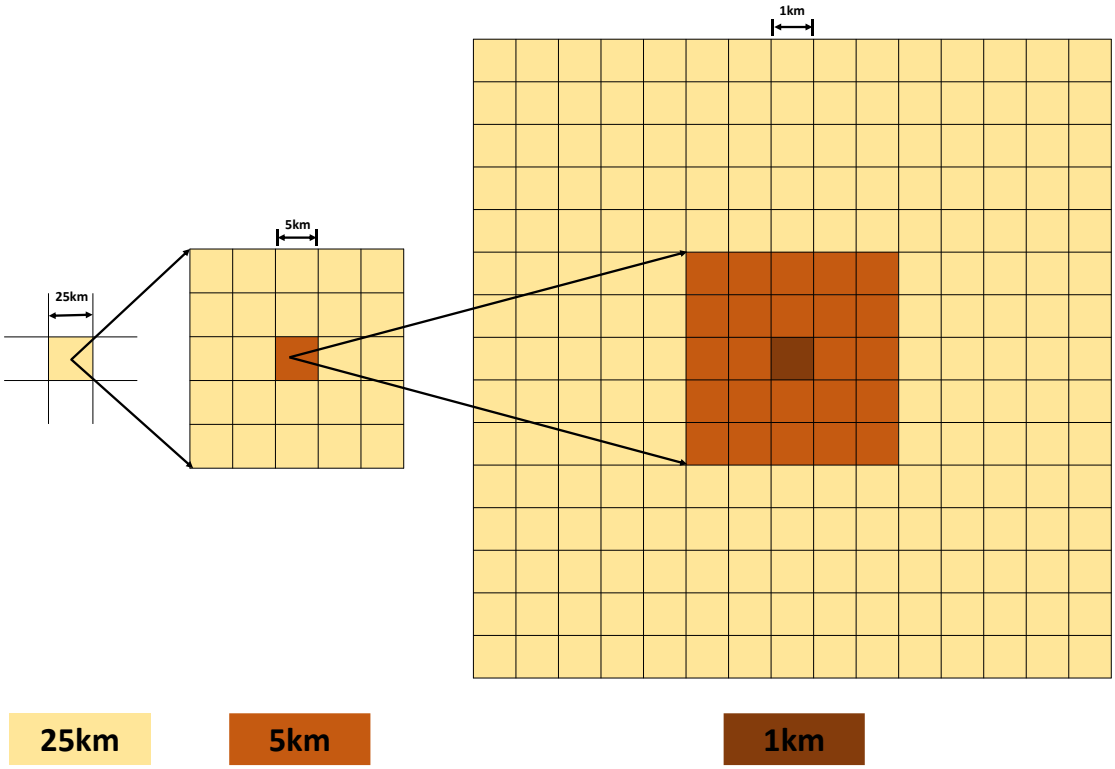

Figure S3. Conceptual subdivision of a coarse grid cell from the 25-km grid into smaller grid points for the finer grids. Each 25-km grid cell is subdivided into 25 5-km grid cells. Each of the 5-km grid cells are further refined into 25 1-km grid cells for a total of 625 1-km grid cells per 25-km cell. The solid black triangle indicates the location of the USTC site.

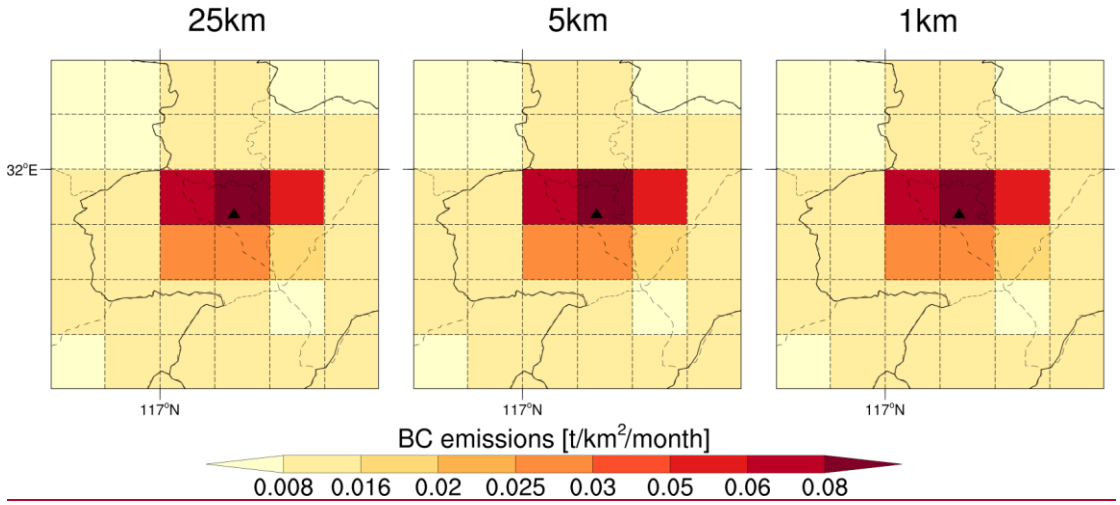

Figure S4. Spatial distribution of BC emissions in the study area for 25-km (left), 5-km (middle), and 1-km (right) resolution simulations, respectively. The solid black triangle indicates the location of the USTC site.

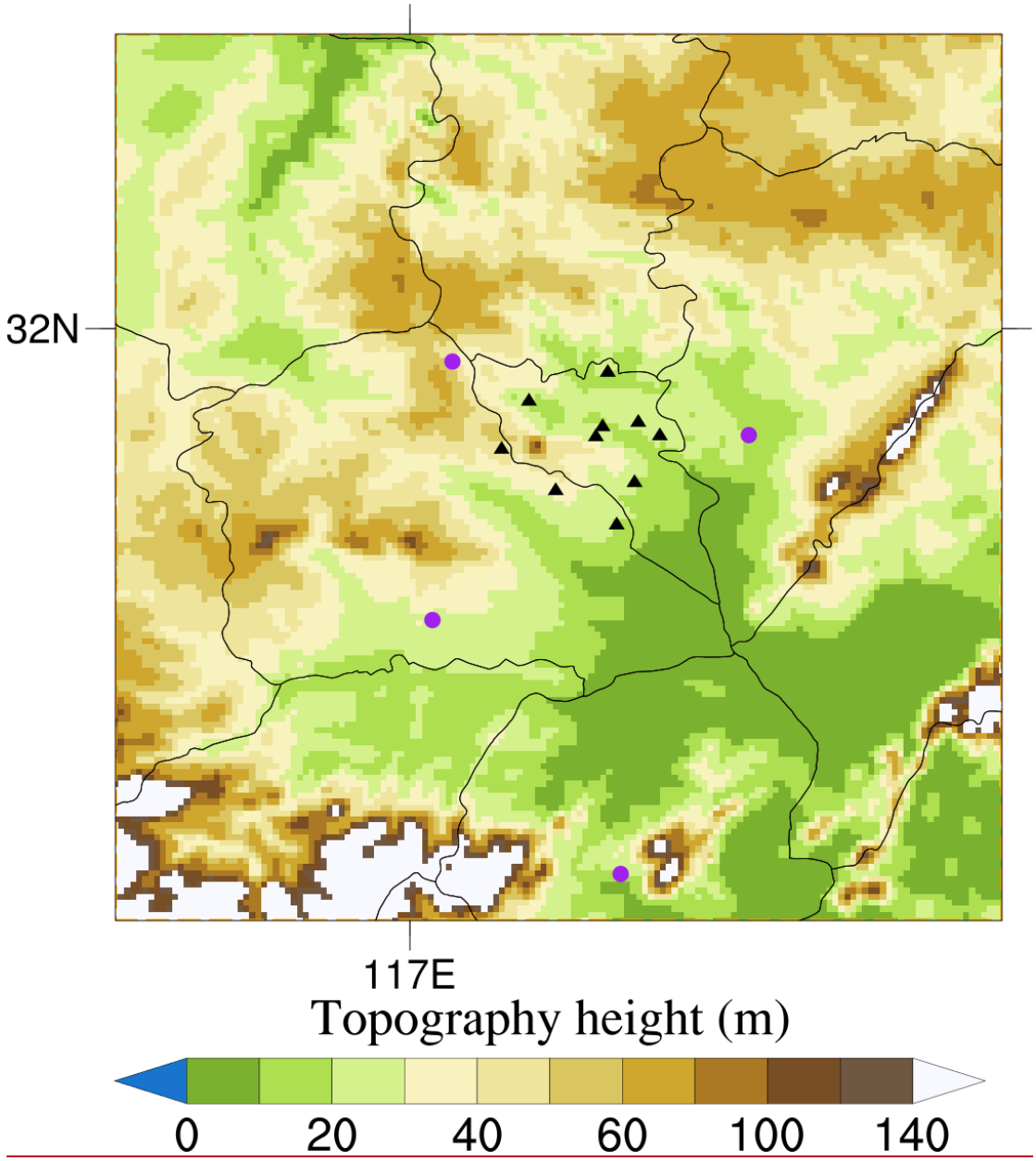

Figure S5. Spatial distributions of 4 MEP and 10 AWS sites used in this study. Solid black triangles indicate MEP monitoring sites, and purple solid dots indicate AWSs locations.

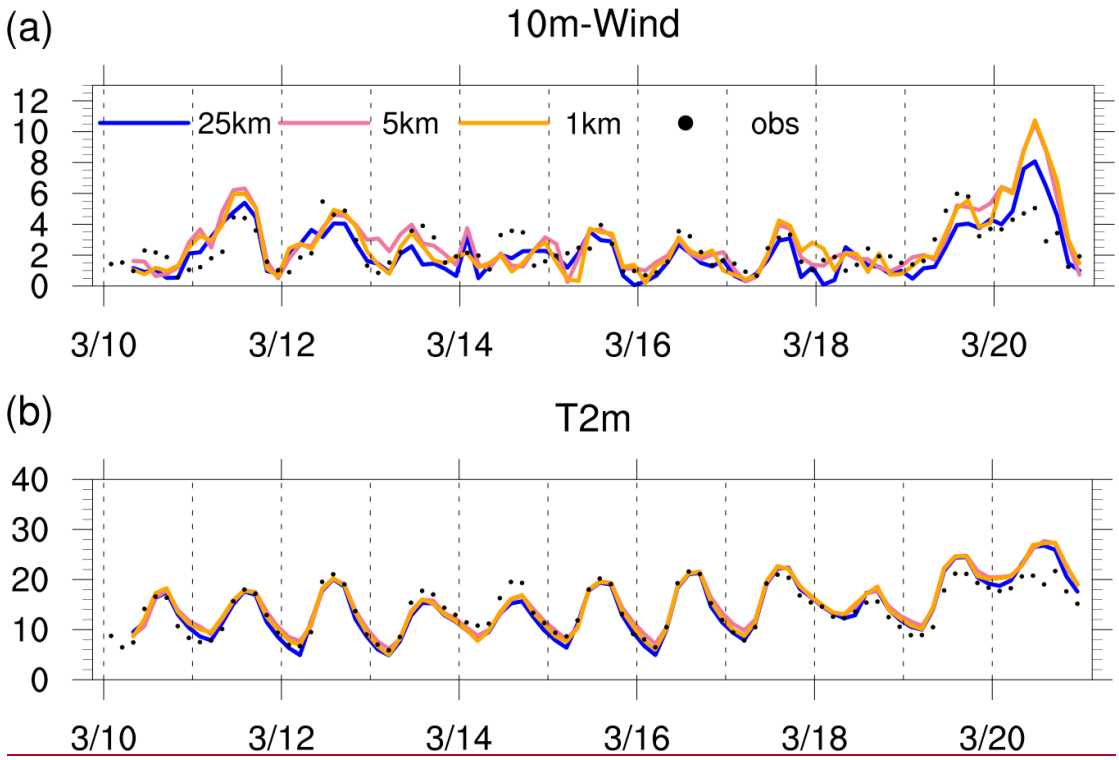

Figure S6. Time series averaged over 4 AWS sites in Hefei of observed (black dot) and simulated wind speed at 8 m (top, unit: m s-1) and temperature at 2 m (middle, unit: ℃) for 25-km (solid blue line) resolution, 5-km (solid pink line) resolution, and 1-km (solid orange line), respectively.

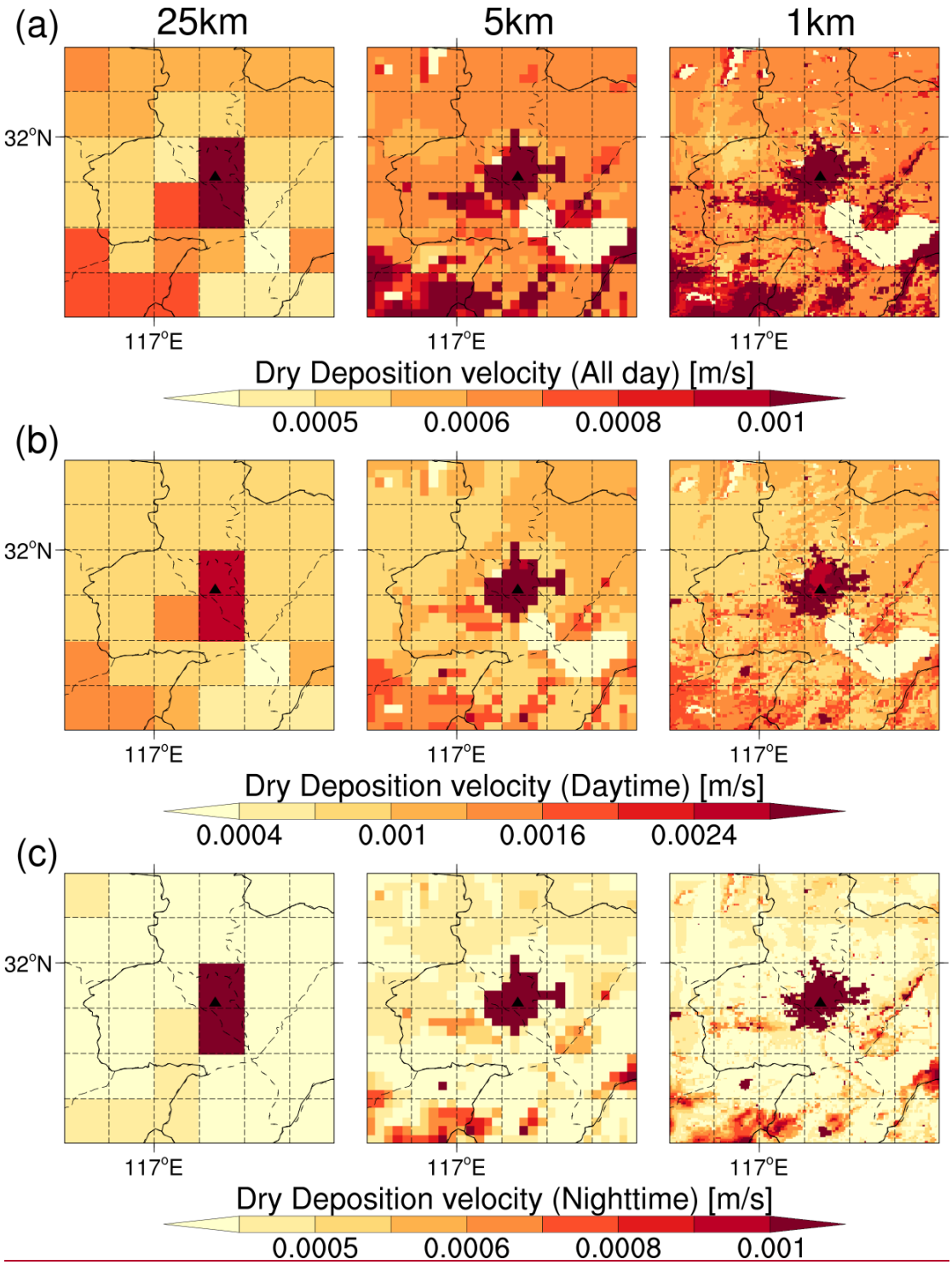

Figure S7. Spatial distribution of the dry deposition velocity in the study area for 25-km (left), 5-km (middle), and 1-km (right) resolution simulations of the whole day (top), the daytime (middle), and the nighttime (bottom), respectively. The solid black triangle indicates the location of the USTC site.

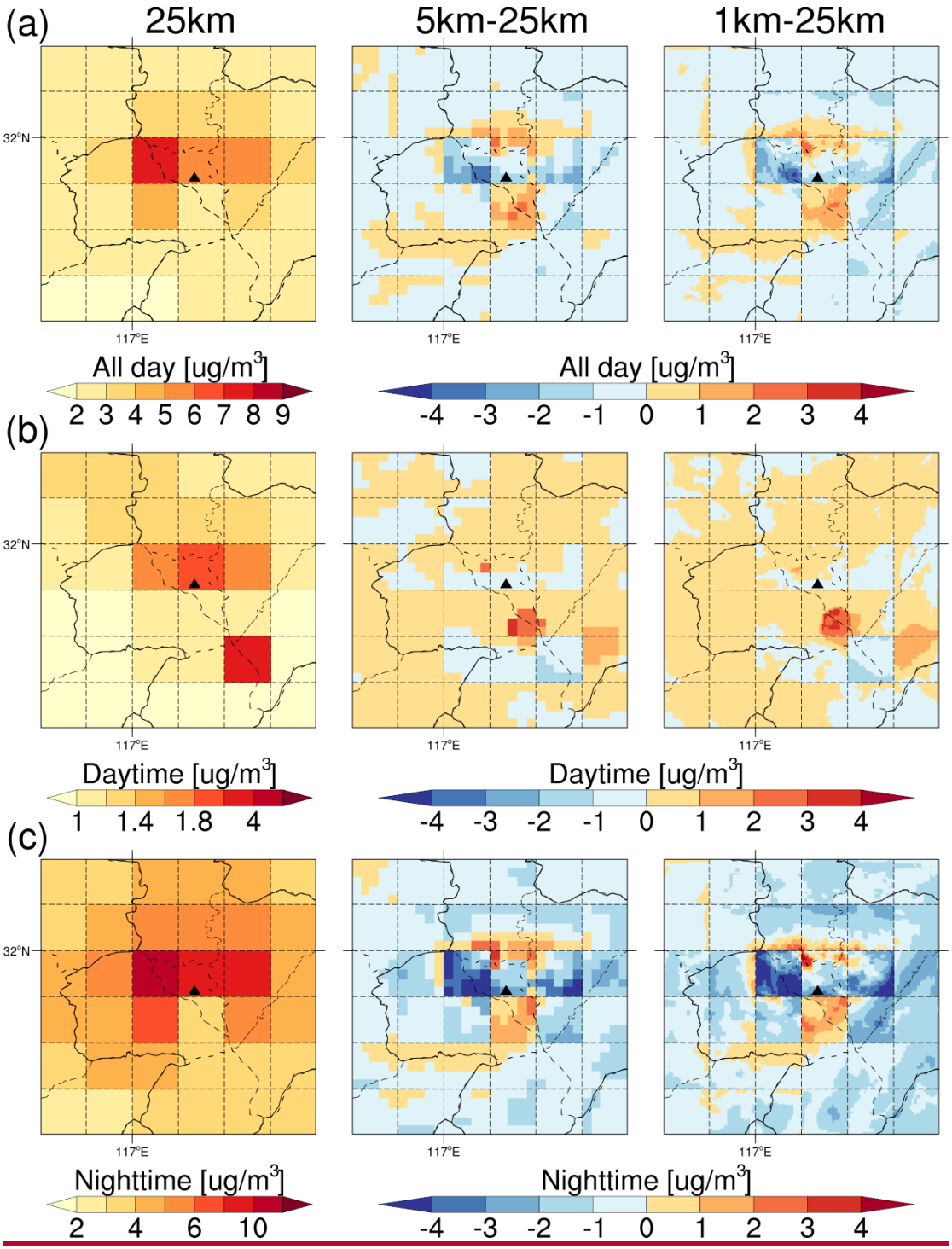

Figure S8. Spatial distribution of the BC surface concentration in the study area for 25-km resolution (left), the difference between 25-km and 5-km resolutions (middle), and the difference between 25-km and 1-km (right) resolutions of the whole day (top), the daytime (middle), and the nighttime (bottom), respectively. The solid black triangle indicates the location of the USTC site.

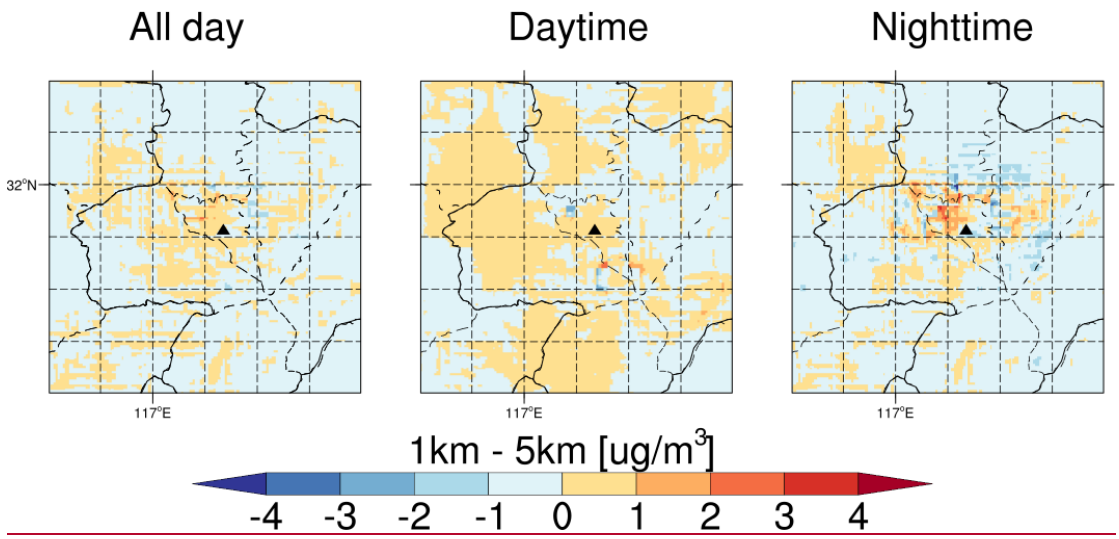

Figure S9. Spatial distribution of the differences in BC surface concentrations between 1-km and 5-km resolutions in the study area of the whole day (left), the daytime (middle), and the nighttime (right), respectively. The solid black triangle indicates the location of the USTC site.

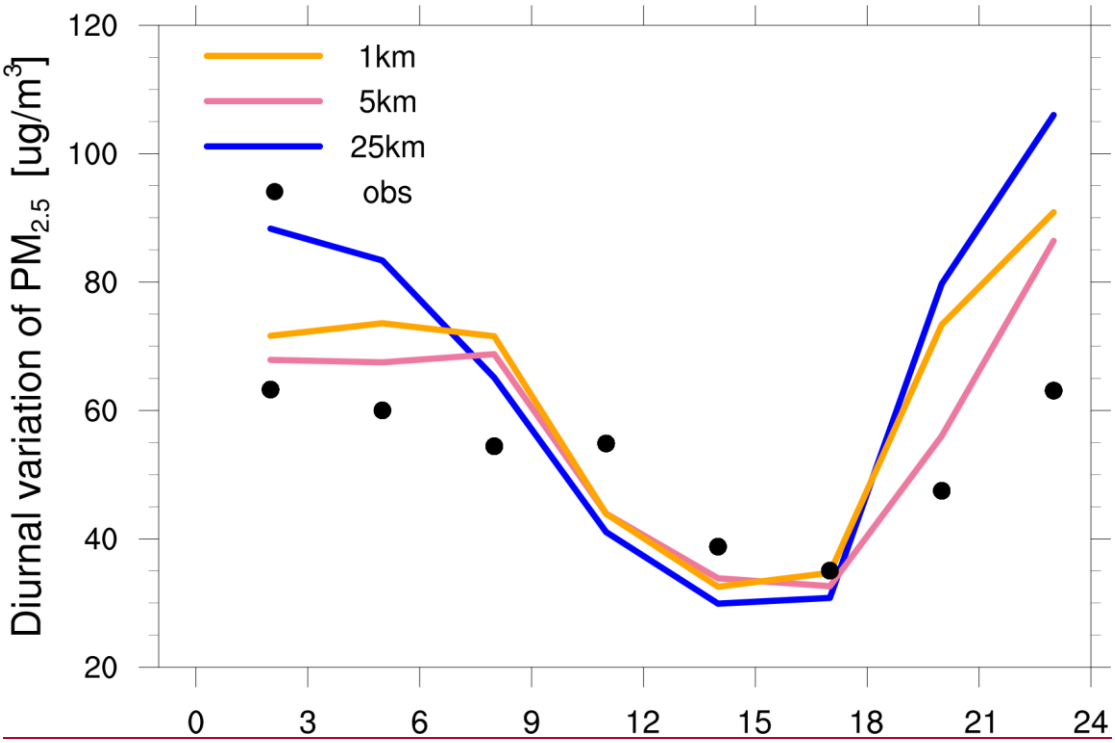

Figure S10. Diurnal variation of $PM_{2.5}$ surface concentrations within 24 h averaged over 10 MEP sites in Hefei during the study period for 25-km (solid blue line), 5-km (solid pink line), and 1-km (solid orange line) resolution simulations and observations (black dot). Both the simulated results and observations are sampled at the model output frequency, i.e., 3-hourly.

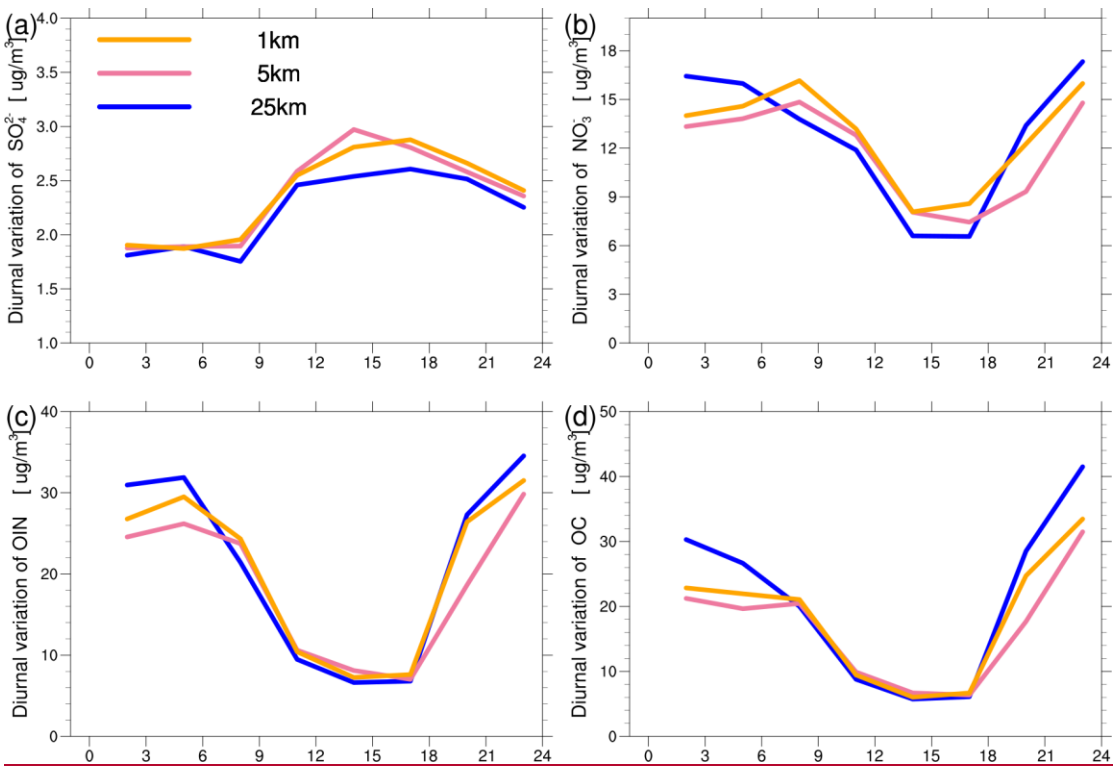

Figure S11. Diurnal variation of (a) $\mathbf{SO_4^{2-}}$, (b) $\mathbf{NO_3^-}$, (c) OIN, and (d) OC surface concentrations within 24 h averaged over 10 MEP sites in Hefei during the study period for 25-km (solid blue line), 5-km (solid pink line), and 1-km (solid orange line) resolution simulations. The simulated results are sampled at the model output frequency, i.e., 3-hourly.

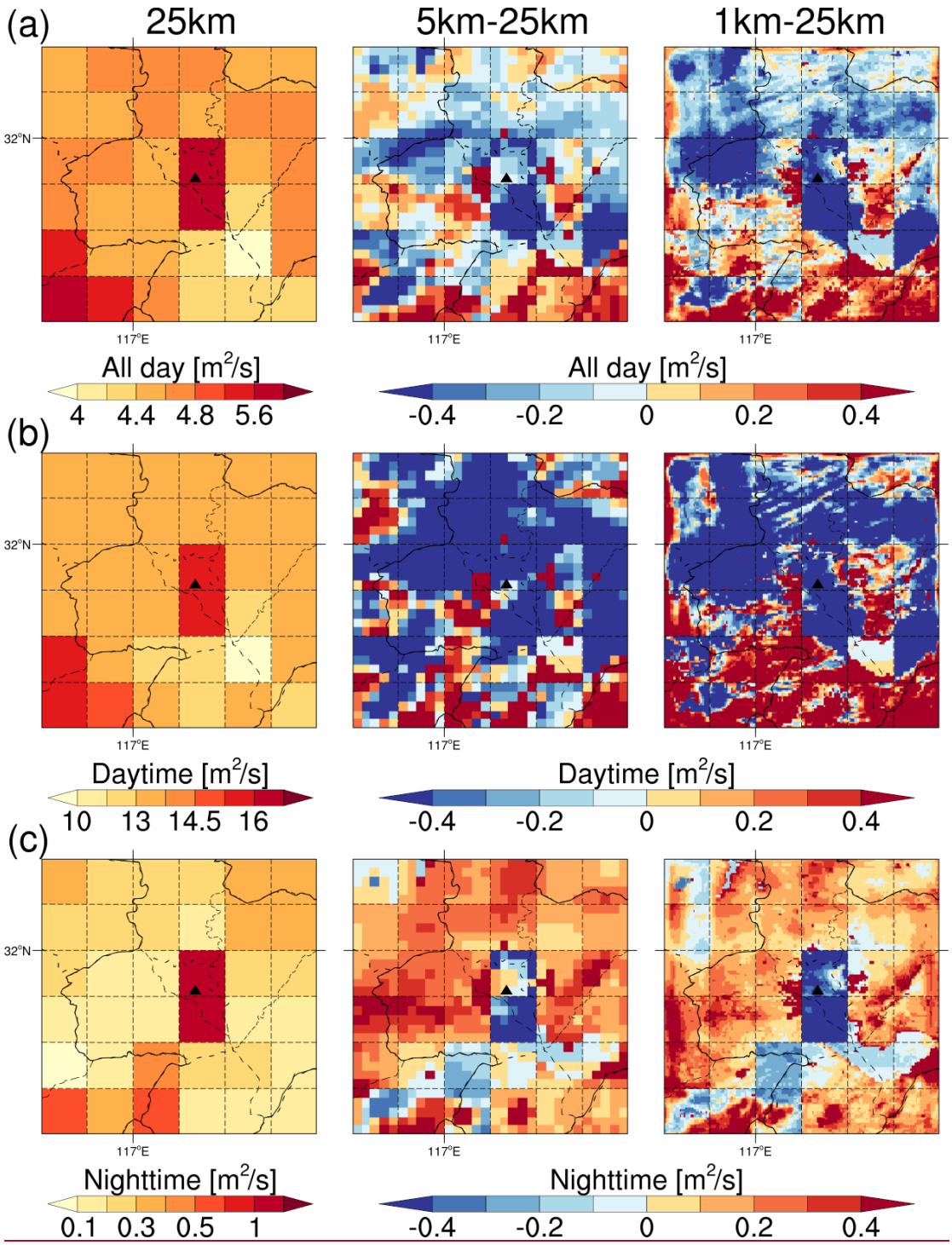

Figure S12. Spatial distribution of PBL mixing coefficients in the study area for 25-km resolution (left), the difference between 25-km and 5-km resolutions (middle), and the difference between 25-km and 1-km (right) resolutions of the whole day (top), the daytime (middle), and the nighttime (bottom), respectively. The solid black triangle indicates the location of the USTC site.

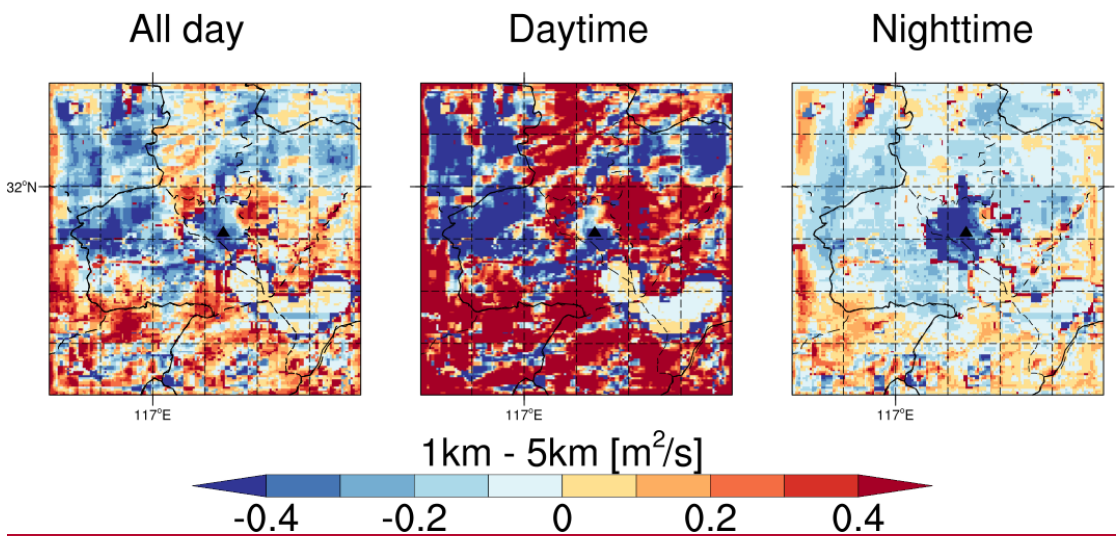

Figure S13. Spatial distribution of the differences in PBL mixing coefficients between 1-km and 5-km resolutions in the study area of the whole day (left), the daytime (middle), and the nighttime (right), respectively. The solid black triangle indicates the location of the USTC site.

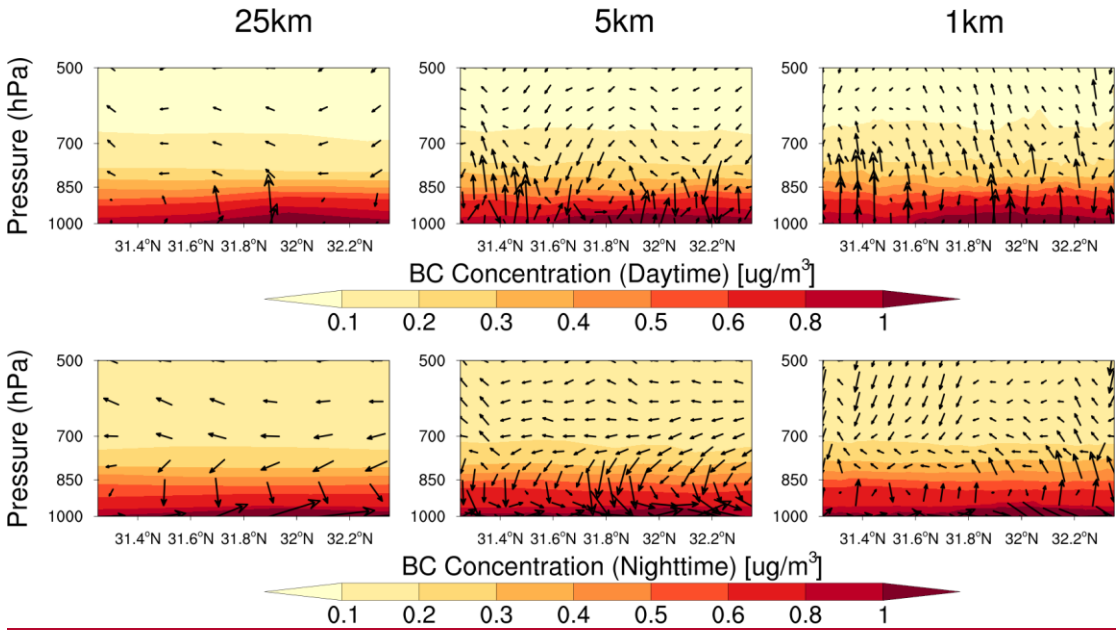

Figure S14. The latitude-pressure cross section of BC concentrations and wind speed flux along the USTC site for 25-km (left), 5-km (middle), and 1-km (right) resolution simulations of the daytime (top), and the nighttime (bottom), respectively. Vector arrows are the combination of wind speed fluxes v and w, with the vertical wind speed flux being multiplied by 100 for visibility. The shaded contours represent BC concentrations at each pressure level.

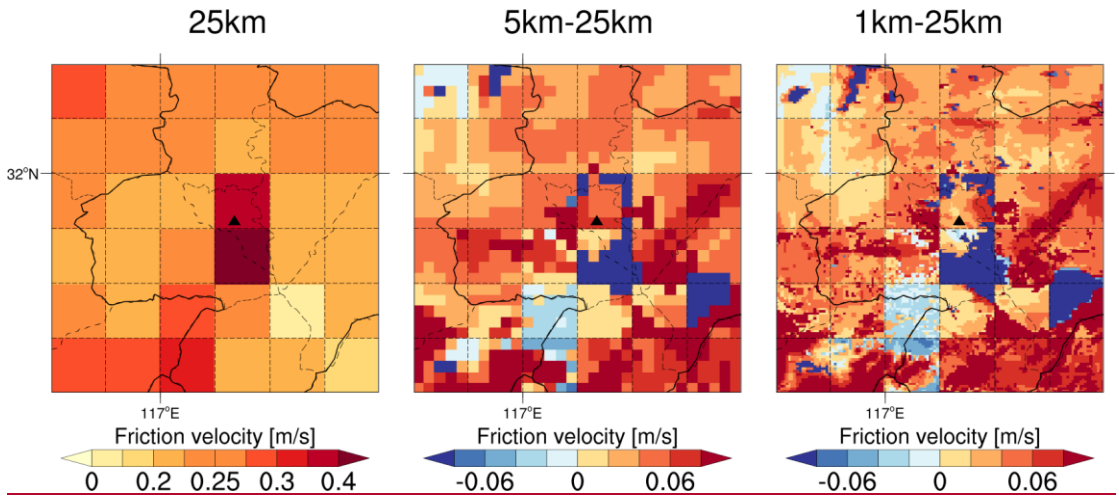

Figure S15. Spatial distribution of the friction velocity in the study area for 25-km resolution (left), the difference between 25-km and 5-km resolutions (middle), and the difference between 25-km and 1-km resolutions (right) simulations of the whole day, respectively. The solid black triangle indicates the location of the USTC site.

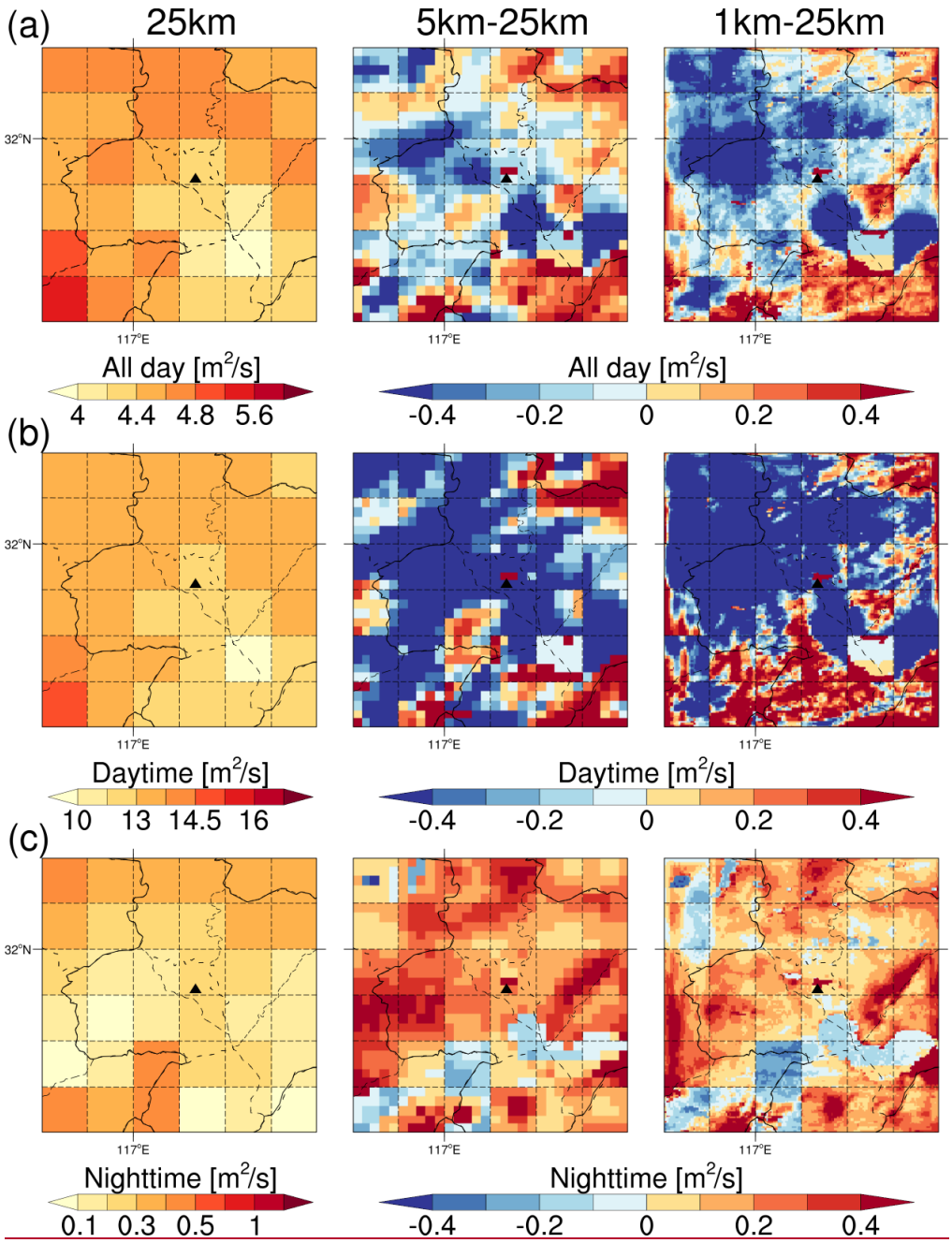

Figure S16. Spatial distribution of PBL mixing coefficients in the study area for 25-km resolution (left), the difference between 25-km and 5-km resolutions (middle), and the difference between 25-km and 1-km (right) resolutions of the whole day (top), the daytime (middle), and the nighttime (bottom), respectively. The solid black triangle indicates the location of the USTC site. The simulation results are from the sensitivity experiments.

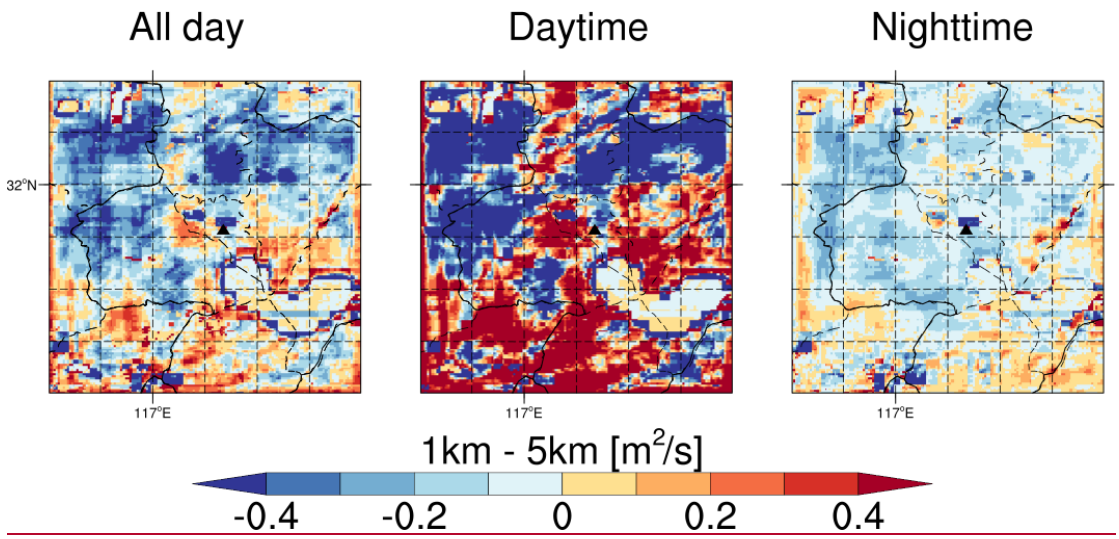

Figure S17. Spatial distribution of the differences in PBL mixing coefficients between 1-km and 5-km resolutions in the study area of the whole day (left), the daytime (middle), and the nighttime (right), respectively. The solid black triangle indicates the location of the USTC site. The simulation results are from the sensitivity experiments.

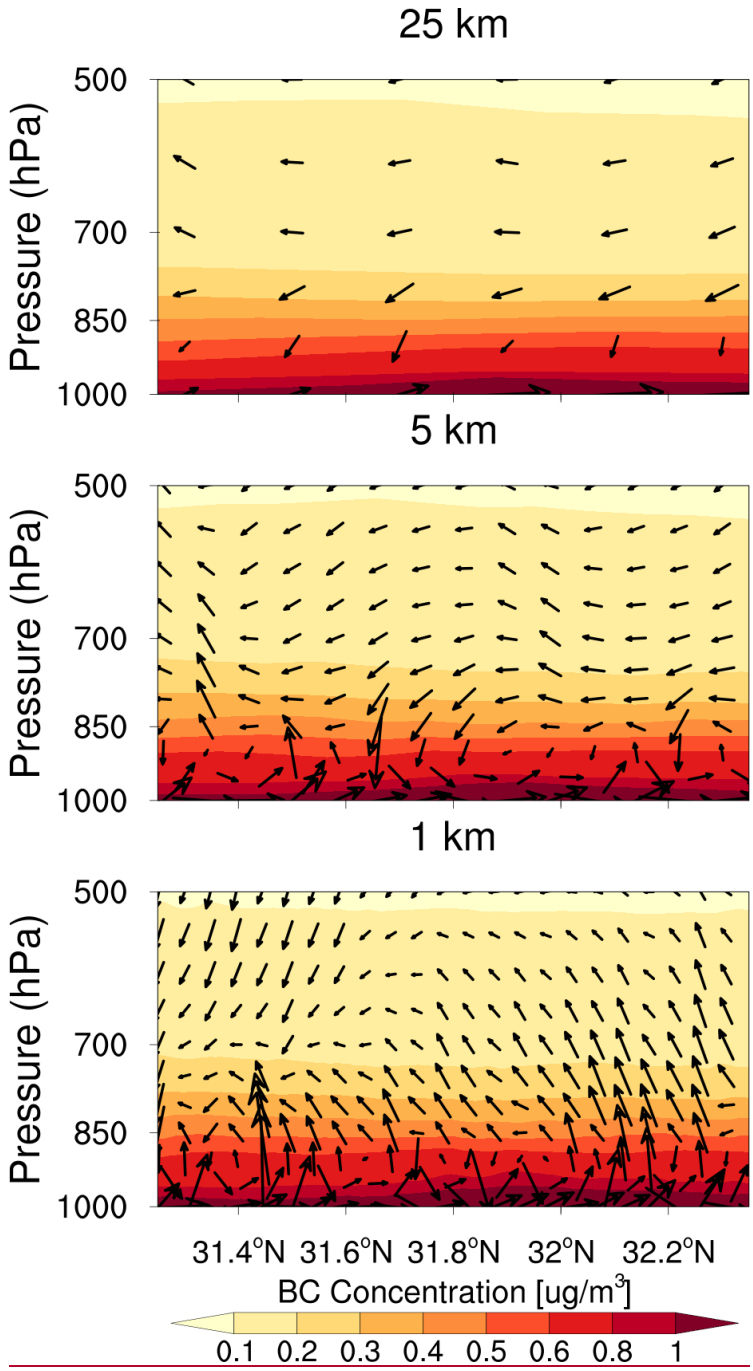

Figure S18. The latitude-pressure cross section of BC concentrations and wind speed flux along the USTC site for 25-km (top), 5-km (middle), and 1-km (bottom) resolution simulations of the whole day, respectively. Vector arrows are the combination of wind speed fluxes v and w, with the vertical wind speed flux being multiplied by 100 for visibility. The shaded contours represent BC concentrations at each pressure level. The simulation results are from the sensitivity experiments.

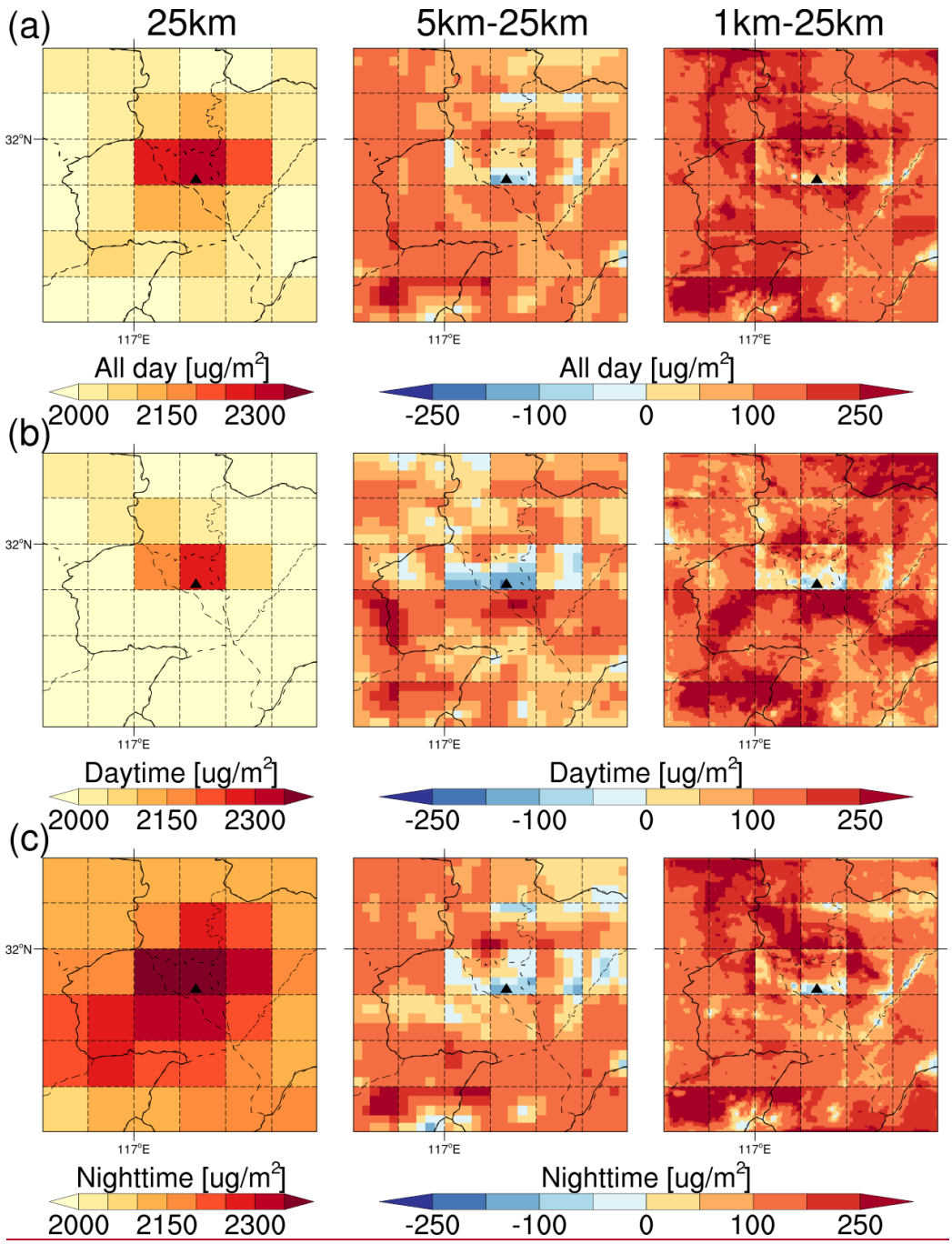

Figure S19. Spatial distribution of the BC column concentration in the study area for 25-km resolution (left), the difference between 25-km and 5-km resolutions (middle), and the difference between 25-km and 1-km (right) resolutions of the whole day (top), the daytime (middle), and the nighttime (bottom), respectively. The solid black triangle indicates the location of the USTC site.

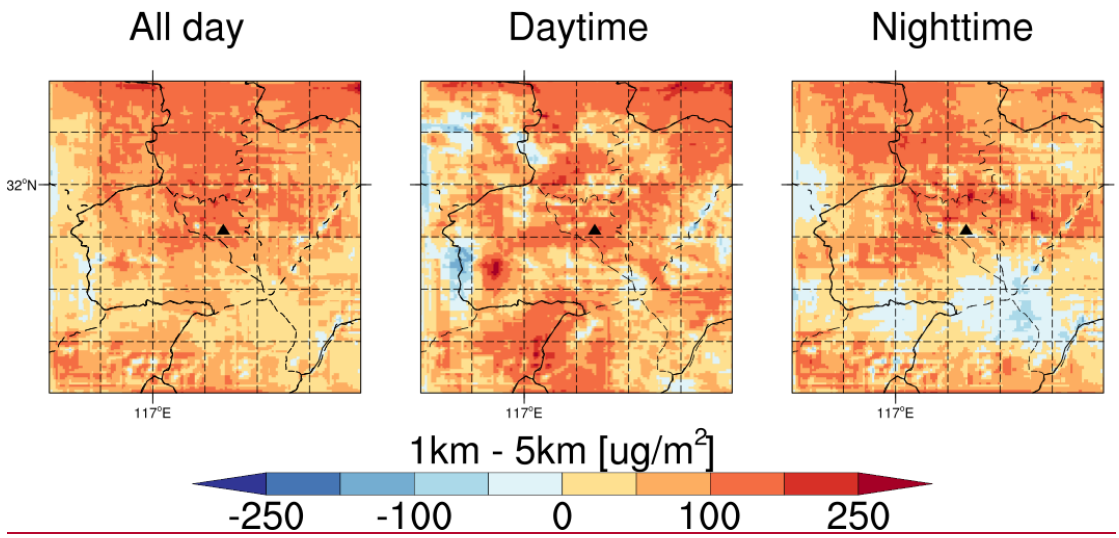

Figure S20. Spatial distribution of the differences in BC column concentrations between 1-km and 5-km resolutions in the study area of the whole day (left), the daytime (middle), and the nighttime (right), respectively. The solid black triangle indicates the location of the USTC site.